International
Progress Report

IPR-05-40

Äspö Hard Rock Laboratory

TRUE-1 Continuation Project

Fault rock zones characterisation

Characterisation and quantification of resin-impregnated fault rock pore space using image analysis

Eva Hakami
Weixing Wang

Itasca Geomekanik AB

August 2005

Svensk Kärnbränslehantering AB
Swedish Nuclear Fuel
and Waste Management Co
Box 5864
SE-102 40 Stockholm Sweden
Tel 08-459 84 00
+46 8 459 84 00
Fax 08-661 57 19
+46 8 661 57 19

Äspö Hard Rock
Laboratory

Report no.
IPR-05-40
No.
F83K
Author
Eva Hakami
Weixing Wang
Date
August 2005
Checked by
Anders Winberg
Date
September 2009
Approved
Mats Ohlsson
Date
November 2009

Äspö Hard Rock Laboratory

TRUE-1 Continuation Project

Fault rock zones characterisation

Characterisation and quantification of resin-impregnated fault rock pore space using image analysis

Eva Hakami
Weixing Wang

Itasca Geomekanik AB

August 2005

Keywords: Binary, Epoxy, Fracture, Image analysis, Network, Resolution, UV

Summary

Enhanced knowledge of the geometrical structure of the void pore space of fault zones is a need for improved conceptualisation and development of flow and transport analyses. The objective of this study, which is a part of the TRUE-1 Continuation Project, has been to develop techniques and gain experience for direct measurements of fault zone pore space geometry.

The approach adopted was to first impregnate the fault rock zone *in situ* with fluorescent epoxy after which the injection (pilot) borehole was overcored with a 300 mm drill bit. The epoxy-reinforced zone could in this way be sampled and further cut into smaller slices in two different directions across the zone. The slices were then photographed at different scales.

A methodology for image analysis of the fracture pore space was developed. It includes image acquisition with UV-lighting, image processing and image analysis, steps which are described in this report. A number of quantitative parameters to describe the complex pattern of the fracture network of a zone have been defined. A similar approach in analysing single fractures is also described with two examples.

The measurement methods were successfully applied on rock samples taken from short boreholes in the tunnel wall in the Äspö hard rock laboratory, where a minor deformation zone (fault) was exposed. The results from this study shows that the pore space of the fault zone makes up a complex pattern. Shear movements and infilling material determine the structure of the pore space.

For this fault zone sample of 20 cm length the general character of the zone remained unchanged along its length. The thickness of the zone is about 6 cm. The total aperture (i.e. the summed up apertures from all fracture branches of the network) is about 14 mm and the average number of fractures of the network is 5-6. The aperture is unevenly distributed between the fractures of the network with one or two fractures with clearly larger apertures. The number of junctions between fracture network branches (within a 1 cm long section) is typically 7 or 19 depending on the orientation of the sample slice. This anisotropy of the network pattern is a result of the shear movements that have created the fault rock pore space. The parameter “porosity” is difficult to define and is therefore not recommended as a descriptive parameter for fault rock.

Sammanfattning

För att få en bättre konceptuell förståelse, och utveckla flödes- och transportanalyser för deformationszoner (förkastningssprickor) i kristallint berg, krävs en ökad kunskap om de geometriska egenskaperna hos porvolymen i mindre deformationszoner. Målet med denna studie, som är en del av projektet ”TRUE-1 Continuation”, har varit att utveckla tekniker och samla erfarenheter från direkta mätningar av geometrin hos porvolymen i deformationszoner.

Det angreppssätt som tillämpats är att först impregnera zonen *in situ* med fluoriserande epoxy och därefter överborra injiceringshålet (pilotborrhålet) med en 300 mm borrkrona. Den epoxyförstärkta zonen kunde på detta sätt provtas och kärnan ytterligare kapas till skivor i två olika riktningar tvärs zonen. Skivorna fotograferades i olika skalor.

En metodologi för bildanalys av sprickornas porvolym har utvecklats. Den innebär fotografering med UV-ljus, bildbehandling och bildanalys, steg vilka beskrivs i rapporten. Ett antal kvantitativa parametrar har definierats för att beskriva det komplexa mönstret hos zoners spricknätverk. Ett liknande angreppssätt för analyser av enskilda sprickplan beskrivs också med två exempel.

Mätmetoderna tillämpades framgångsrikt på bergprover tagna från korta borrhål i tunnelväggen i Äspölaboratoriet där en mindre deformationszon (förkastningsspricka/sprickzon) korsar tunneln. Resultaten från studien visar att porvolymen i denna zon har ett komplicerat mönster. Skjuvrörelser och sprickfyllnadsmaterial bestämmer strukturen hos porvolymen.

För detta 20 cm långa prov från zonen är det generella utseendet oförändrat över provets längd. Zonens bredd är ca 6 cm. Den totala aperturen, dvs den summerade aperturen från alla sprickor i nätverket tvärs zonen, är ca 14 mm, och medelantalet sprickor är 5-6 stycken. Aperturen hos dessa är ojämnt fördelad med en eller ett par sprickor med klart större apertur. Antalet korsningspunkter mellan sprickor i nätverket, i ett 1 cm långt avsnitt av sektionen, är typiskt ca 7 respektive 19 stycken beroende på i vilken riktning de studerade skivorna är kapade. Denna anisotropi i nätverksmönstret är ett resultat av skjuvrörelserna som har skapat sprickzonens porvolym. Parametern ”porositet” är svår att definiera på ett precist sätt för en deformationszon, och rekommenderas därför inte som en lämplig parameter för karaktärisering.

Contents

1 Introduction

One of the factors that determine the safety around an underground radioactive waste repository is the isolating properties of the surrounding rock mass. Therefore the rock mass retention properties have been a major topic for research at the Äspö Hard Rock Laboratory, specifically in the Tracer Retention Understanding Experiment (TRUE) research program, including several phases and sub projects e.g. /Winberg et al. 2000/ and /Winberg et al. 2003/.

This report concerns a part of a project within the TRUE-1 Continuation Project which focuses on the characteristics and properties of fault rock zones. The aim of this subproject is to gain better understanding of the geometrical and mineralogical characteristics of fault rock. The approach taken to assess the geometry pore structure of fault rock for the current study is to inject fluorescent epoxy resin into the fractures of selected fault rock zones /Stigsson et al. 2003/ and /Maersk-Hansen and Staub 2004/. The injected epoxy gives rise to an increase in local rock strength of the fault rock zone and enables collection of intact large diameter drill core samples /Maersk-Hansen and Staub 2004/. Addition of fluorescent dye makes the epoxy-filled pore space more easily detectable and measurable. The methodology applied builds largely on methodology and experiences gained from the Pilot Resin Injection experiment, performed as part of the TRUE-1 Project /Winberg et al. 2000/.

The work process adopted in the current work and its coupling to the disposition of the current report is given in Figure 1-1.

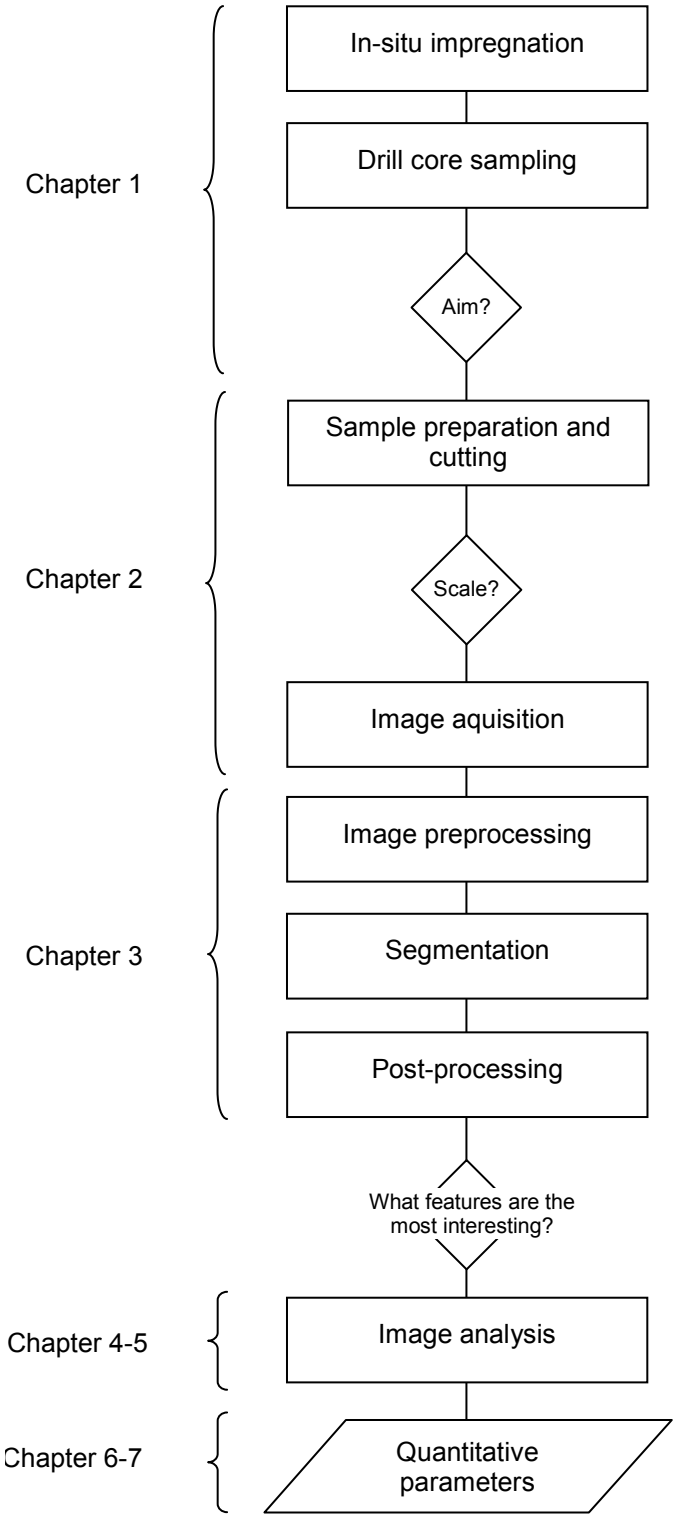

Figure 1-1. *The flowchart shows the different steps taken in the image analysis, starting from in-situ impregnation leading finally to the characterization parameters. The chapters where each step is reported are indicated.*

2 Sample collection and image acquisition

2.1 Core sample description

In the summer of 2004 two boxes of rock samples from the epoxy injected faults were received. The description of the field work, including geological mapping, may be found in /Maersk-Hansen and Staub 2004/. The first box included samples from borehole KA2423A03 (pieces B1-B4) and borehole KA2169A01 (pieces B1-B4). The samples consist of one upper half pipe of the core cut along the axis of the core, see Figure 2-1. (The lower half of the core was not available for this study.) The second box included samples from borehole KA2169A03 (B1-B2, two pieces of rock specimens). These samples were broken and could not be used further, i.e. there was either no epoxy in fractures or the existing epoxy had not been able to penetrate and glue the rock fractures sufficiently together.

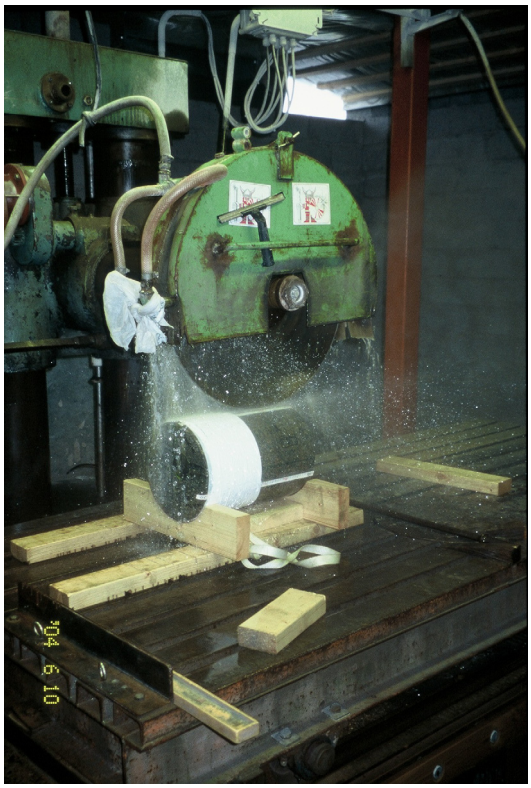

Figure 2-1. *An illustration of how the cutting of the large diameter (300 mm) drill core was made.*

The eight rock specimens from borehole KA2169A01 and KA2423A03 were explored further. The collected information is given in Table 2-1 and Table 2-2. From borehole KA2169A01 there are four sample pieces (B1-B4). Sample B1 includes one fracture, B2 has two fractures, and B3-B4 have three fractures, respectively. Some samples were broken along existing fractures. Borehole KA2423A03 includes four sample pieces (B1-B4): B1 has one open fracture, B2 and B3 includes a complex fracture network at the fault intersection, and B4 has no fractures.

Table 2-1. Description of samples collected in borehole KA2169A01.

Sample No.	Fractures	Epoxy occurrence	Comments
B1	1	Yes. Epoxy on the whole broken surface from centre and out.	Corner is broken and the ruler at corner. Includes a part of the injection pipe.
B2	3	Yes. Epoxy on the broken fracture surface and also in glued single fracture.	Sample broken along the fracture.
B3	c. 3 – 4	No	
B4	c. 3	Very short impregnation distance in one or two fractures. Between dummy and borehole wall.	Rubber dummy in the pilot borehole.

Table 2-2. Description of samples collected in borehole KA2423A03.

Sample No.	Fractures	Epoxy occurrence	Comments
B1	Yes, one open	No, only at borehole wall	
B2	Yes, complex	Yes	Corner is broken, Two measurement tapes
B3	Yes	Yes, both in single fracture and fractured zone	Neighbour sample to B2. Broken in the contact between intact rock and fractured zone.
B4	None	No	One cut perpendicular and the other with angle c. 45 degrees.

2.1.1 Selection of samples for further study

The aim of this project is to gain better understanding of fault rock. Therefore the samples B2 and B3 from KA2423A03 were selected for further studies, since these samples encompassed the core of the fault zone. These samples also showed highly successful impregnation. The core samples from KA2169A01 were thus not used in the further studies since this core does not include the central part of the fault zone. Some of the fractures had a limited epoxy penetration and most of the fractures were broken during sampling.

Figure 2-2 and Figure 2-3 shows how the large diameter core from KA2423A03 has been successively cut into smaller pieces. The way in which the samples from this drill core were cut is also illustrated in Figure 2-4.

Figure 2-2. *The core was cut along the core axis into two halves. Only one half (upper half) was used in the current study. This image shows samples B1, B2, B3 and B4 from borehole KA2423A03. The left side of the core is positioned closest to the tunnel and the intersection with the fracture zone centre is at 2.4 m borehole depth /Maersk-Hansen and Staub 2004/. (N.B. the reference tapes that can be observed in some photographs do not refer to borehole depth and were used only for relative measurements.)*

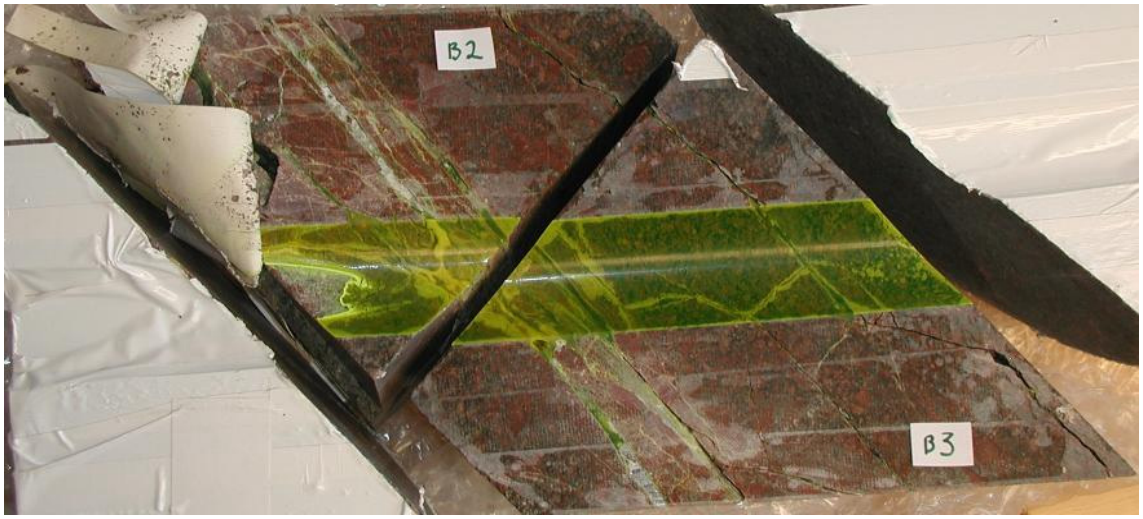

Figure 2-3. *This figure is similar to Figure 2-2, but the samples (B2 and B3 from borehole KA2423A03) are rotated such that the cut surfaces are seen. The trace of the 76 mm injection hole may be noted in the centre of the photograph (light green epoxy). (Up direction is inwards the image.)*

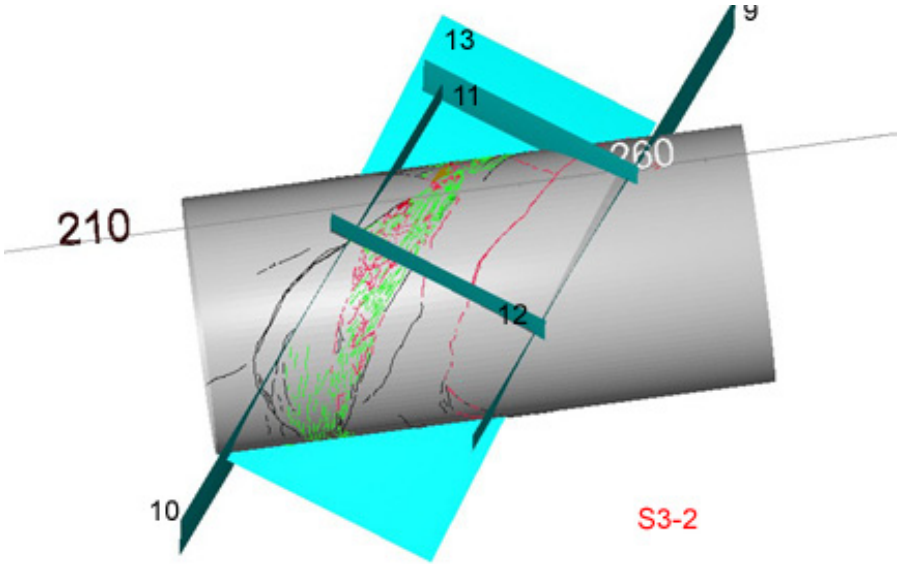

Figure 2-4. *The drill core surface of KA2423A03 was mapped and this image shows a view used for the planning of cutting. The cutting planes were chosen such that the sample would include the whole fractured zone that was the target of this study. The fault is approximately 155/83 (strike/dip) /Maersk-Hansen and Staub, 2004/.*

2.1.2 BIPS images from pilot borehole at KA2423A03

To enable a comparison between different types of characterization images the BIPS image from KA2423A03 is shown in Figure 2-5. This location corresponds to the location of the main fractured zone selected for further study. The BIPS images (borehole TV images) are routinely used at Äspö HRL as a complement to the geological mapping.

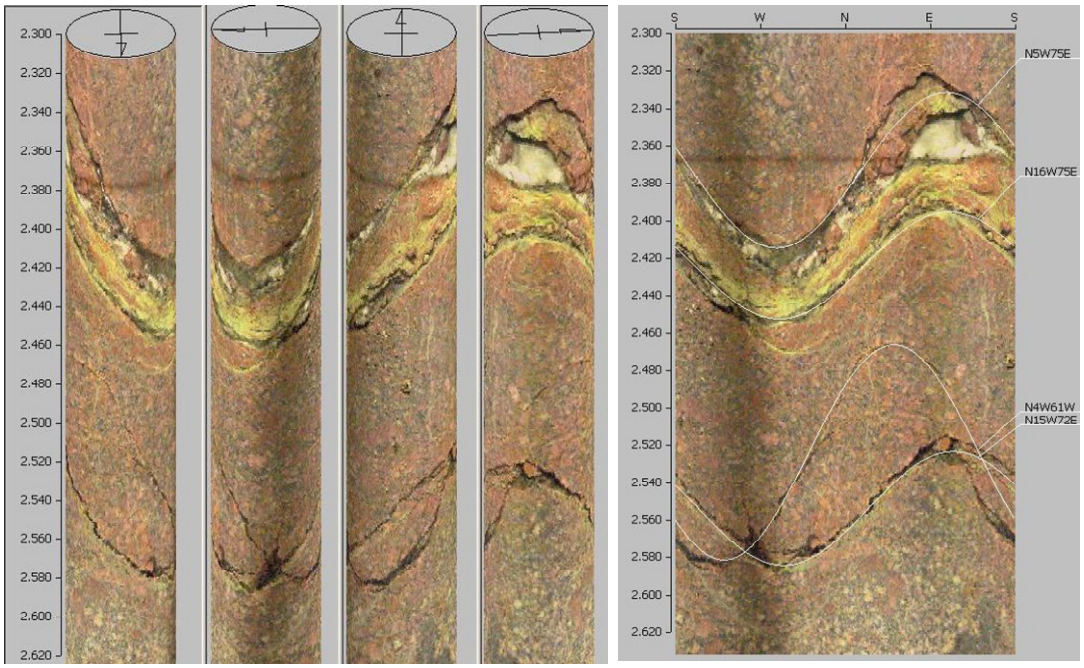

Figure 2-5. *BIPS image from pilot borehole at centre of borehole KA2423A03 (cf. Figure 2-3). The fracture zone at 2.4 m depth is the zone studied in samples B2 and B3.*

2.2 Image acquisition from KA2423A03 samples B2 and B3

2.2.1 Sample surfaces overview

For each sample, three different surfaces were photographed, 1) the outer cylinder surface, 2) the cutting plane that separated the samples B2 and B3 and 3) the core plane (cutting plane parallel to borehole axis). The overview photos are shown in Figure 2-6 and Figure 2-7. More close-up images can be seen in Figure 2-8 through Figure 2-10.

Figure 2-6. *Curved surface, cutting plane and core plane of the B2 sample from KA2423A03.*

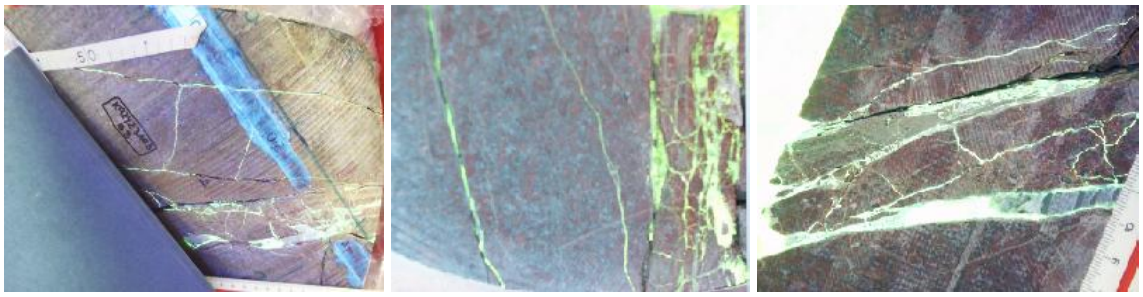

Figure 2-7. *Curved surface, cutting plane and core plane of the B3 sample (KA2423A03).*

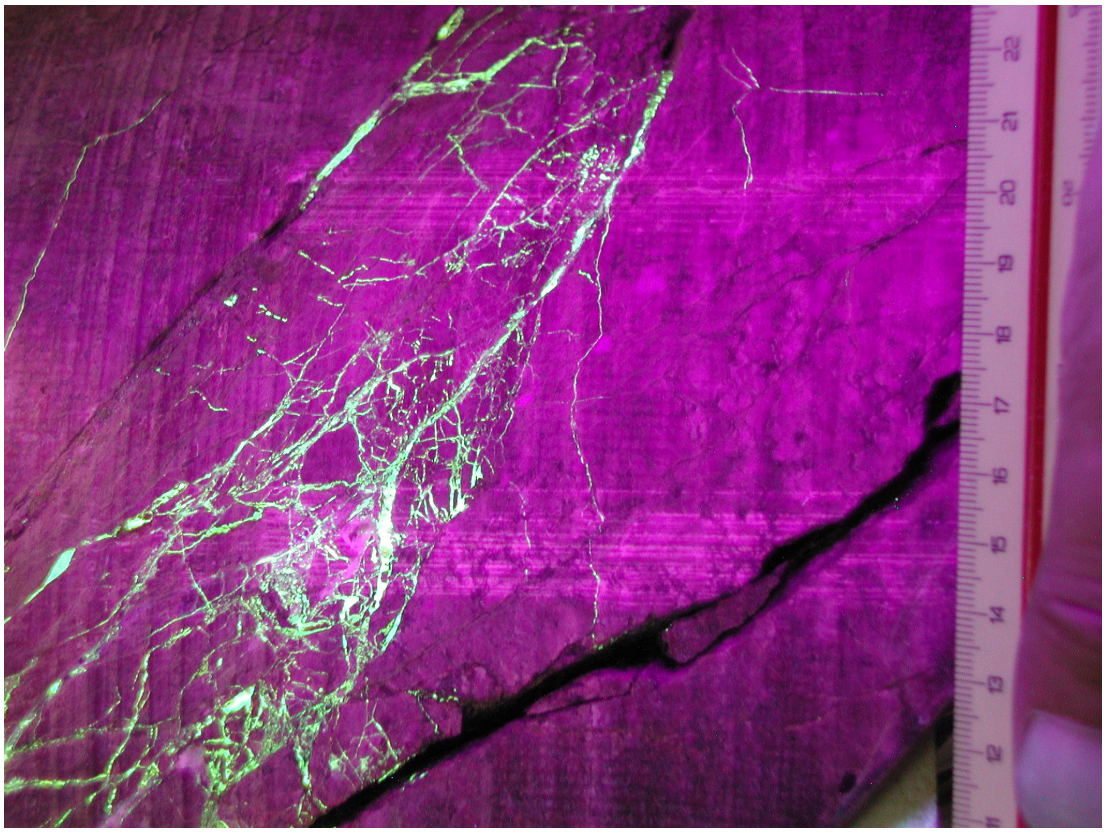

Figure 2-8. *Curved outer surface of sample B2 from KA2423A03. The image is taken at UV light, cf. Figure 2-6.*

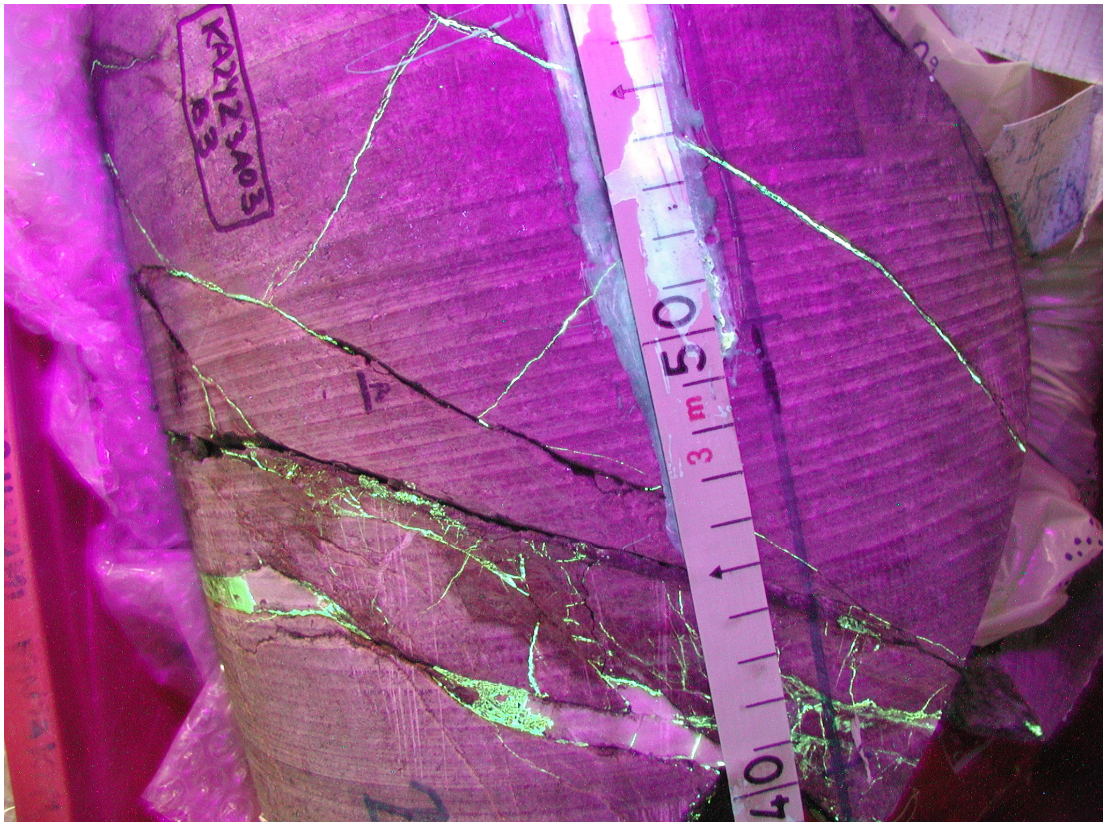

Figure 2-9. *Curved outer surface of sample B3 from KA2423A03. The image is taken at UV light, cf. Figure 2-7.*

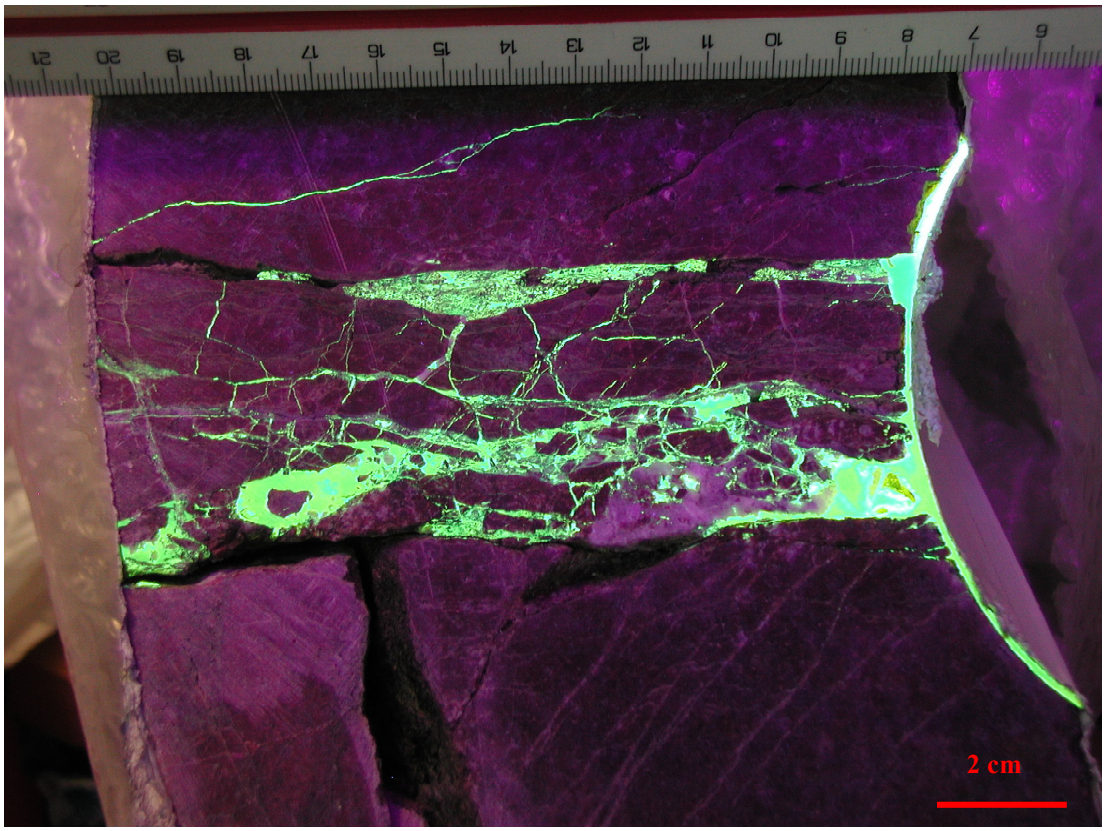

Figure 2-10. *The cutting plane separating samples B2 and B3 collected from borehole KA2423A03. The image is taken at UV light.*

2.2.2 Camera and lighting

Two different digital cameras for image collection were tested; one was an Olympus camera with resolution 2,048×1,536×24 bits, and a magnification of 4X. Example images are shown in Figure 2-8 through Figure 2-10. The other camera tested was a Minolta Dimage 7 with resolution of 2,560×1,920×24 bits, and a magnification of 7X. The ensuing comparison showed that the quality of the cameras was fairly comparable but the Minolta camera was selected for the main image acquisition. Ordinary light or UV light was used for photography in a dark room to avoid effects of extra lighting. The minimum focal distance of these cameras is about 30 cm. The cameras are very sensitive to both lighting conditions and the stability of hand of the photographer. By using an image acquisition device, shown in Figure 2-11, the camera became more stable and the focal distance could be adjusted by simply moving the camera holder up or down. The light orientation and intensity was also adjustable. Further, a method was needed to position the rock sample surfaces to be photographed levelled horizontally. This was a difficult task since the shapes of the samples were not regular. The choice of method was to simply use a box with sand and to place the rock samples on a plastic film on the sand bed with the desired horizontal orientation of the surface.

Three different illumination conditions for the image was used; one employed both ordinary lamps and UV lamps in combination (Figure 2-12), the second used only ordinary lamps (Figure 2-13 (a)), and the third employed only UV lamps (Figure 2-13 (b)). The images in Figure 2-14 and Figure 2-15 constitute two additional examples of images taken at UV light at different magnification (i.e. different focal distances, giving

different image resolution). It can be noted that even at a fairly high magnification the standard camera used gives a reasonably sharp image and small epoxy objects can readily be detected. Also, it can be concluded that the penetration of the epoxy has been good in the sample. The first type of illumination makes the epoxy areas exhibit a high light intensity, some variation in rock surface colour is also visible, and there is an element of colour distortion. The ordinary lighting conditions make the different minerals in the image come out clearly, but cannot visualise the injected fracture sharply. However, using the UV lighting only makes the epoxy-filled fractures show up more clearly, but naturally suppresses other types of information, such as different colour on different minerals, on the exposed rock surface. After this testing, it was decided to acquire each image by using two different illuminations (UV and ordinary light) separately.

Figure 2-11. *Image acquisition device: A box (red filled with fine sand; two ordinary lamps, the position of which can be adjusted; a plate with scales for samples and an ultraviolet (UV) lamp (grey with handle).*

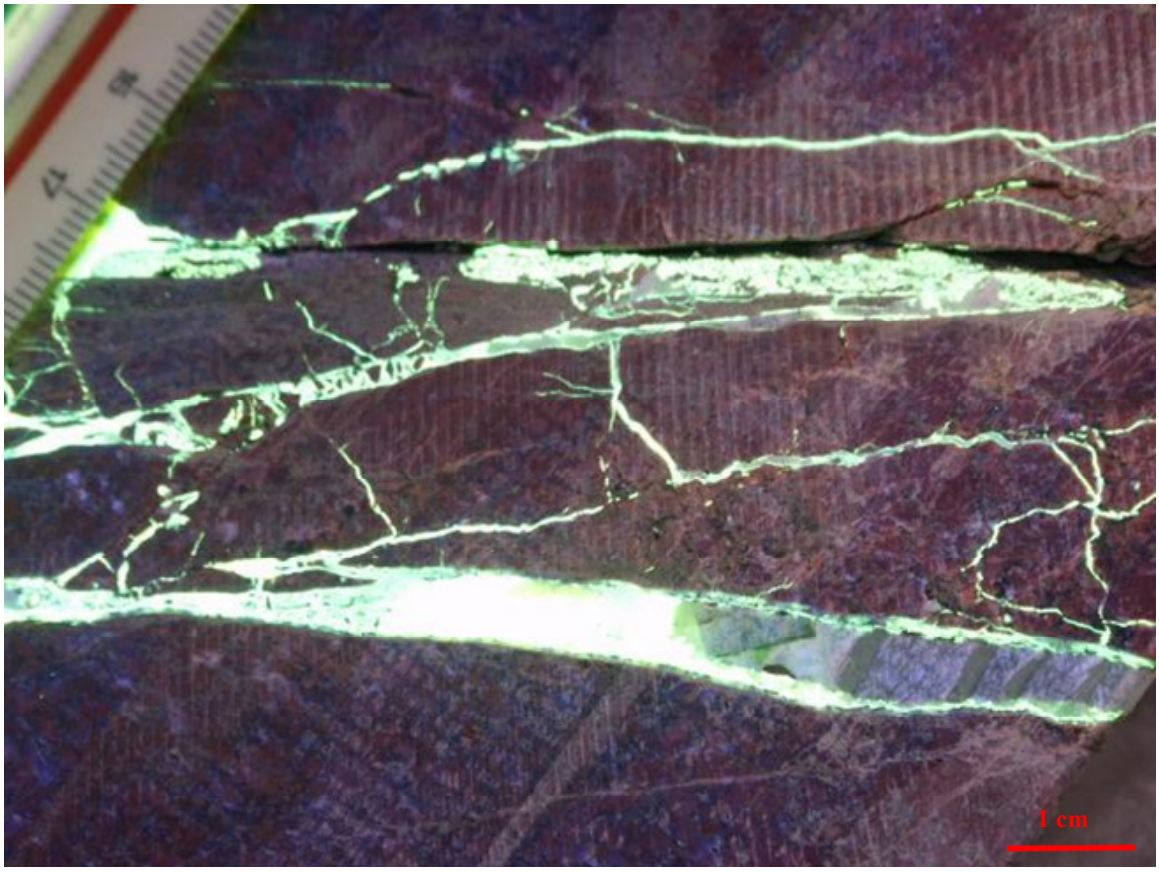

Figure 2-12. *B3 image (detail of outer surface shown in Figure 2-3, frame size is 640×480 pixels) with illumination made up of a combination of ordinary light and UV lamps.*

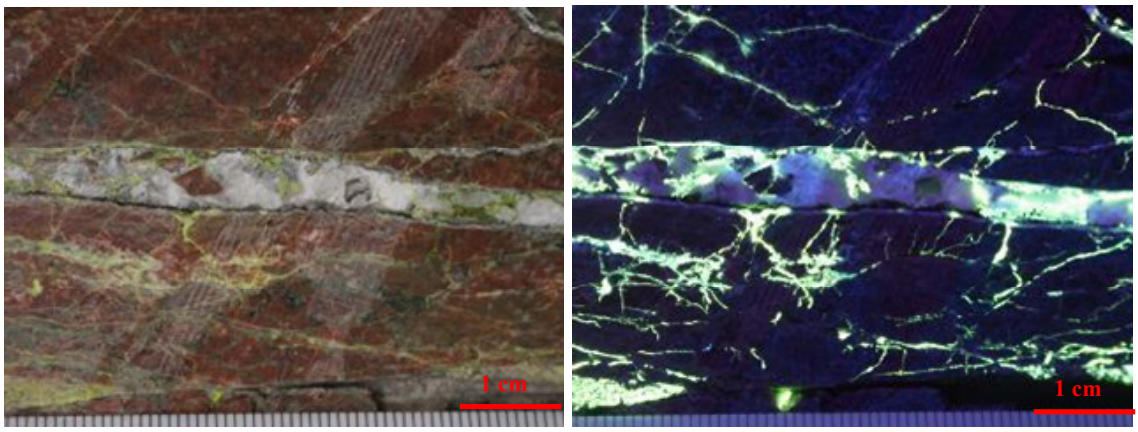

(a) (b)

Figure 2-13. *B2 image (detail of outer surface shown in Figure 2-3, frame size is 320×240 pixels) taken at (a) ordinary light and (b) UV light.*

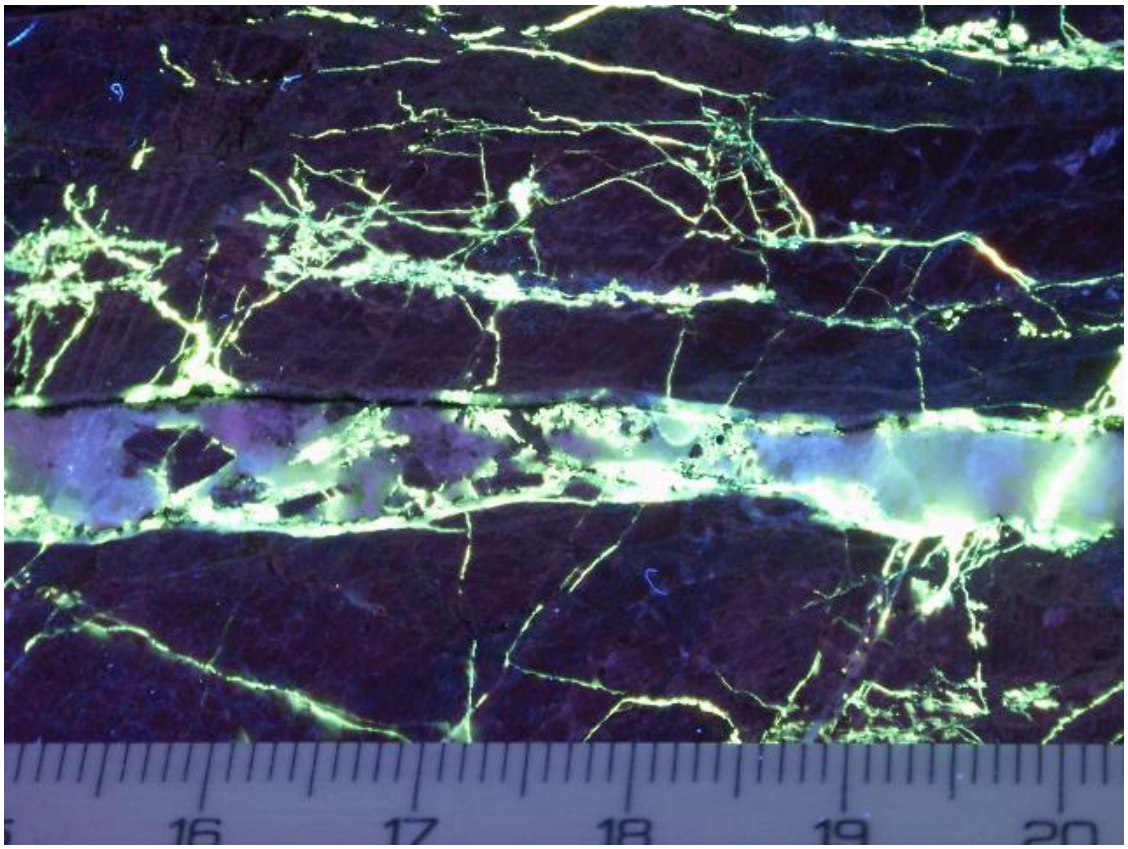

Figure 2-14. *B2 core plane, UV light image: resolution: 0.021 mm/pixel.*

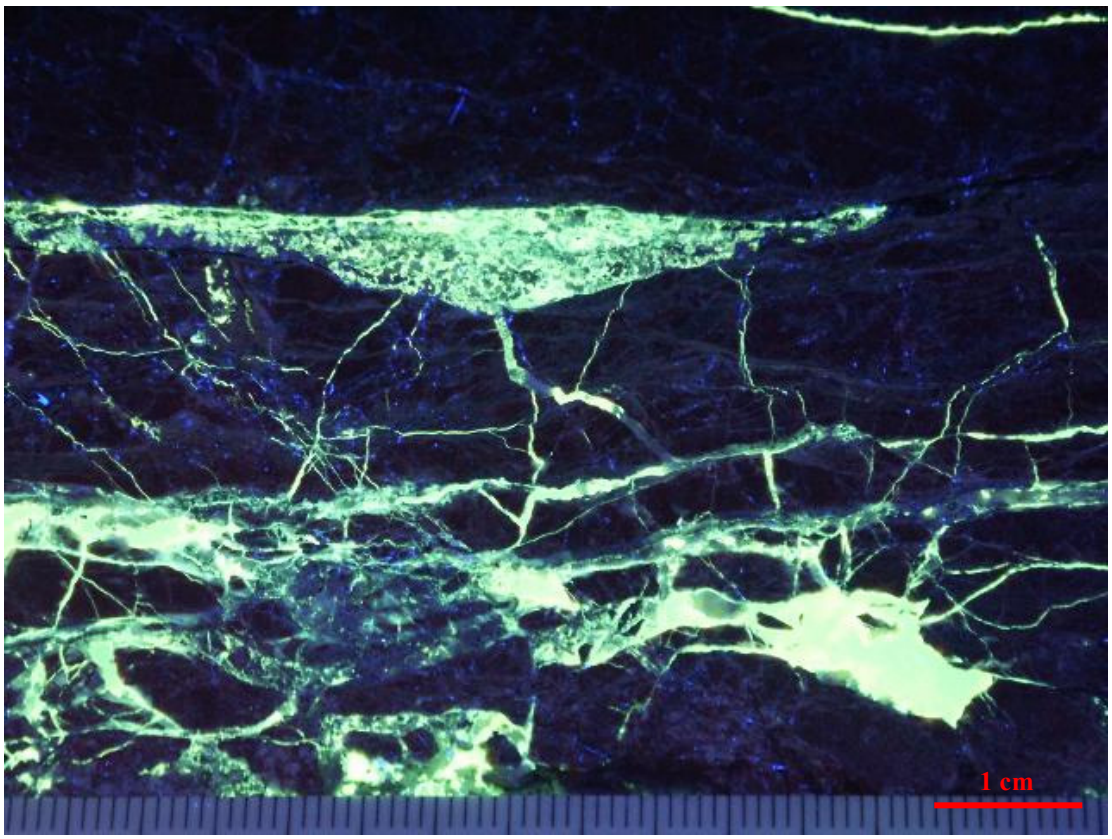

Figure 2-15. *B2 cutting plane, UV light image: resolution 0.029 mm/pixel.*

2.3 Image acquisition for B2 and B3 sample slices

In order to analyse the fracture network in three dimensions and to enable a 3D characterisation the samples were cut into slices. B3 was cut into 12 slices parallel to the first cutting plane, and B2 was cut into 7 slices parallel to the core axis plane (cf. Figure 2-3). The slice thickness is c. 18 mm. Since B2 and B3 are neighbouring samples, they were cut in orthogonal directions to allow assessment of anisotropy in the fracture network patterns. In Figure 2-16 the piles of slices for each sample are shown.

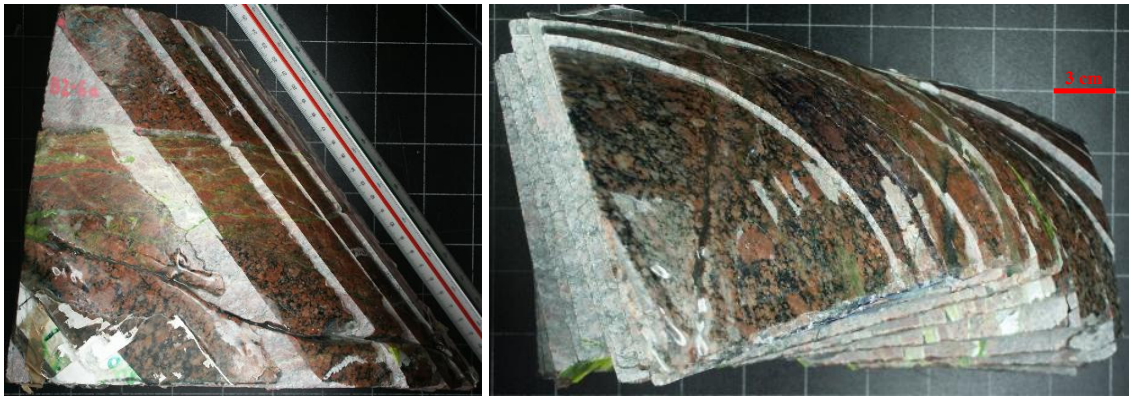

(a) (b)

Figure 2-16. *(a) B2 – 7 slices (b) B3 – 12 slices.*

For each slice, images were taken at three different scales (resolutions). All together more than 300 digital images were taken. The three scales are:

1. *"Overview slice resolution":* a slice is included in an image frame, the aim is to use it for overview and 3D construction, the resolution is about 0.12 mm/pixel, the size of slice is about 27 cm in length, one example is shown in Figure 2-17.

2. *"Main fracture zone resolution":* an existing fractured zone will be included in one full image frame, the resolution is about 0.06 mm/pixel, and the size of network is about 15 cm in length (see Figure 2-18). This is the scale used to calculate the main patterns and characteristics.

3. *"Complicated fracture network part resolution":* a part of fracture network is inside an image frame, the goal is to analyse more detailed information of the fracture network, the resolution is 0.02 mm/pixel, and the size of network is about 5 cm in length (Figure 2-19 to Figure 2-21). Because of the constraints imposed by paper size, the full resolution of these images cannot be displayed in this document. In order to illustrate the difference in image quality and accuracy a part of the images from Figure 2-19 are cut off and displayed in Figure 2-22 and Figure 2-23. This may provide the reader with some impression of the image quality and resolution that can be used for analysis.

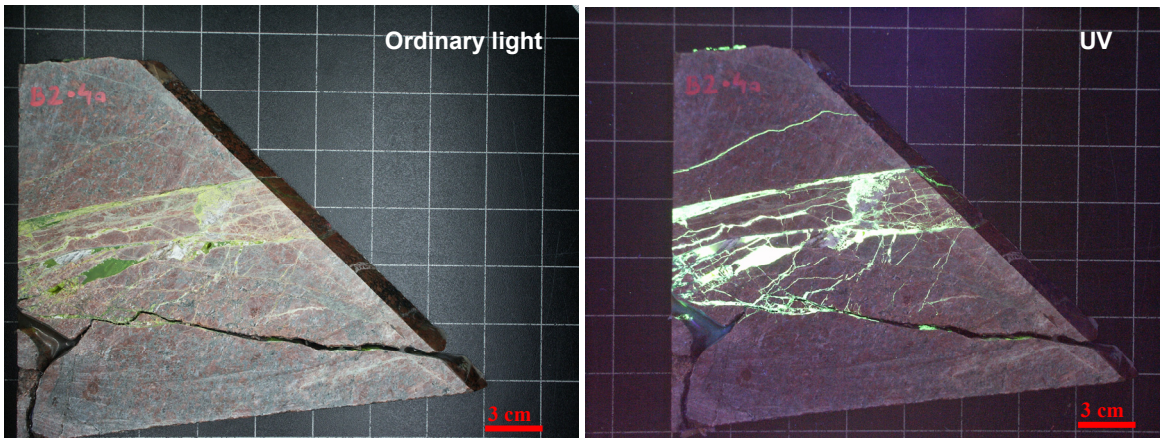

Figure 2-17. *B2-slice a4: "Overview slice resolution images" at ordinary light and UV illumination.*

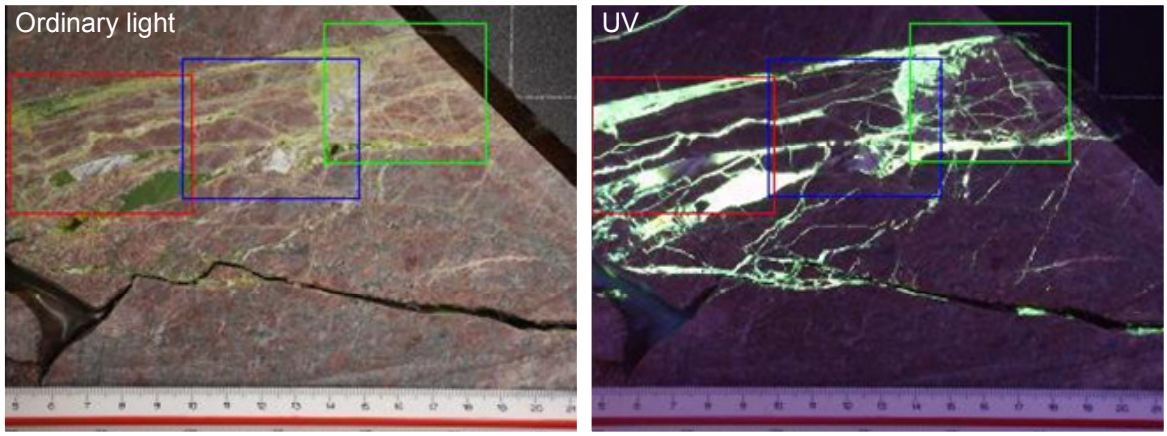

Figure 2-18. *B2-slice a4: "Main fracture zone resolution" images at ordinary light and UV illumination. The squares indicate the location of images taken at higher resolution, cf. Figure 2-19 through Figure 2-21.*

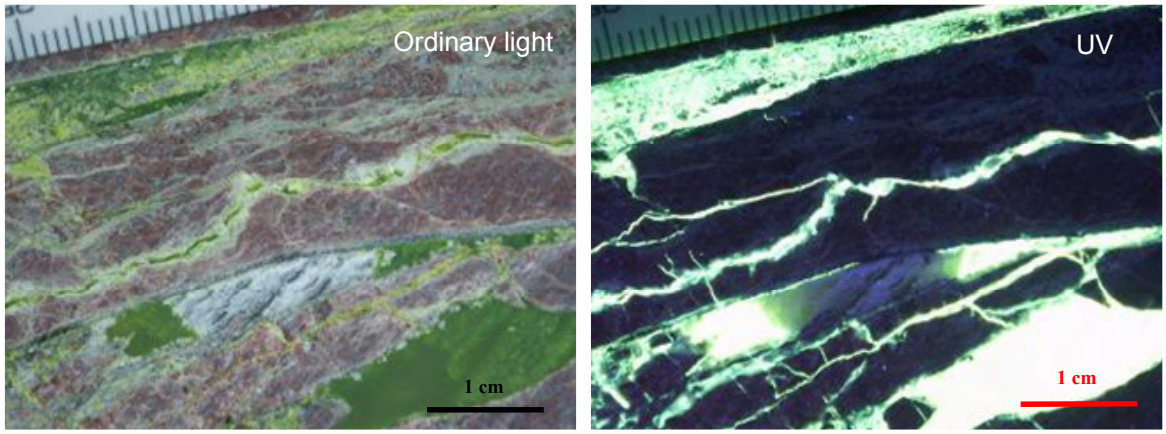

Figure 2-19. *B2-slice a4: "Complicated fracture network part resolution" images at ordinary light and UV illumination. These images correspond to the red rectangle in Figure 2-18.*

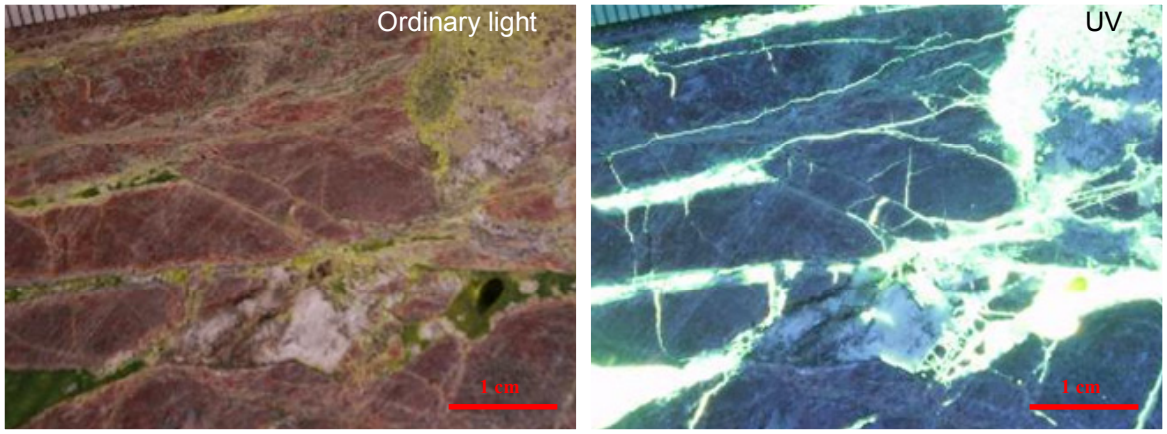

Figure 2-20. *B2-slice a4: "Complicated fracture network part resolution" images at ordinary light and UV illumination. These images correspond to the blue rectangle in Figure 2-18.*

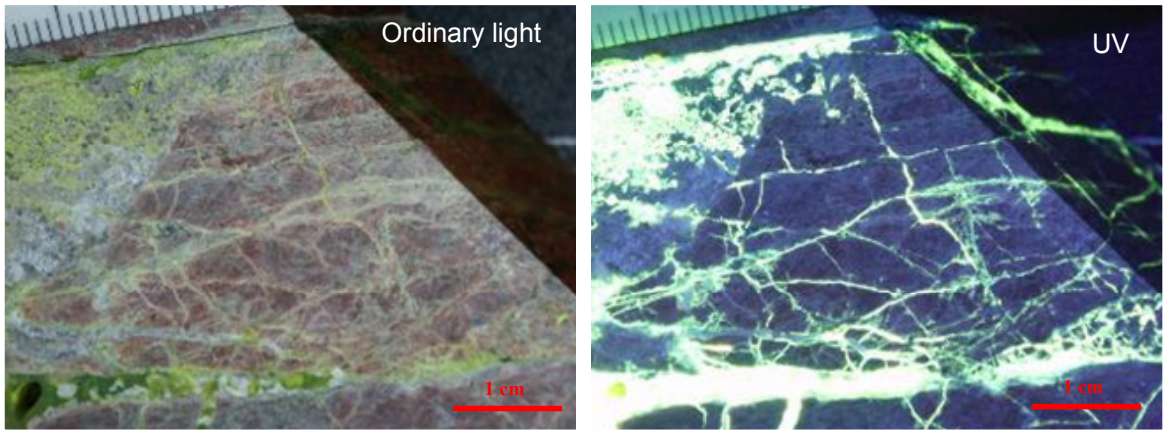

Figure 2-21. *B2-slice a4: "Complicated fracture network part resolution" images at ordinary and UV illumination. These images correspond to the green rectangle in Figure 2-18.*

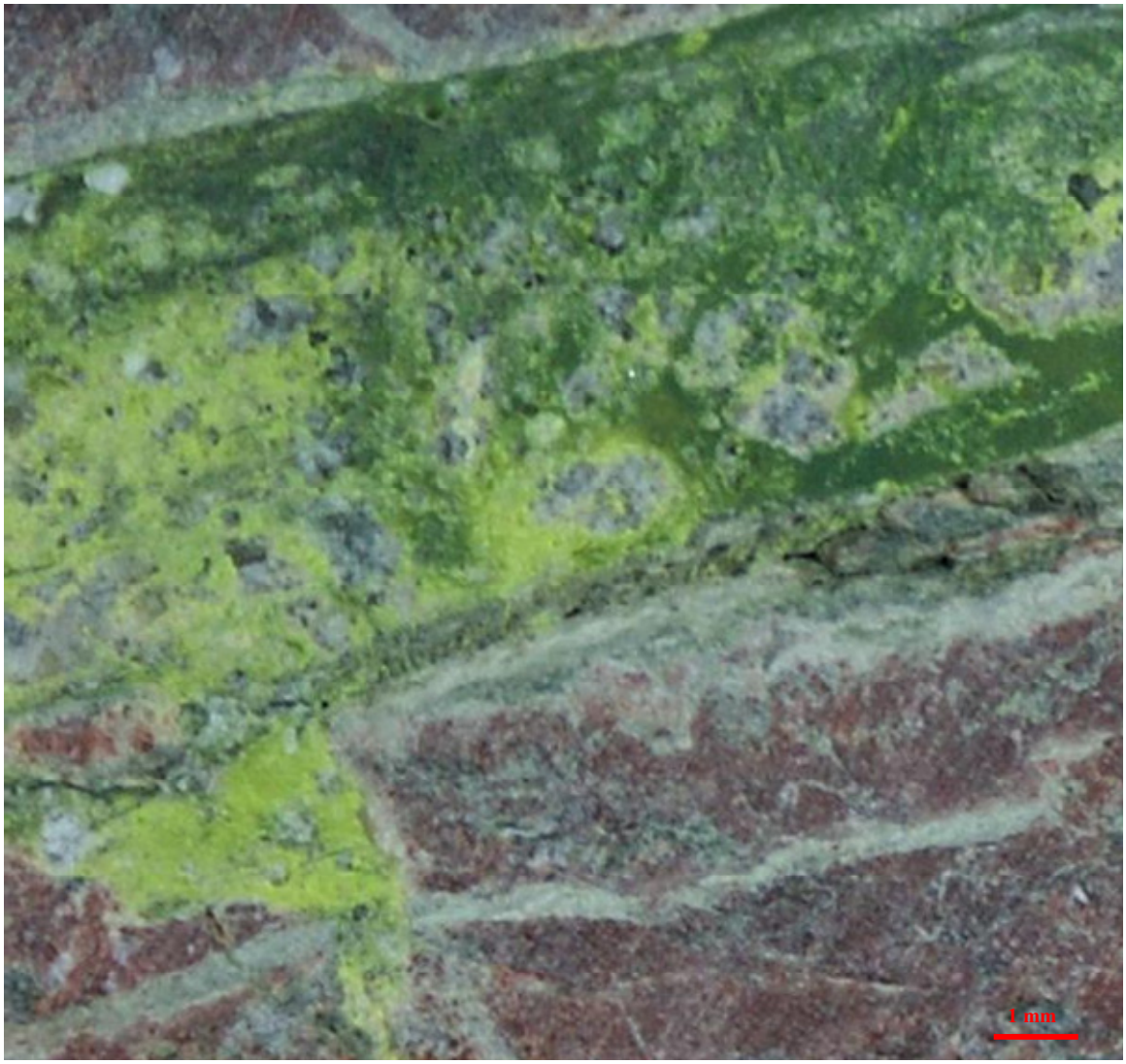

Figure 2-22. *B2-slice a4. Image at ordinary light, an excerpt of information from upper left corner of Figure 2-19.*

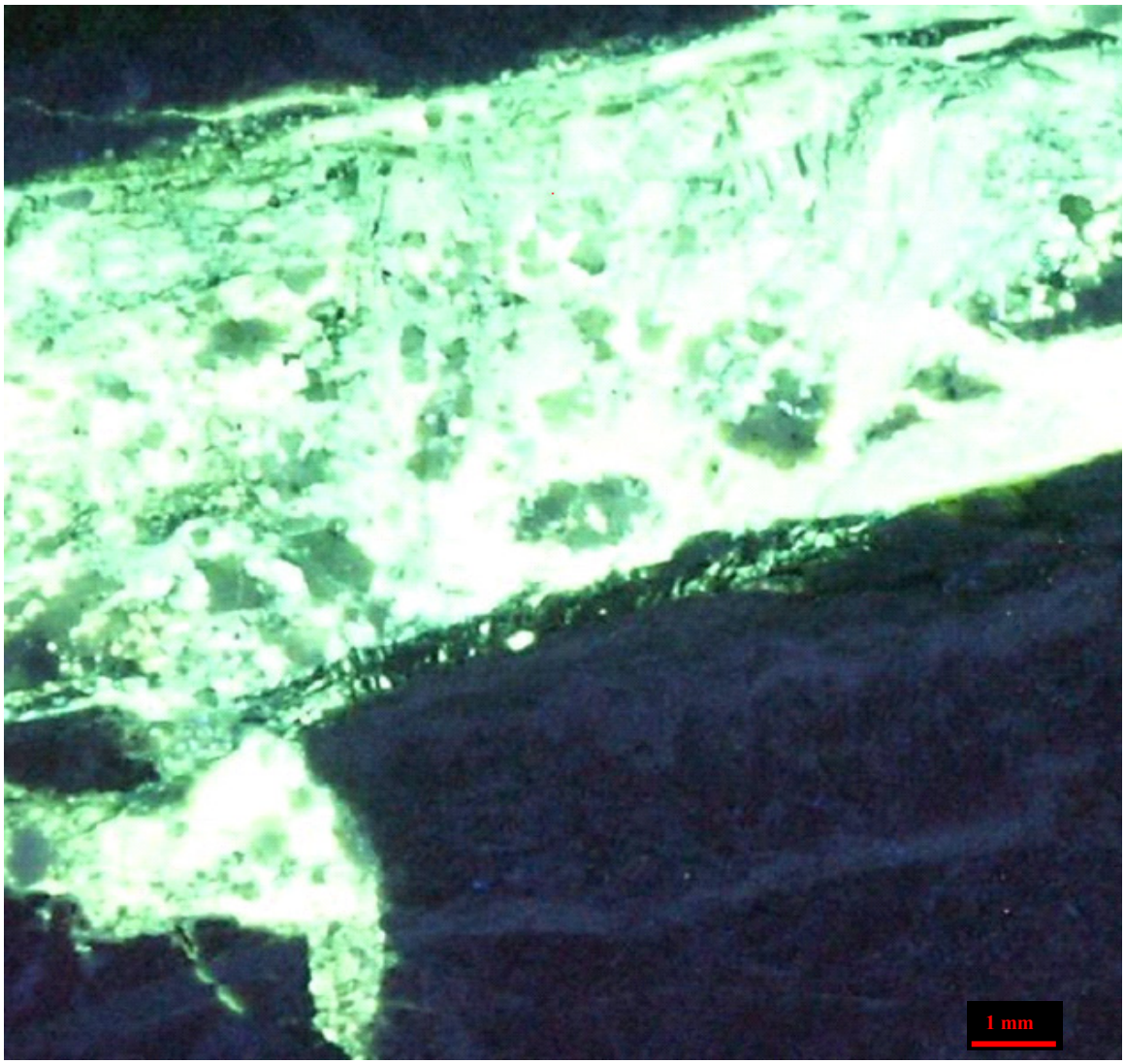

Figure 2-23. *B2-slice a4. Image at UV illumination, an excerpt of information from the upper left corner of Figure 2-19 (the same area as in Figure 2-22), the size of each pixel is 0.02 mm.*

2.4 Image acquisition using microscope

To analyse the fracture aperture and fracture microstructure, image acquisition using a microscope was tested. The following system was used:

1. A PC computer with a frame grabber, connected to a Fujitsu CCD colour camera (Resolution 720×576×24 bits, 24V, 50 Hz, 270 M, from Internvidea AB). The camera is connected to a ZEISS Stemi SV11 microscope, plan S1.0X.

2. For ordinary light illumination, the internal lighting system of the microscope (KL1500 electronic) was used. By using these lights, images can be acquired at maximum resolution. To identify fractures with epoxy clearly, two kinds of UV lamps were used, (a) Upland, MINI MODEL UVL4 and (b) Upland, UVL–56. The latter is much stronger than the former.

3. Images along fractures on the slice B2–4a were also acquired. The image resolution was about 0.0039 mm/pixel. Both ordinary light and UV illumination were used for image capture and different magnifications. Two examples, at different scales (resolutions), are shown in Figure 2-24 and Figure 2-25, respectively.

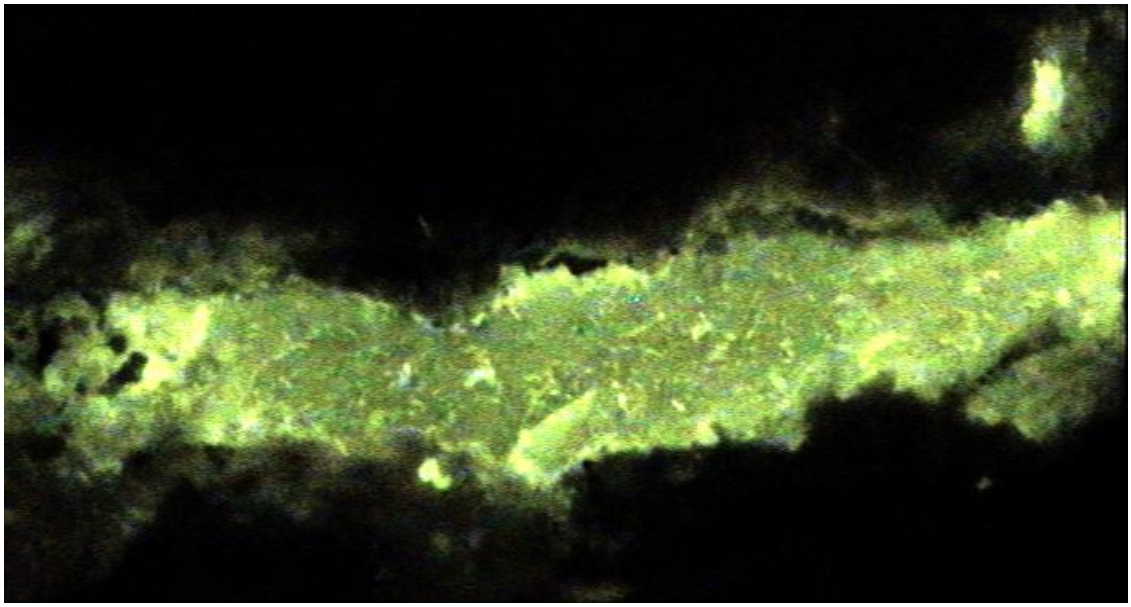

Figure 2-24. *B2 slice a4. Example of image acquired with microscope (fracture length is about 3 mm) at UV illumination. The image resolution is in this case 0.00426 mm/pixel.*

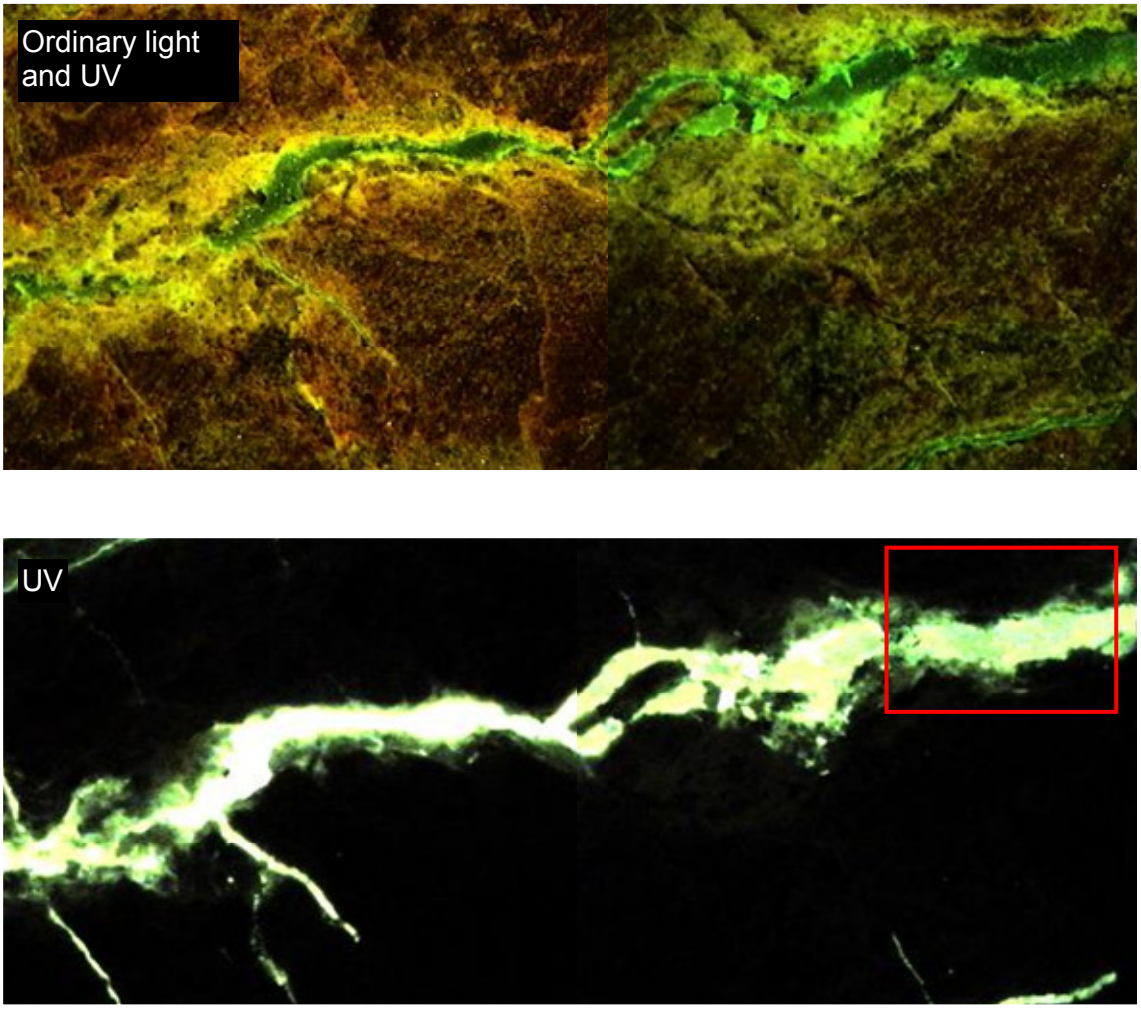

Figure 2-25. *B2 slice a4. Images taken by microscope using both ordinary light and UV lamps in combination (upper) and UV lamp only (lower). Two neighbouring frames are merged. The resolution is about 0.01 mm/pixel. The red square shows the location of the close-up image in Figure 2-24.*

2.5 Suggestions for future image acquisition

Since the time available for image capture was limited, no constant illumination environment for the image acquisition was established, and therefore the image quality was not stable. Sometimes, it was very good and sometimes not satisfactory even if the same acquisition equipment was used. This instability was mainly caused by changes in the extra lighting conditions. Therefore, for future acquisition with set high quality requirements, a simple shielded illumination box is recommended.

So far, digital cameras with magnification 4X and 7X have been tested, where the image resolution can be up to 0.022 mm/pixel. However, there are commercially available digital cameras with magnification up to 20X. The image resolution taken by a good digital camera (say 4,000×4,000 pixels) can thus be as high as 0.01 mm/pixel even when the images can cover a fairly large view area (ca 4 cm side). Microscope images, on the other hand, in our case only had 720×576 pixels. The relatively large view area of digital cameras makes them good for fracture network characterisation. Based on the

experiences from the analysed rock slices in this study, it is better to use the proposed shielded illumination box and a new digital camera for taking fracture images for further processing and analysis.

In this study, aperture analysis was applied only to a few fractures. The results of the testing showed the prospects for measurement and analysis. Microscope imaging is useful for analysis of a single fracture, and here, the image resolution (0.003 mm/pixel) cannot be matched by the digital camera. It would be advantageous to acquire more close-up fracture images for analysis using the slices produced to improve the general impression of the porosity and distribution of pore space of fracture and associated fine materials in crystalline rock. Micro image acquisition is very sensitive to the specimen movement relative to the camera. Ordinarily, thin sections are used for the microscope. However, in our case, the specimen is not a thin section, and the fracture continuity between images (orientations and end points are not necessarily matching one another) are difficult to achieve due to the movement of the specimen relative to the camera. It may be practical to construct a mechanical device for image acquisition using a microscope if decided to collect a large number of micro images.

3 Image processing and fracture detection

This chapter provides an overview of the current status of rock fracture image processing research, followed by a brief description of visual rock fracture properties and an attempt to classify the types of rock fractures. Finally, the work done on image processing within the current project is summarised.

3.1 Image processing of rock fractures in the literature

For multiple fractures on an image /Reid and Harrison 2000/ presented a semi-automatic tracing method for rock fractures. /Lemy and Hadjigeorgiou 2003/ developed an auto-tracing method for rock fractures based on edge detection and neural networks. /Soroushian et al. 2003/ proposed an algorithm for fracture image binarisation of their laboratory SEM images. Similar image analysis has been done by /Kemeny and Post 2003/, /Wang and Stephansson 1997/, /Lee and Kim 1995/, /Wang and Pavlidis 1993/, /Harrison 1993/, /Sun et al. 1992/, /Hu et al. 1992/, /Whittaker 1992/, /Tanimoto et al. 1989/ and /Franklin et al. 1988/. For three-dimensional assessment, work has been done by /Kemeny and Post 2003/ and /Dingxiang et al. 1986/. /Lyman 2003/ has used neural networks techniques to detect fractures.

In Sweden, with special application to the bedrock at the Äspö HRL, /Johansson 1999/ presented three different algorithms for single rock fracture or crack detection. /Feng 1996/ used the BIPS system for acquiring borehole images, and studied measurements of the orientations of single joints in a borehole, and other fracture properties. In the BIPS system, rock fractures (and associated envelope curves) are traced based on input points (the more points, the more accurate the tracing), to fit theoretical sinusoidal curves. The applied interpretation technique does not include elements of image processing or matching algorithms, and colour or grey scale information is not required.

/Hakami 1995/ presented a method to measure aperture and roughness of single joints, using an image analysis technique and also analysed the relationship between aperture (distribution) and hydro-mechanical characteristics.

3.1.1 Visual properties of rock fracture and classification for image segmentation

Fractures or cracks belong to the group of so-called “thin curved objects”, i.e. the length of the object is much longer than the width. The fracture or crack may be empty or filled with different materials and the filling materials could have different colours. Most often, tracing of rock fractures on rock surfaces is difficult since the surfaces are rough and both the colour and the intensity of light vary along the fracture. Therefore, since the fracture thickness (aperture) and colour vary greatly, it is expected that this result in many “gaps” in the imaging of fractures. If the image includes multiple fractures they may form a complicated network with fractures crossing each other. All these properties make image analysis of fracture images a hard task compared to many other applications. Figure 3-1 to Figure 3-3 shows some examples of rock fracture images at different scales.

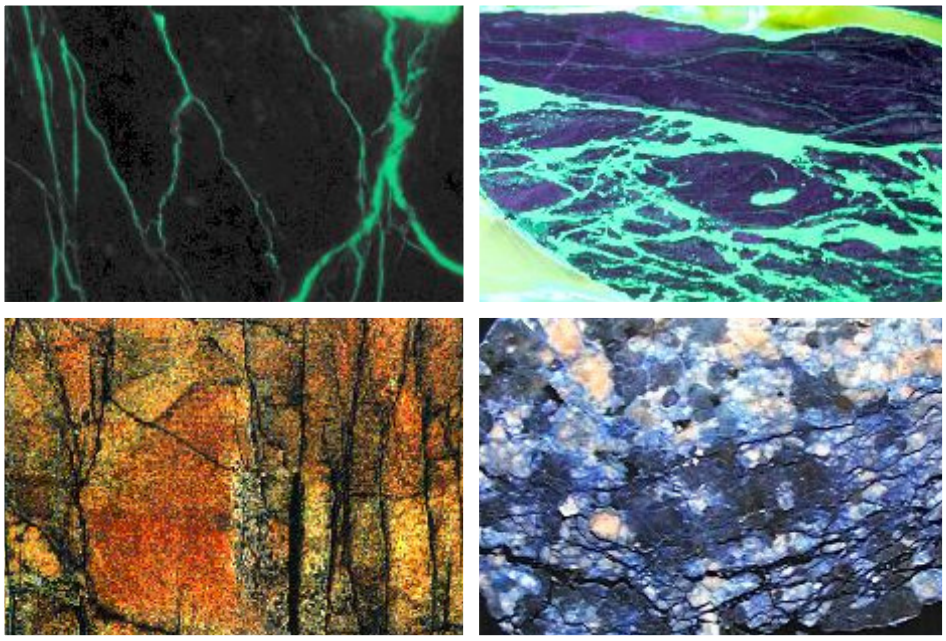

Figure 3-1. *Fracture types: The two top images are fluorescent epoxy-filled micro fractures (fractures are brighter), the bottom-left image is a natural fracture image at a large scale, and the bottom-right is an image on centimetre scale (fractures are darker).*

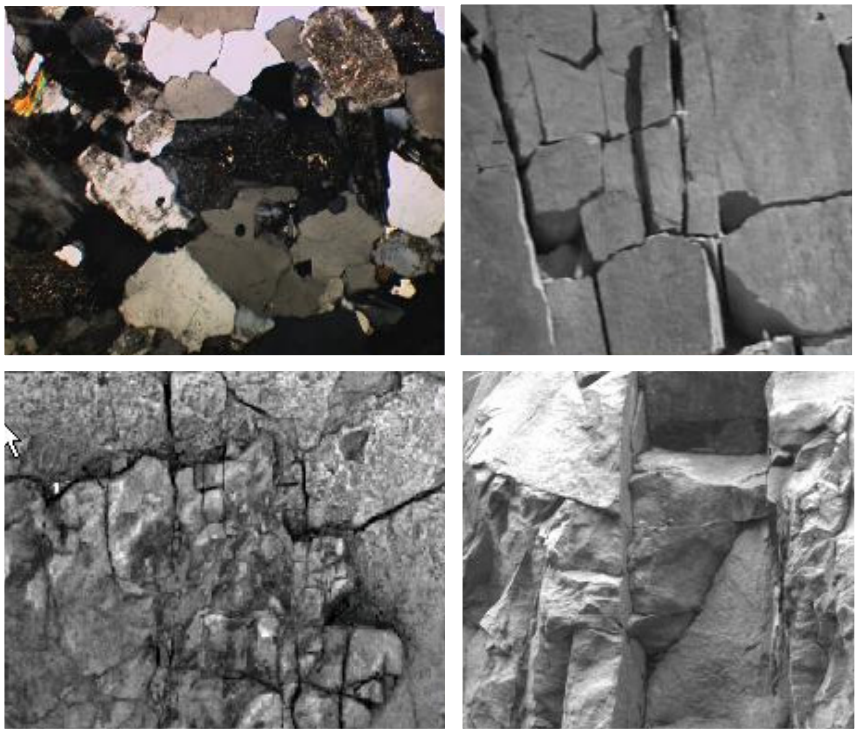

Figure 3-2. *Rock is divided into "blocks" by fractures or mineral grain boundaries.*

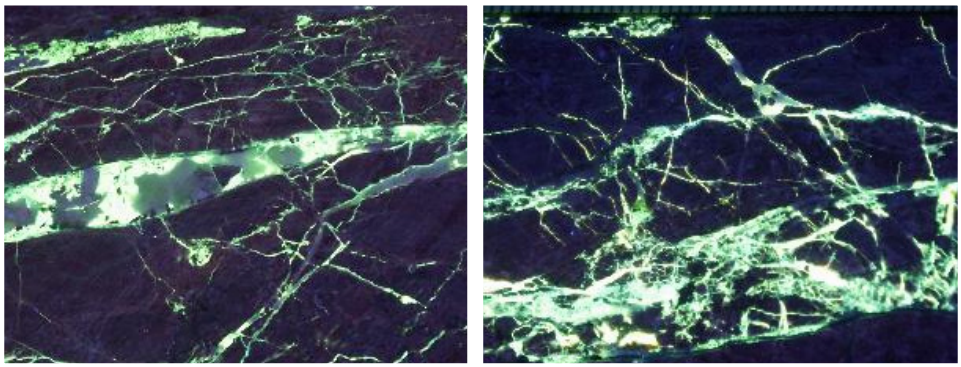

Figure 3-3. *Image examples from this study (about 7 cm and 5 cm in width). Thanks to the fluorescence epoxy a comparatively high contrast between fractures/pores and surrounding rock is achieved, which facilitates analysis significantly.*

3.2 Image pre-processing

The aim of image pre-processing is to enhance images for better visualisation and processing. Image pre-processing techniques can be classified into global operators and local operators /Huang et al. 2005/. Linear contrast stretch and histogram equalization are two of the most widely used global operators. Adaptive histogram-equalization, contrast-limited adaptive histogram equalization, kernel filters, morphological functions and multi-scale enhancement belong to the local operators. While the global methods use a transformation applied to all the pixels of the image, the local operators use input-output transformation that varies adaptively with the local characteristics of the image. The above types of image pre-processing can be expressed as:

Global operators: $f_{new}(x,y) = Trans\left(f_{original}(x,y)\right)$

Local operators: $f_{new}(x,y) = f_{original}(x,y) - Filter(x,y) + Const.$

Image enhancement algorithms are designed to process a given image such that the result is better than the original image and optimised for the applications or objectives. When the objective is to improve perceptual aspects, desirable image pre-processing can be performed by contrast or dynamic range modification. In this study, to enhance the fracture images for further processing and segmentation, both methods have been attempted. The methods applied are briefly introduced in the following sections.

3.2.1 Image conversion from colour to grey scale

A grey scale image $f(x,y)$ has $L(i = 1,2,..,l \le 256)$ possible grey levels (i.e. intensity levels) one value in each image pixel (x, y are the pixel coordinates on the image plane).

A colour image (RGB) is a combination of three images: $F\left\{f_r(x,y), f_g(x,y), f_b(x,y)\right\}$.

If one converts a colour image to a grey scale image, a general conversion equation can be given as:

$$F \Rightarrow f(x,y) = \alpha \cdot f_r(x,y) + \beta \cdot f_g(x,y) + \gamma \cdot f_b(x,y),\ (\alpha + \beta + \gamma = 1)$$

As in the example if Figure 3-4, a given colour image may be divided into the three RGB (Red, Green and Blue) images. It may be noted that the three images are different. In general it depends on the image itself, and the objective of the analysis, which colour is most useful. In this example the green and the red colour images give clearer images than the blue colour.

In Figure 3-5, the same colour image is instead split into three images.

RG ($\alpha + \beta + \gamma = 0.5 + 0.5 + 0.0 = 1$)

RB ($\alpha + \beta + \gamma = 0.5 + 0.0 + 0.5 = 1$)

GB ($\alpha + \beta + \gamma = 0.0 + 0.5 + 0.5 = 1$)

Each of these images is a combination of two colour channels. In this example, the Red-Green image shows the fracture clearer than the others.

Except for RGB, a colour pixel can also be divided into the three values of intensity (I), hue (H) and saturation (S), which is another way to represent a colour image. An example is shown in Figure 3-6. For fractures, it seems that the best image may be the combination of light intensity and colour hue (HI).

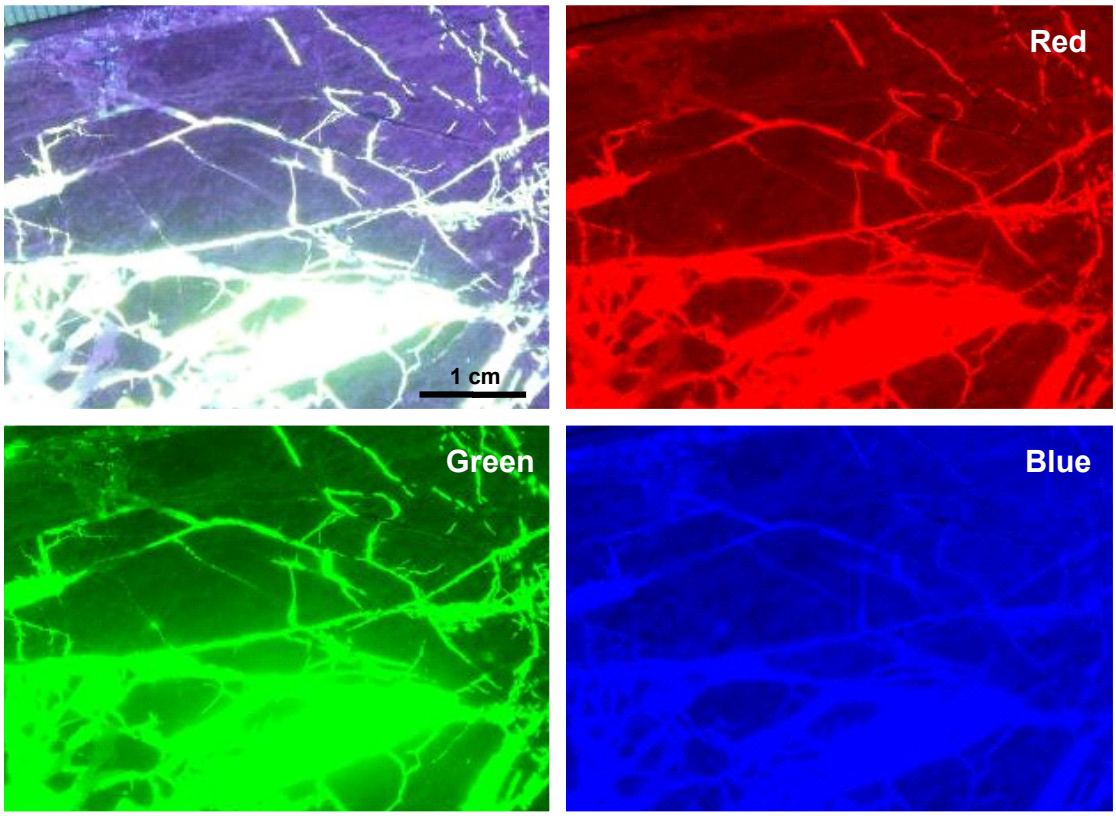

Figure 3-4. *A fracture image in colour is split into three images, RGB (Red, Green and Blue).*

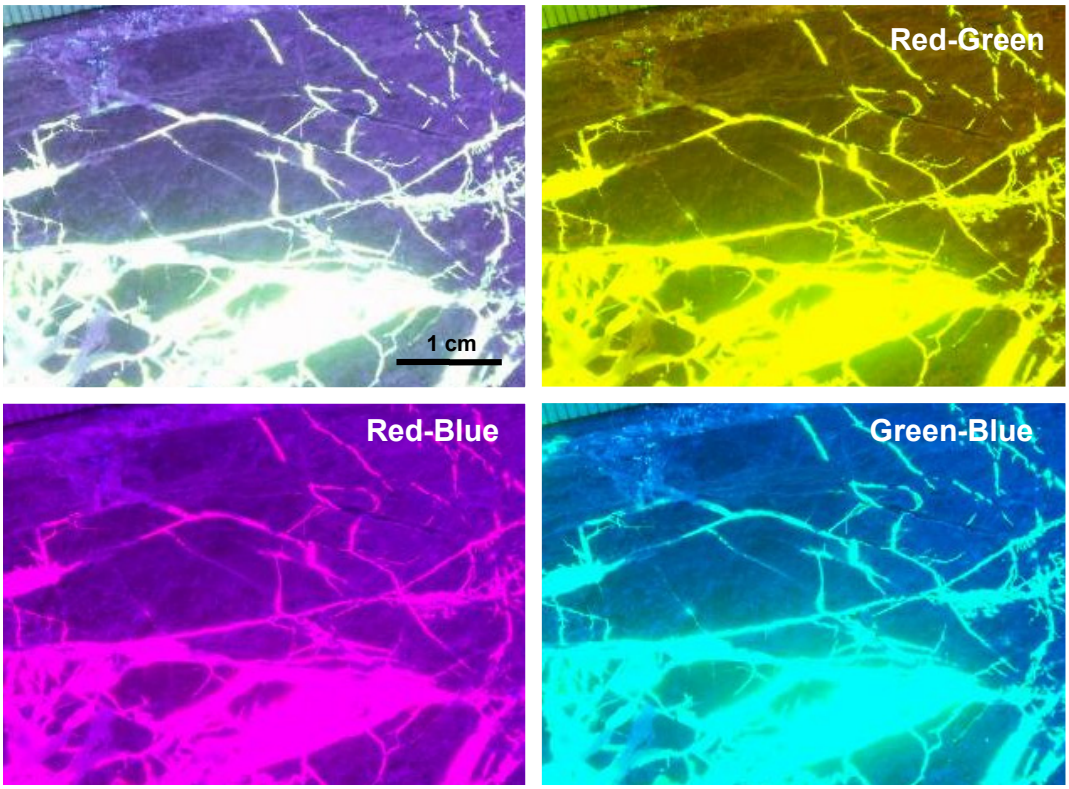

Figure 3-5. *A fracture image in colour is split into three images; RG, RB and GB.*

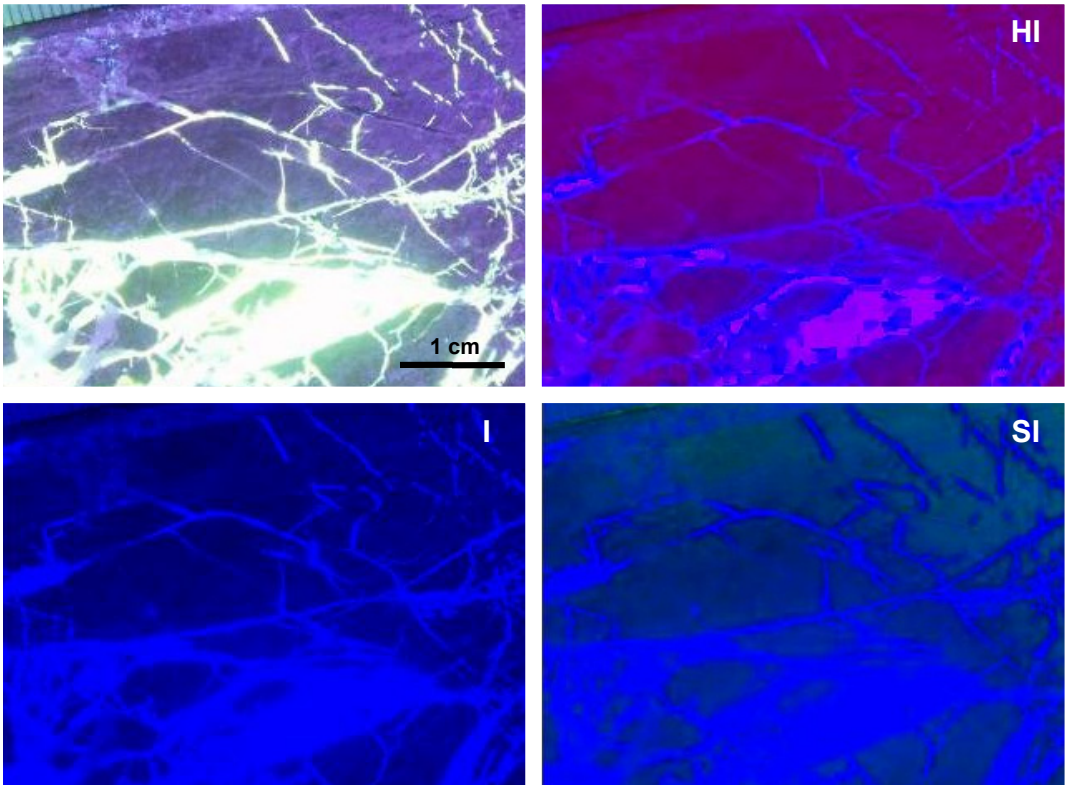

Figure 3-6. *A fracture image in colour is split into three images; HI, I and SI.*

When a colour image is to be converted to a grey scale image, the new image pixel value can also be calculated based on the RGB values or IHS values in different ways. Figure 3-7 shows how the earlier discussed colour image is converted into a grey scale image by using minimum or maximum RGB values, i.e. for each image pixel, checking its RGB values and choosing the minimum or maximum value of the three values from red, green or blue, as input for the new image. In our application example, it is obvious that conversion using minimum values is the better one.

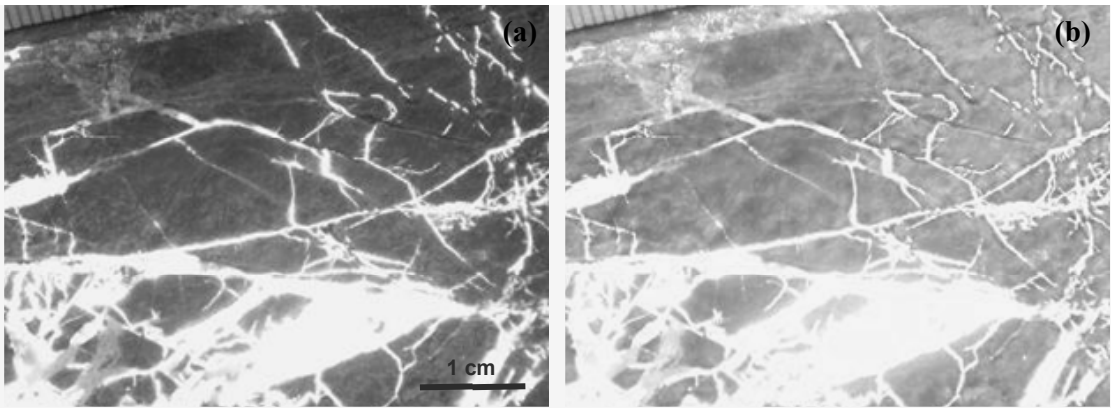

Figure 3-7. *The fracture image in colour (cf. Figure 3-4 through Figure 3-6) converted to a grey scale image. (a) Converted by using minimum RGB values, and (b) Converted by using maximum RGB values.*

A colour image includes a lot of information, some information is useful, and some cannot be used, depending on the requirements of the image processing and analysis. All the image-conversion methods belong to the global operators group. In our study, since only grey scale image segmentation has been considered, colour information has not been used so far. To obtain a grey scale image, the colour image was converted directly by using the minimum operator on the combined GB (green and blue) image. To fully make use of all available colour information, more tests and studies are needed.

3.2.2 Comparison of image pre-processing operators

No matter whether one has a colour image or a grey scale image, a number of image pre-processing operators can be used for image enhancement. For grey scale images, the operator acts on one image, and for colour images the operator acts on three images, RGB, respectively. Due to our rock fracture characteristics, several widely used operators were tested on the images. Based on our utilities, the tested operators were classified into two types: one is image noise removal, and the other is for sharpening rock fractures in images.

In Figure 3-8, five different operators are compared for a colour rock fracture image:

(b) The operator is a 3×3 kernel with a median filter operation (local operator). In this new image, the noise points and lines are removed, but the image is blurred.

(c) Morphological operation (local operator) – simple opening and closing, the operation result is similar to the median filter, it may be somewhat better for removing noise lines or curves.

(d) Linear stretch (global operator) – stretching the range of grey scales, it makes the intensity contrast higher.

(e) Sharpening (local operator) – it makes the fracture sharper, but noise arises.

(f) Exponent transformation (global operator) – it decreases the grey values of the non-fracture regions.

For our images, the operators of exponent transformation, linear stretch and median filters have been used in most cases. Since this project is a first test of the methodology, an automatic procedure for enhancement of the rock fracture images has not been applied. Such auto-procedures may be developed based on the requirements of further processing-image segmentation (fracture delineation and/or tracing).

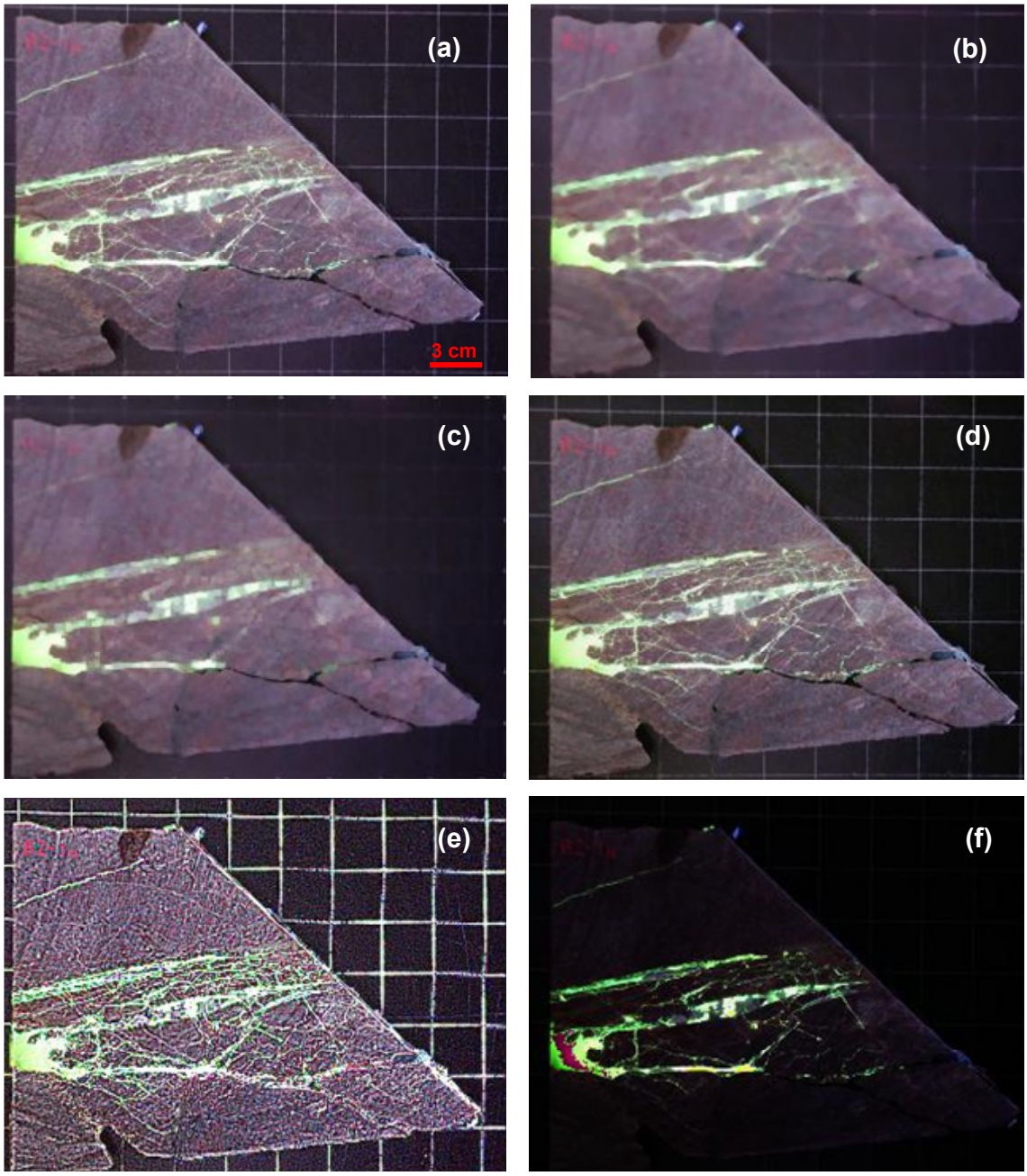

Figure 3-8. *Comparison of image pre-processing operators: (a) Original image; (b) Median filter; (c) Morphological operation; (d) Linear stretch; (e) Sharpening and (f) Exponent transformation (see text).*

3.3 Fracture delineation or tracing

After image pre-processing, the next step is image segmentation and fracture tracing. The image segmentation is an old topic of image analysis and pattern recognition. The current line of approach is to combine different image segmentation algorithms depending on the application, in our case single rock fractures or a fracture network.

3.3.1 Image thresholding

Selection of thresholding algorithms

Thresholding is one of the existing, simple, popular and most important approaches to image segmentation. From our literature review, the thresholding algorithms can be classified into two groups /Otsu 1979/, /Fu and Mu 1981/, /Pal and Pal 1993/, /Lee and Chung 1990/, /Groenewald et al. 1993/, /Sonka et al. 1995/, /Tsai 1985/ and /Kapur et al. 1985/. One group is based on the characteristic feature (e.g. grey level) histogram. The other is based on the gradient (or Laplacian) of an image. The main global thresholding algorithms summarised in the literature include: Optimal thresholding (OPT), Between class variance (BCV), Entropy, Moment preserving, Bi-modes (the threshold is a valley point between two main peaks) – here denoted BIM, Edge based thresholding (DIFF), dynamic edge based thresholding (DYN). /Lee and Chung 1989/, evaluated five of the global thresholding algorithms, namely OPT, BCV, Entropy, Moment preservation and Quadtree. They came to the conclusion that Entropy and Quadtree are sensitive to image characteristics such as contrast and histogram distribution.

In order to evaluate how useful these global algorithms (abbreviated OPT, BCV, BIM, DYN, and DIFF), are for our application, they have been implemented in a computer program.

The implemented algorithms are:

1. OPT /Groenewald et al. 1993/
2. BCV /Sonka et al. 1995/
3. DIFF /Kapur et al. 1985/
4. DYN, similar to DIFF, the difference being that the threshold value is not constant over the whole image. It varies from place to place.
5. BIM /Otsu 1979/, /Fu and Mu 1981/ and /Groenewald 1993/

In order to evaluate the performance of the above five thresholding algorithms for rock fracture images some test images were selected for further analysis. These images are representative for fracture analysis applications, and the fractures and background can roughly be distinguished by the human eye (e.g. background is darker than fractures). The test images are of the size 320×240 pixels uniformly quantified to 24 bits. Our four test images are shown in Figure 3-9 and their histograms are shown in Figure 3-10, respectively. The image in Figure 3-9(a) was taken from a slice with two long fractures, its histogram, having a shape of a normal distribution. In Figure 3-9(b), the image is a microscope image with one fracture and there are no obvious dual peaks in the histogram. Figure 3-9(c) is an image of a slice, its background being rough, where there

are many fractures forming a network. Figure 3-9(d) shows an image of a part of a cylindrical outer surface, with much noise, and the fracture network being very complicated. Figure 3-10(a)-(d) shows the histograms of the corresponding images in Figure 3-9(a)-(d). Most of the histograms seem to be bimodal (with two principal peaks) but their shapes being very different.

One of the most difficult problems in comparing and evaluating the performance of thresholding algorithms is the selection of a meaningful object performance criterion. A criterion suitable for one application may not be suitable for another. In this application with measurements on epoxy filled fractures, the most important concern should be the accuracy in the segmentation. In evaluating the performance, the probability of error in size and uniformity, which are relatively easy to observe by the human eye, may be set as criteria. The evaluation made was simply based on a comparison by the human eye, which was judged to be sufficiently useful for the current work.

As seen from several tests, OPT and BCV operations will give a similar result on any of our rock fracture images. Therefore, in the Figure 3-11 through Figure 3-14, OPT, BIM, DIFF and DYN operator results are given on each image in Figure 3-9 for comparison.

The results of the testing show (Figure 3-11 through Figure 3-14) that OPT works on all of the four images, BIM works on the image of a two mode (peaks) histogram, DYN may work for the images with a complicated fracture network, and DIFF is sensitive to the information variation of rock fracture images.

Based on the result of the testing, OPT or BCV were chosen for all the rock fractures. Figure 3-15 demonstrates four other typical image thresholding results by using the BCV algorithm.

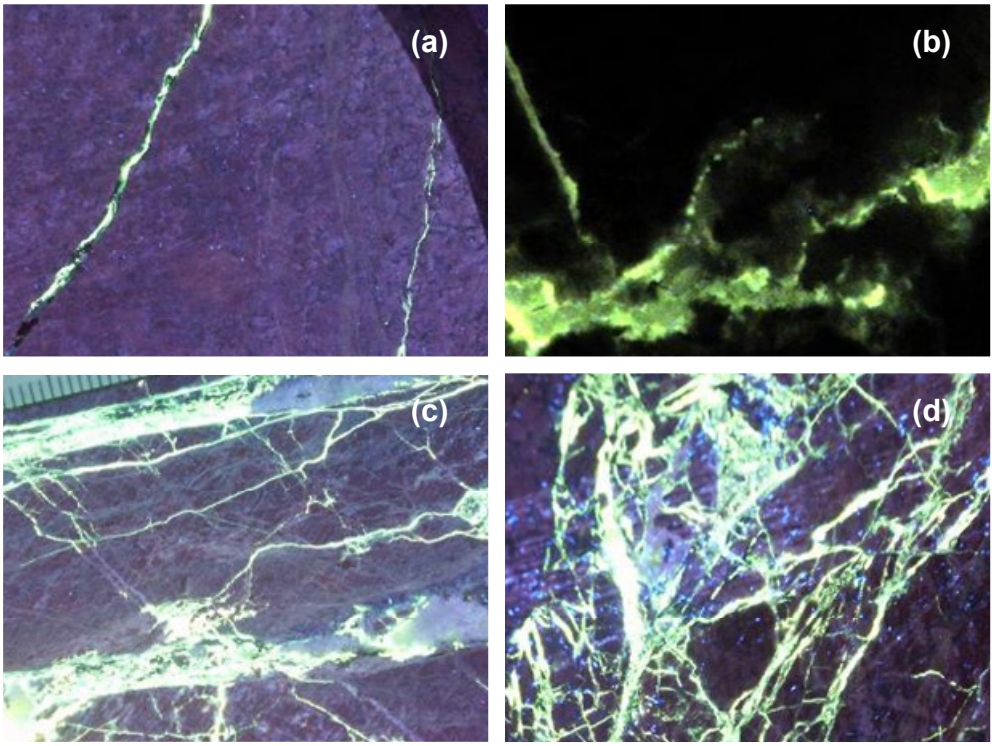

Figure 3-9. *Four typical rock fracture images of different scale and character.*

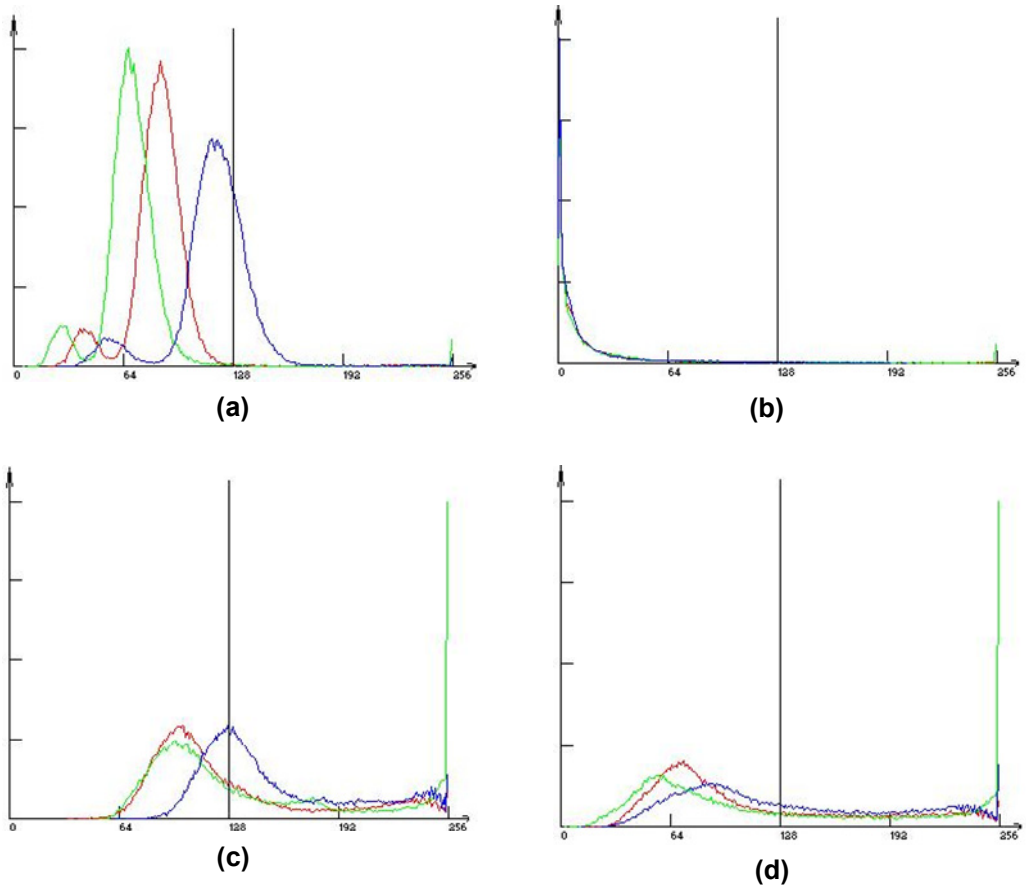

Figure 3-10. *Histograms for the RGB images in Figure 3-9 (Intensity on the x-axis and frequency on the y-axis), respectively.*

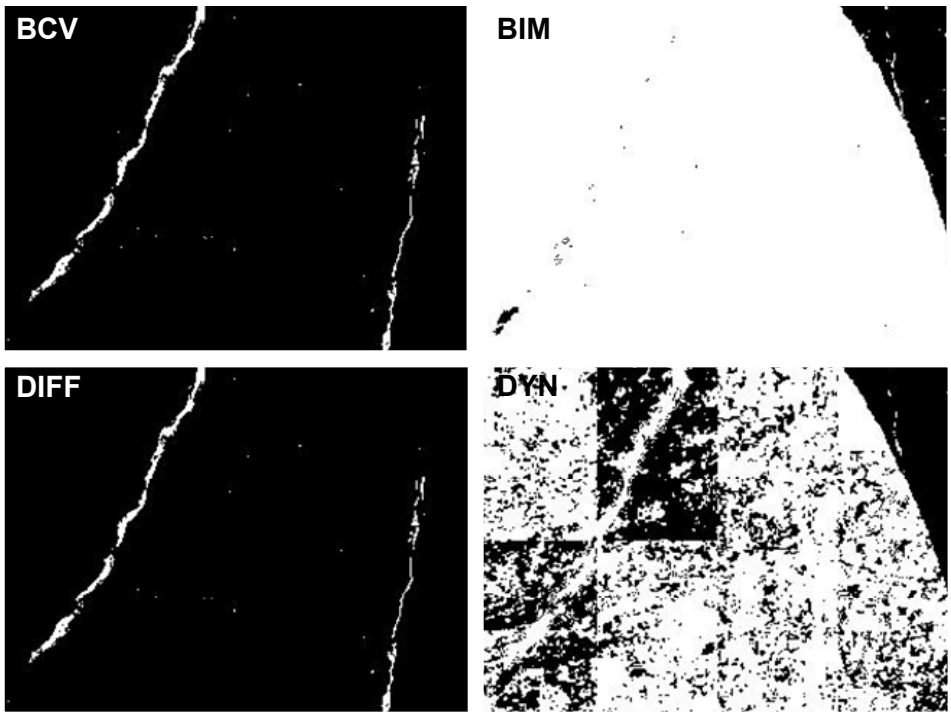

Figure 3-11. *Results of four thresholding algorithms applied on the image (a) in Figure 3-9: Notable is that BIM and DYN fail.*

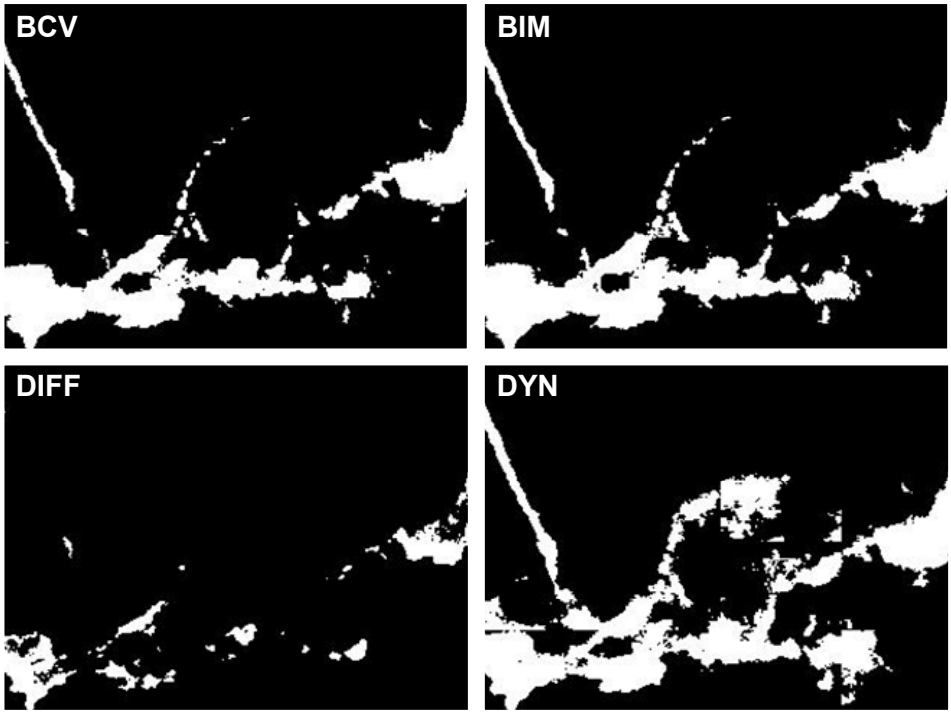

Figure 3-12. *Results of four thresholding algorithms applied on the image (b) in Figure 3-9. DIFF failed, and DYN gives a fracture area larger than what can be detected by the human eye.*

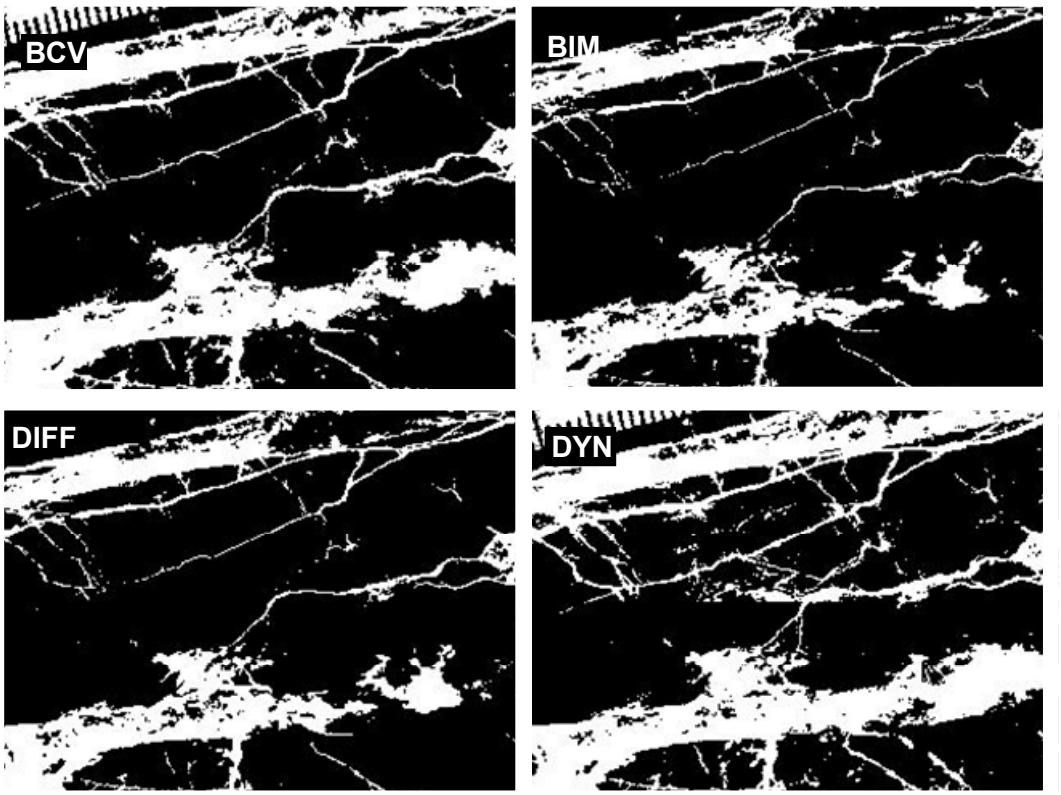

Figure 3-13. *Results of four different thresholding algorithms applied on the image (c) in Figure 3-9. All the operations seem to give fairly similar results, except for the handling of the measuring tape in the upper left corner.*

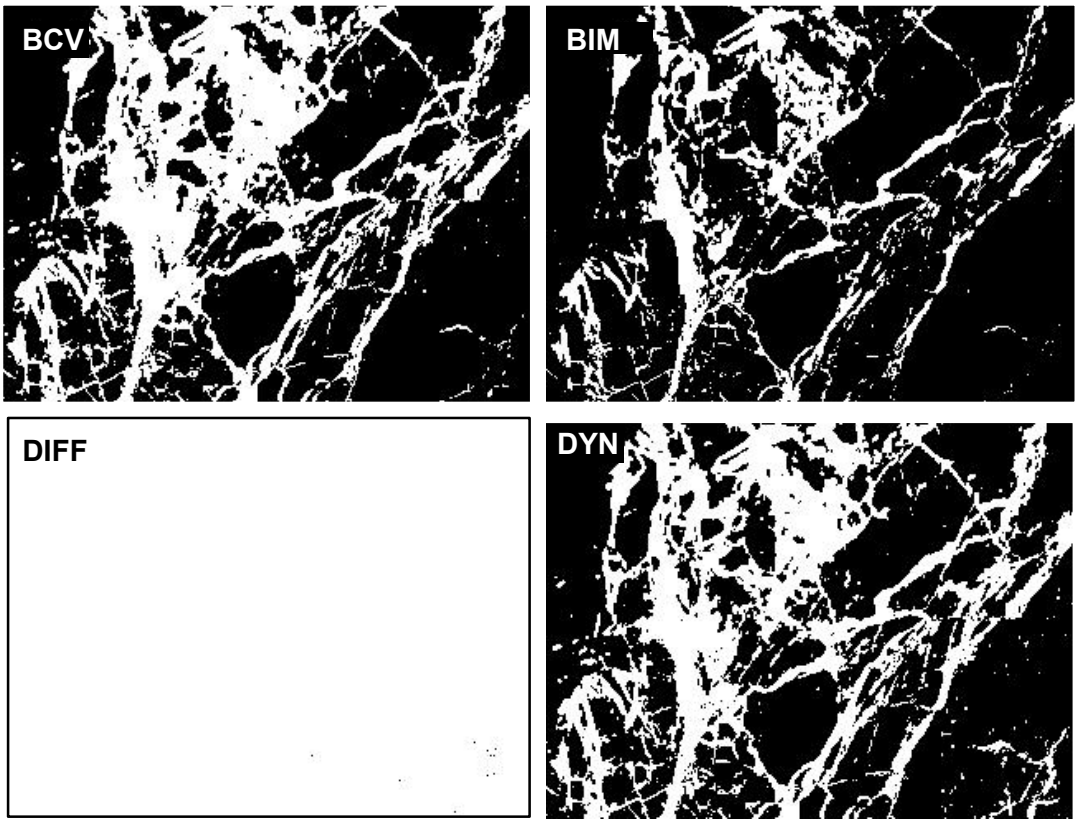

Figure 3-14. *Results of four thresholding algorithms applied on the image (d) in Figure 3-9. Notable is that DIFF fails completely.*

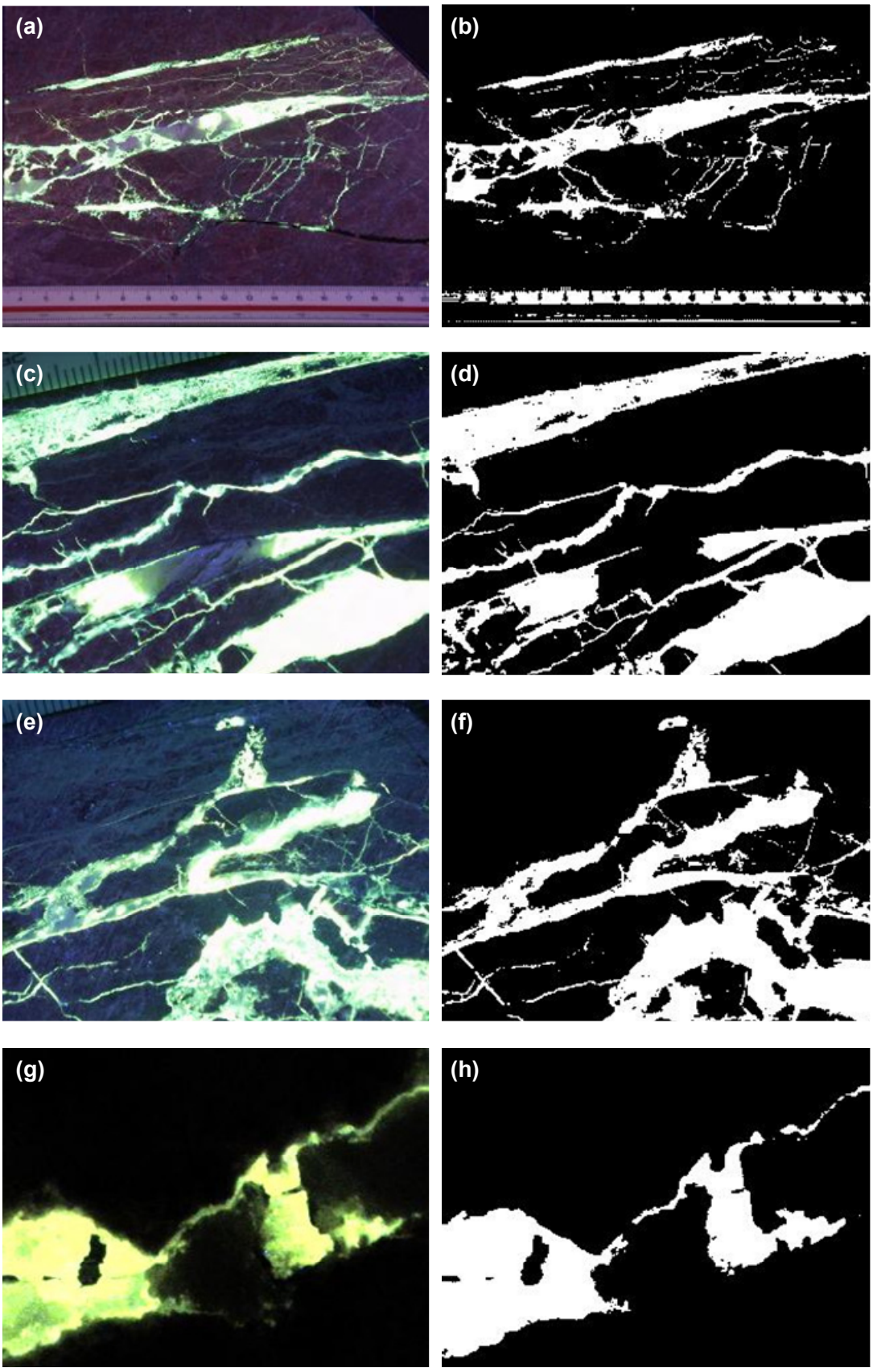

Figure 3-15. *BCV algorithm on the four typical rock fracture images in Figure 3-9; the detection of epoxy by the human eye in the left column of images can be compared with the detection as a result of the BCV threshold.*

Conclusions regarding thresholding algorithms

For a rock fracture image with a rather uniform background, and a range of grey levels of fractures being not too large, the algorithms OPT and BCV are good choices for performing global thresholding.

In this study, a simple BIM algorithm was tested and the results show that it works for some types of images (the histogram consists of two main peaks). The design of the algorithm depends strongly on the type of histogram resulting from the fracture images.

For the fracture images, it is not suggested to use the thresholding algorithms based on gradient magnitude. The textured surfaces of the fractures will strongly affect the thresholding results although the background of images is rather uniform.

Generally speaking, thresholding algorithms can be classified into manual, semi-automatic and automatic thresholding. The automatic thresholding algorithms can be sub-classified into (1) those based on the grey level histograms and (2) those based on gradient magnitude histograms. In the application of fracture recognition, if the images can be binarised satisfactorily by human vision, OPT and BCV are suggested to be used for automatical thresholding. BCV was used in the analysis of our epoxy-filled fractures (see Chapter 4).

In cases where images are more complex (because the contrast is low and there is no stable background colour, for example the BIPS image case) some adaptive thresholding algorithms may also be required.

In order to more accurately binarise rock fracture images, adaptive thresholding, edge-based or region-based algorithms may be required. In recent years, many researchers have recognised that it is difficult in most applications to use one single image segmentation algorithm to segment images. A new topic is the fusion/merger of different image segmentation techniques or algorithms. To test this kind of approach, some new algorithms have been developed based on both edge- and region-based detection (Figure 3-16). The developed algorithms are useful for fracture tracing in some cases. The fusion procedure may therefore constitute a next step of development.

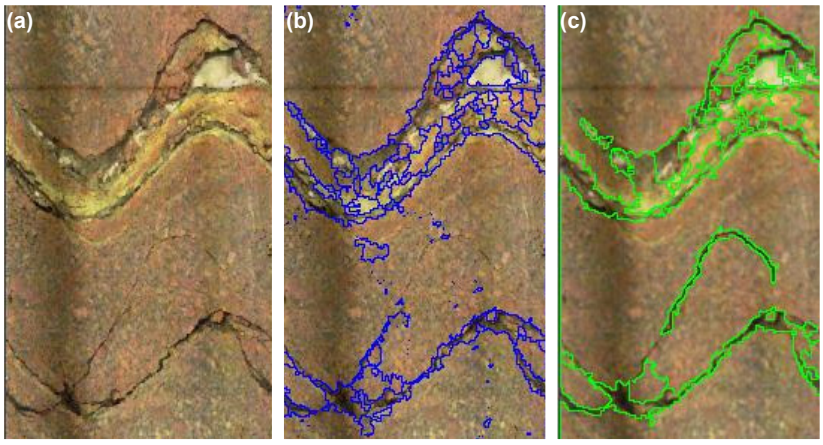

Figure 3-16. *Examples of region-based algorithms applied to fracture tracing using BIPS images: (a) Original image (b) Segmented based on image shrink similarity (c) segmented image based on smoothing and similarity. For a real segmentation application it is required to modify the segmented fracture curves, e.g. to use curve smoothing, small region merge and gap links. All these are post-processing procedures.*

3.3.2 Edge-based segmentation algorithm

Grey scale information (a colour band) is used here to trace the fracture curves. To develop the algorithm, several aspects must, generally speaking, be considered: (a) grey flatness or smoothness; (b) curvature variation; (c) magnitude strength; (d) computational searching costs; and (e) distance linking etc.

Segmentation algorithms for monochrome images are generally based on one or two basic properties of grey level values: discontinuity and similarity. For the first category, the approach is to partition an image based on abrupt changes in grey level.

On the surface of the rock, the fracture objects often appear as steep "edges" or edges of "ridges". Edges, in the image analysis literature, constitute a jump in intensity. The cross section of a so-called ideal edge has the shape of a ramp: infinite slope and flat portions on either side of the discontinuity. In smoother versions of the ideal edges, the first derivative (in an appropriate direction) attains local maxima at so-called edge points or edge pixels. A well-known *edge detector* of this type is the Canny edge detector, which locates the local maximum in gradient magnitude (= steepest slope). However, in our case we are more interested in another class of detectors, those known as *ridge detectors*. A ridge can simply be considered as a double edge (a bar edge). Between the steep parts there is a narrow plateau or peak.

Ridge (or valley) detectors are expressed as follows: a bright (dark) ridge point is defined as a point for which the intensity has a local maximum (or minimum) in the main principal curvature direction.

Ridge-based detection algorithm

The valley-edge detection algorithm reported by /Wang 2003/ may be used as a ridge detector. A valley-edge detector tries to detect the lowest valley point in a certain direction. When found, the associated pixel is used as the valley-edge candidate, and its direction and location are marked for further processing to form a valley-edge, either by thinning and tracing procedures.

As depicted in Figure 3-17 for each pixel p, check in four different directions and determine whether p is a valley-edge point or not. As an example, a small kernel valley-edge detection function runs as follows:

In the 0º direction:

If $f(x,y) < f(x-1,y)$, then $F_1^0 = f(x-1,y) - f(x,y)$,

If $f(x,y) < f(x+1,y)$, then $F_2^0 = f(x+1,y) - f(x,y)$,

If $f(x-1,y) < \alpha f(x-2,y-1) + \beta f(x-2,y) + \gamma f(x-2,y+1)$, then
$F_3^0 = \alpha f(x-2,y-1) + \beta f(x-2,y) + \gamma f(x-2,y+1) - f(x-1,y)$,

If $f(x+1,y) < \alpha f(x+2,y-1) + \beta f(x+2,y) + \gamma f(x+2,y+1)$, then
$F_4^0 = \alpha f(x+2,y-1) + \beta f(x+2,y) + \gamma f(x+2,y+1) - f(x+1,y)$;

And similar expressions in the 45º, 90º and 135º directions.

In the direction θ the following sum is calculated,

$$T_\theta = w_1 F_1^\theta + w_2 F_2^\theta + w_3 F_3^\theta + w_4 F_4^\theta$$

θ = 0º, 45º, 90º and 135º; w_i (i = 1,2,3,4) are weights.

$T_{max} = \max(T_0, T_{45}, T_{90}, T_{135})$.

If T_{max} is greater than a threshold T, the detected point will be marked as a valley-edge candidate.

The distance *L* (*L* = (i+1) – i = (j+1) – j = 1) is pre-determined based on the image resolution and quality, and smoothing is done prior to valley-edge detection.

Details on this algorithm can be found in /Wang 2003/. It is here stressed that for each direction, two values are calculated, *f1* and *f2* (= two second order differences at two scales). A weighted sum of these (in e.g. the 135 degree direction) is obtained after valley-edge detection. A post-processing subroutine must be added where three more functions are used, thinning, bridging of small gaps, and removal of short curves or lines (cf. to Figure 3-18 and Figure 3-19).

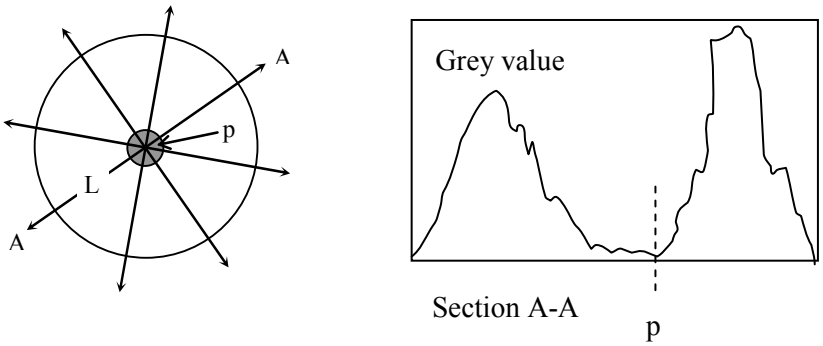

Figure 3-17. *The diagram for valley-edge detection algorithm /Wang 2003/.*

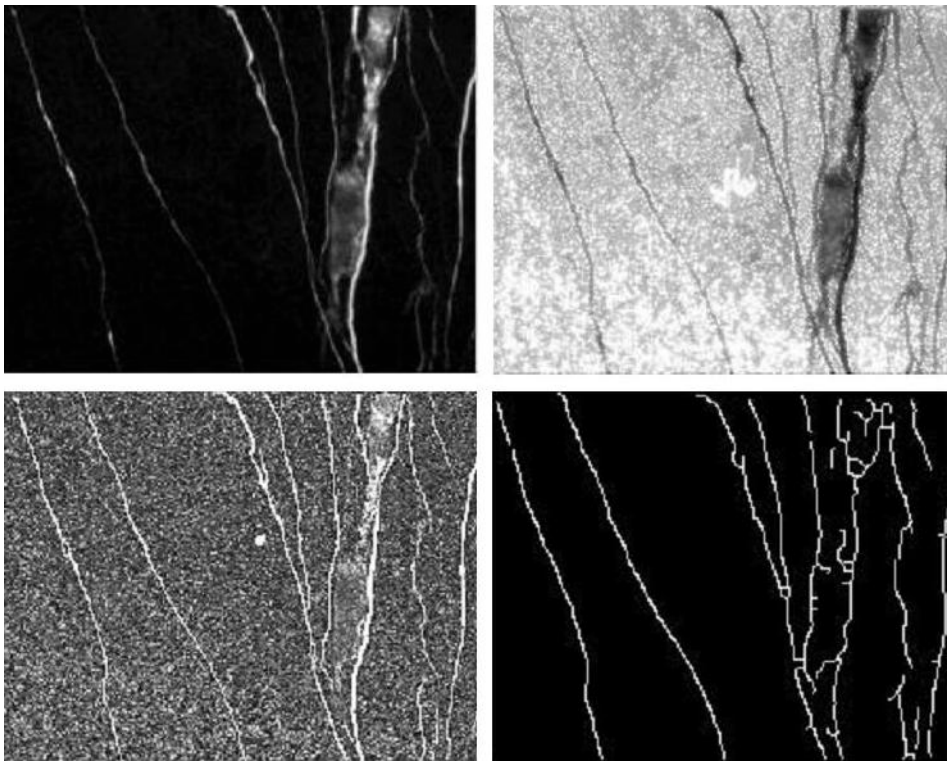

Figure 3-18. *Example 1 of the fracture tracing by the developed valley-edge algorithm. The top-left image is the original image, the top-right image is the inverted and enhanced image, the bottom-left image is a gradient magnitude image (obtained by an algorithm called Robert edge detector). The bottom-right image is the image obtained by the new valley-edged detector followed by thinning, bridging and noise removal filtering.*

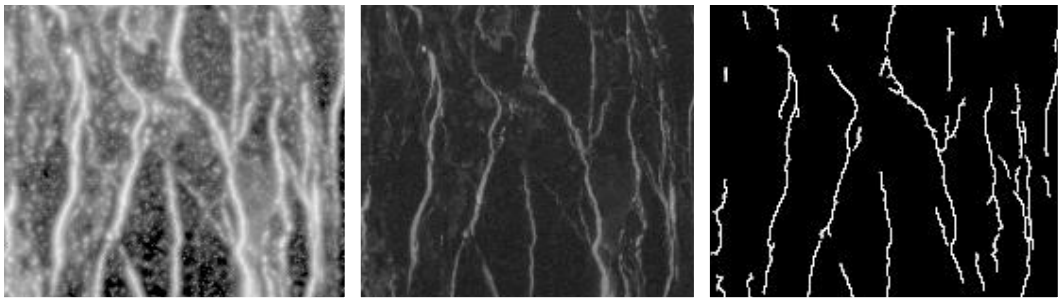

Figure 3-19. *Example 2 of the fracture tracing by the new algorithm. The left image is the original image, which is quite blurred and unclear. The image in the middle is a gradient magnitude image, and the image to the right is the resultant image.*

Handling of information at multiple scales

Multi-scale representations are more or less related to scale-space theory, notably the theories of *pyramids*, *wavelets* and *multi-grid methods*. A detailed presentation and discussion of the theory is not provided here, but detailed information can be found in /Tremblais and Augereau 2004/, /Lindeberg 1993/ and /Sergios and Stavros 2004/. For the complicated rock fracture images dealt with in this study, this methodology was proven very useful.

If most fractures in the image are very thin, the fine-detail information in the image is very important for fracture tracing, and the algorithm must avoid destroying this information. On the contrary, if fractures are thick, it is necessary to remove detailed information in the image, because it may produce a lot "fracture traces" that are actually not real fractures but created by background noise in the image. In general, one applicable image-processing tool is to use a multiple scale technique that makes image structures at coarse scales correspond to simplifications of corresponding structures at fine scales.

By using the knowledge at multiple scales, the valley edge detection results from different scale images may be combined, ending up with a promising fracture tracing result, which is difficult to obtain using other methods. A grey scale fracture image of 734×596 pixels is presented in Figure 3-20(a), and its fracture tracing result is shown in Figure 3-20(b). In Figure 3-20(a), edges (i.e. intensity contrasts) are caused both by the mineral colours of the intact rock and by fractures. These edges are randomly distributed on the whole surface of the image and the thick fracture therefore cannot be detected properly by using valley edge detection alone. The fracture mapping result is processed based on a combination of multiple scales techniques and the developed valley edge detection methods. In the following a brief description is given on how to use the multiple resolution technique.

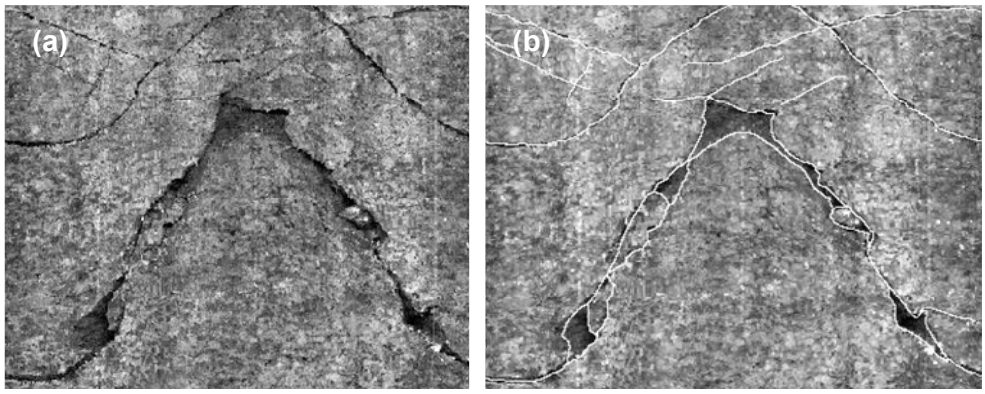

Figure 3-20. *An example of rock fracture images: (a) Original image of resolution 734×596 pixels; and (b) Fracture tracing result.*

The image scale is reduced. Let $x = 1,...,n$, $y = 1,...,m$, and $f(x, y)$ is the original image. Then

$f(x_k, y_k)$, $x_k = 1,...,n/2^k$, $y_k = 1,...,m/2^k$, k = 1, 2, 3, 4,…

where, $k \le K$, $m \ge 2^K$, $n \ge 2^K$

To obtain a useful scaled $f(x_k, y_k)$, several image shrink methods have been tried out (e.g. Gaussian, average, medium, adaptive, maximum and minimum filters). Figure 3-21 shows examples of the differences between the rock fracture images where shrink methods have been applied. With a *maximum filter* (Figure 3-21(a)) is meant that one takes four nearby pixels in the original image and out of these only uses the pixel with the highest intensity for the new shrinked image. With a *minimum filter* (Figure 3-21(e)) one instead uses the pixel with the lowest intensity.

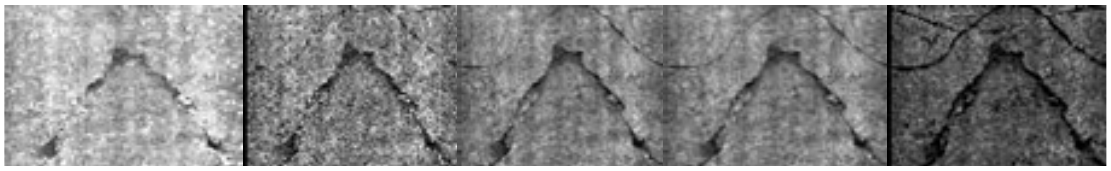

(a) (b) (c) (d) (e)

Figure 3-21. *Five different filters were tried three times shrinking the image in Figure 3-20(a): (a) Maximum filter; (b) Odd lines; (c) Average filter; (d) Middle filter; and (e) Minimum filter.*

The fractures in the original image in Figure 3-20(a) have low grey values. This causes the shrinked image using maximum filter to loose the information about thin fractures (Figure 3-21(a)). On the contrary, using the minimum filter (Figure 3-21(e)) gives an image that has sharper fractures, but the noise becomes sharp too in this image. In our case, it was decided to use the minimum filter to shrink the original image three times and then to smoothen the scaled image using a Gaussian filter (see Section 3.3.1).

The results are shown in Figure 3-22. The original image has a rough surface with thick fractures. If the developed ridge detection and fracture tracing algorithms had been directly used without image scale operations, the detection result would have included a lot of lines not representing fractures (i.e. lines). When the original image was shrunk one step, the detection result will improve. The best detection result is seen in Figure 3-22(d), where the image has been shrunk three times before the ridge detection and fracture tracing were performed.

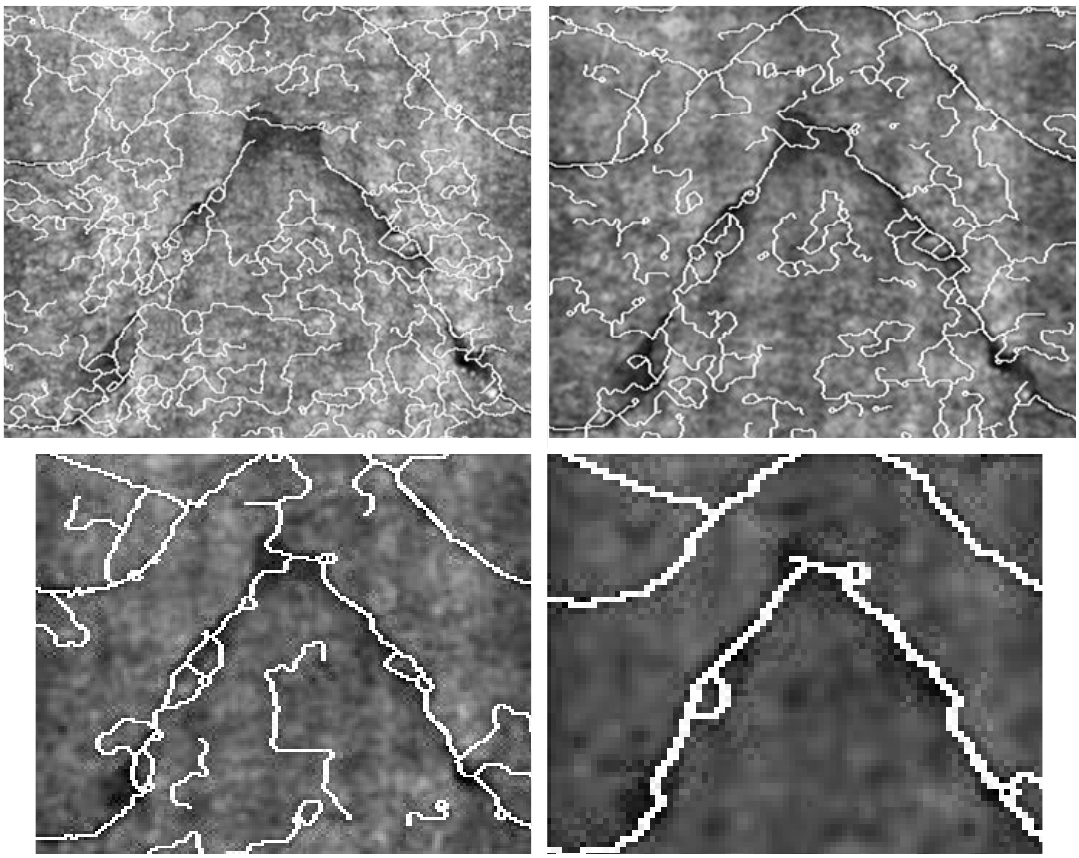

Figure 3-22. *Valley edge detection results (image resolutions in pixels): (a) 734×596, (b) 367×298, (c) 183×149 and (d) 91×74.*

In order to trace the fractures, the gaps between valley edges need top be linked together. This task requires the extraction of information about attributes of endpoints, in particular orientation and neighbourhood relationships. As usual, after image enhancement and valley-edge detection for each resolution image, the valley edges are thinned into a width of one pixel. At this stage some gaps in the valley edges prevail and noise is still present in the image. To close the gaps, it is necessary to trace the valley edges. To do this, the new algorithm first detects significant endpoints of curves (or lines). Then, it estimates the directions for each endpoint based on local directions of valley-edge pixels. Finally, it traces fractures according to the information of directions of each new detected pixel (new endpoint) and an intensity cost function. The valley-edge tracing starts from the detected endpoints to see which neighbourhood has the highest grey value, and when a new pixel is found as a valley-edge point, it is used as new endpoint. If the end point cannot be found, the various threshold values are changed until a new end point is determined.

Before it starts to trace from another detected endpoint, the tracing procedure continues until a fracture is fully traced. When there is no detected endpoint for continuous tracing, the valley-edge tracing procedure stops. For each resolution image, special tracing thresholds have been set up. The basic idea of image segmentation is to use multiple scale concepts to find maximum information about each fracture and to trace the boundaries of the fractures.

Conclusions on image processing and suggestions for further work

1. For this study, a number of algorithms have been developed (and compiled from the literature) for rock fracture image processing and segmentation.

2. A number of image pre-processing algorithms have been discussed and compared.

3. Several auto-thresholding algorithms have been studied and compared, and the BCV or OPT algorithms are considered satisfactory for the rock fracture images analysed in this study.

4. Apart from the thresholding algorithms, a region-based segmentation algorithm is also tested on BIPS images.

5. The developed edge detection algorithms are robust for ridge edge detection and fracture tracing. They have been tested for the images of epoxy-filled single fractures and fracture networks. They seem promising but may need further testing.

6. For difficult images (where cracks and fractures are difficult to distinguish due to either dark minerals or shadows etc) or images with "large" fracture apertures, use of multi-scale technology can alleviate the production of images with fractures without artificial "fractures" being introduced by background patterns.

7. A further development of the current work would be to create an automatic pre-processing procedure applicable to all rock fracture images at first. Then, to modify the developed thresholding, region-based and edge-based, image segmentation algorithms fitting them to the rock fracture images, respectively.

8. Another possibility for development would be to use neural networks, fuzzy logic, wavelet /Kokare et al. 2004/, /Muñoz et al. 2003/, /Egmont-Petersen and de Ridder 2002/ and /Jain et al. 2000/ and artificial intelligence technologies to automatically classify images. Then to use pyramid methods to divide original images into several scale levels, and use fusion/merger of the different detection algorithms to set up the appropriate fracture image segmentation and fracture detection procedures. This development would be of interest if a large number of fracture images, including such with large differences in character, were to be analysed.

4 Fracture network analysis

When the fractures or pores (i.e. the epoxy filled areas in this case) are separated out by use of the colour or grey scale images, the question is how to classify or characterise the binary (black and white) fracture patterns obtained. A need exists for a set of parameters that describes (or reflects) different properties of the network that are being subject to analysis, such as:

- The amount of fractures.
- The location and orientation of fractures.
- The apertures of fractures.
- The shape of fractures.
- Existence and size of rock fragments made up by the fracture network.
- The connectivity between the fractures.

Even if one of the above parameters is similar for two different fractured zones (for example the number of fractures), still the flow and transport properties of the zones could be distinctly different. Therefore, a certain number of parameters must be considered and combined to constitute the base for the characterization.

To exemplify, there are four different "types" of character of fractures or fracture zones as outlined in Figure 4-1. The case *(a)* is the simplest "single fracture" case. This type of fracture has previously been studied with different techniques and the main parameter that has been used is the aperture, where the aperture is the point-wise distance between the two opposing fracture surfaces (with the aperture being measured in the direction perpendicular to the overall facture plane). This parameter is sufficient, and not difficult to apply, at least as long as the two side walls are fairly sub-parallel and planar. Another parameter often used in this situation is the point-wise height coordinate for the fracture surface (again in relation to some reference plane normally being parallel to the overall fracture plane). The variation of this parameter gives information on the roughness properties of the fracture surfaces. (Note that measurement on one of the fracture surfaces does not give any information on aperture and that the roughness parameter in itself does *not* reflect the aperture or aperture variation).

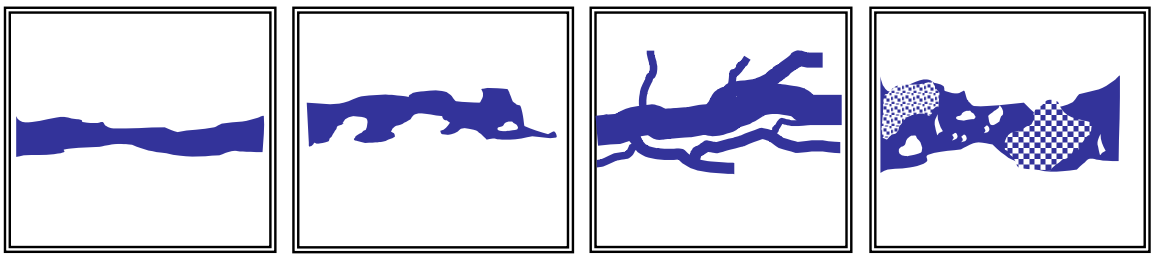

Figure 4-1. *Different general characters of fracture or fracture zones (a) single fracture, (b) complex single fracture, (c) Branching fractured zone and (d) Porous fractured zone.*

In the case *(b)* the situation is similar, with only one single fracture, but in this case there is a more complex situation due to fracture filling material of different kinds. In this case it may be more difficult to measure the aperture and there are few examples found in the literature. For obvious reasons it has been more difficult to sample and measure theses surfaces, where the infilling or fault gouge is often softer or looser and probably highly sensitive to drilling and cutting processes, drying etc. The aperture parameter, as such, is also more difficult to define for this situation since there is no obvious direction for the aperture to be measured and "multiple apertures" may well appear, due to enclosed infilling fragments within the single fracture.

The third case *(c)* is a case where the fracture pattern is so complex and there are so many fractures that it is not meaningful to talk about a single fracture, but rather a "fractured zone". This fractured zone consists of several shorter fractures, which are connected to each other. If water flows through such a fractured zone it is clear that the rock surfaces (and rock matrix) that are in contact with the flowing water is much larger compared to the single fracture case, and hence the summed-up area available for matrix diffusion and/or sorption becomes larger, even if the transmissivity may still be similar. This type case may be called the "branching fractured zone".

The forth case, *(d)*, is the case where there is a lot of fine-grained material in the fracture zone. This material may be located on the fracture surfaces, consisting of porous infilling minerals, or it could be fault gouge material that is clogged between opposing rock surfaces. Also, there may be larger mineral grains and fragments of the wall rock enclosed by the fracture pore space. In this case it is hard to talk about branches of fractures. The multitude of small pores of water may well be important for the transport properties but it is not meaningful to describe these pores using the conventional aperture parameter. If the infilling, or fault gouge, material is substantial it could fully block (or diverge) the flow in the zone or reduce the transmissivity of the zone significantly. This case is denoted the "porous fractured zone". It is reasonable to expect that the retention properties in the case *(c)* could be quite different compared to case *(d)*, due to both geometry and mineralogical differences, also in cases when the overall hydraulic conductivity is similar.

In this study the focus is on the fault rock, i.e. the rock at deformation zones, and smaller scale fractured zones, where clear displacements have taken place. In the following, the possibility to describe this type of zone quantitatively is discussed. The sample collected from borehole KA2423A03 shows both branching and porous character, something in between cases *(c)* and *(d)*. Attempts have been made to find quantitative parameters that could be used to describe this zone, such that it would be possible to distinguish this zone from another zone with slightly different properties. This chapter presents the parameters in general and then Chapter 5 discusses the influence of scale (i.e. image resolution) followed by the specific results for our samples as presented in Chapter 6. Examples of how image analysis may be applied to analysis of single fractures are provided in Chapter 7.

4.1 Basic binary image parameters

Figure 4-2 introduces two example images I and II that may be considered as two different fractured zones. After the fracture image processing described in Chapter 3 the result has become like the two binary images seen in the figure. Notable is that the fractured zones indeed have clear similarities, but also show clear differences. These example images are in the following explored to further explain and exemplify different image analysis parameters investigated.

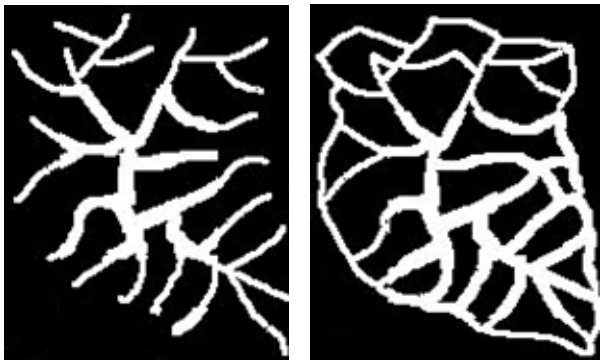

Figure 4-2. *Example images I and II.*

The image consists of a certain number of pixels and they are either white or black. Often it is of interest to calculate the proportion of white pixels, if the object is white the background colour is black (if needed the image can always be inverted) For example, in images I and II in Figure 4-2, the proportion of white area is 20% and 29%, respectively.

In our sample case, if the epoxy is considered representations of the pores, and the whole image frame is the study area, the proportion of white in the image being the same as the porosity of the area. There are, however, some problems in applying this simple porosity parameter estimate as will be discussed further.

Another basic parameter of the whole image is that the number of objects in the image may be calculated. Each object constitutes a number of white pixels that are connected to each other. The object may have any shape and size. When the picture is very complex the type of object varies a lot. In our two example images in Figure 4-2 there is only one object in each, because all the white pixels are connected.

There are two general approaches to carry out the further analysis of the binary pattern. Either the pattern is regarded as a collection of fractures or as a collection of particles. With a “fracture” is here implied that the objects are basically lines or non-closed curved lines and with a “particle” is here implied an object that is formed by a closed curve. Using both approaches there are ways to define parameters that fulfil one or more of the desired needs listed at the beginning of this chapter. Both approaches were applied to our example images.

4.2 Fracture network parameters

Considering the pattern as a number of connected branches of fractures, one parameter that describes the level of complexity is the number of fracture junctions. This entity can be calculated by first making all fractures thin, only one pixel thick. By doing so, the images in Figure 4-3 are obtained, and this pattern is denoted the "skeleton" or the "net image" of the fracture network.

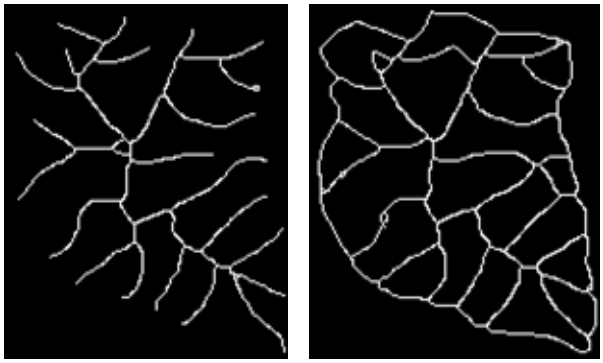

Figure 4-3. *The skeleton (net) image of example I and II in Figure 4-2.*

Another developed algorithm is used on the net image to find the points where the fractures are branching and these points are marked. The result is seen in Figure 4-4. If one then takes the net image and deletes the junction points from the net, the remaining image consists of separate branches. This image does not have only one object anymore, but many, see Figure 4-5. The number and statistical properties of this collection of branches may also be used as a descriptor of the fracture network. In Table 4-1 some results are given from this type of analysis applied to our two example images. The number of junctions and branches of course increases in example II because it has more fractures. But the difference in ratio between the two parameters gives some hint on the difference in connectivity between the two networks. The number of junctions becomes relatively low in the case with many "dead-end" fractures, like in example I. This difference is even more clearly seen if the number of end-points of the net is calculated (also given in Table 4-1). In network II there are no end-points at all while there are many in example I.

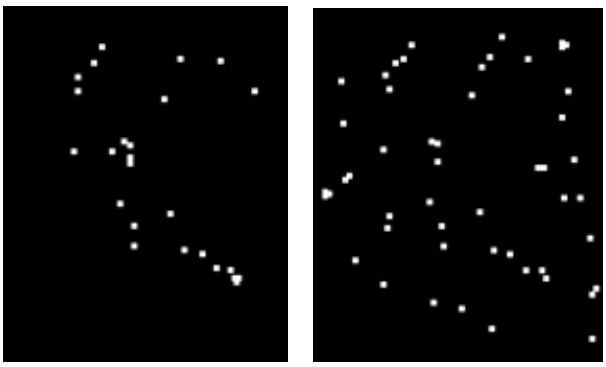

Figure 4-4. *The junctions of the nets in example I and II in Figure 4-3 (the points are enlarged for visibility).*

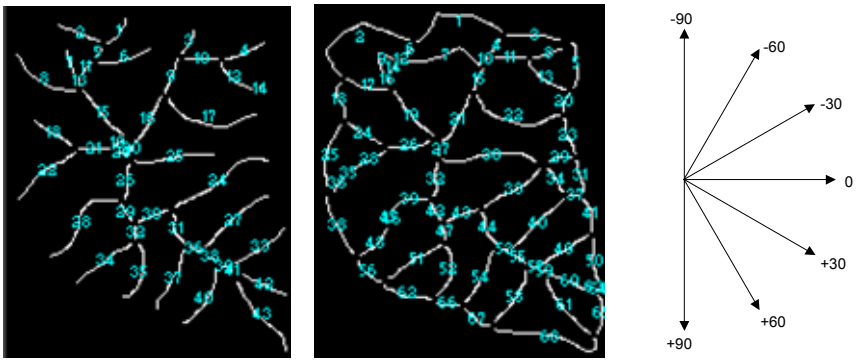

Figure 4-5. *The "branch" images of the networks I and II in Figure 4-3. Every object (branch) in the image is given an object ID-number. For every object the size and overall orientation is determined, counted as positive angle clock-wise from the x-axis.*

Table 4-1. Fracture network parameters based on the net (skeleton) image.

Example	Number of junctions	Number of branches	Ratio between branches and junctions	Number of end-points	Average size (length) of branches [pixels]
I	26	43	1.65	39	22
II	51	68	1.33	0	21

A frequency histogram of the branch orientation may reveal if there is any preferred orientation of the fractures in the network. In our simple example I it is readily seen from the histogram (Figure 4-6) that there are five more preferred orientations (around -60, -35, -5, 25 and 85 degrees, cf. Figure 4-5), but our sample is small and there exists no strongly dominating direction.

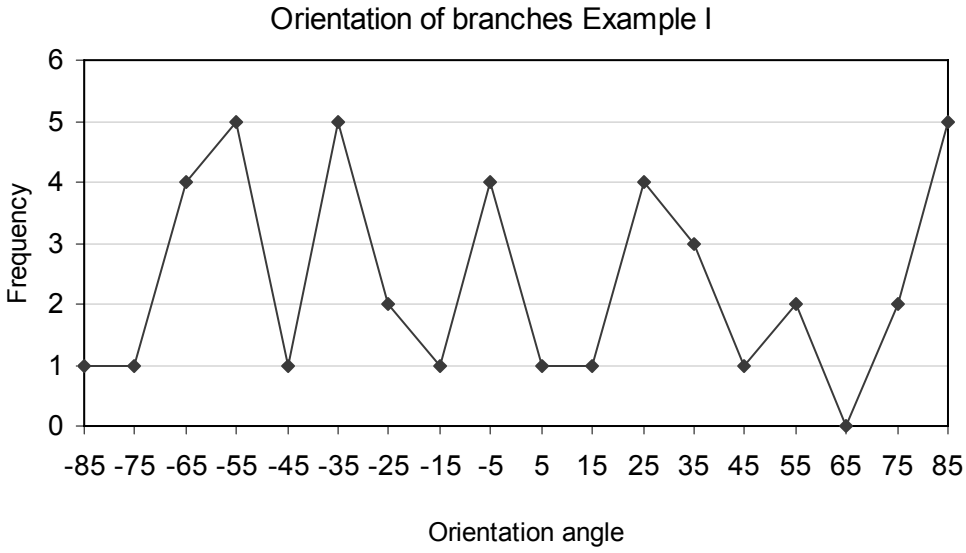

Figure 4-6. *Frequency histogram for the orientations of the branches of Example I network.*

4.3 Fracture particle parameters

The other approach to analyse the network is to consider it as being made up of particles surrounded by a background. To find these objects the original boundary image is first inverted, then the boundaries between the black (pores/fractures) and white (rock) in the image are traced and these boundaries will, in the case where there exists particles, form closed curves. In our Example I, only one very small particle is formed (the large background white area in is not counted as a particle). This single small particle does not give much information about the fracture network. Therefore, the particle approach is not so useful for the fracture networks with extreme branching character and poor connectivity, but of course the analysis tells us that this is the case and this is good information as such. A small number of particles implies a low connectivity between fractures, or it means that the complexity is very low in general, such as in a single fracture case.

On the contrary, all rock parts (white parts) inside the network in image II are enclosed by connected lines and therefore make up particles (these could be called rock blocks, rock fragments or mineral grains depending on what material and scale being studied, but in the following the term particle has been chosen).

Figure 4-7 shows the result after using the particle tracing algorithms on Example II. Each particle is now an object with a given ID-number. As with the branches, the statistical properties of this collection of particles are another way of describing the character of the network.

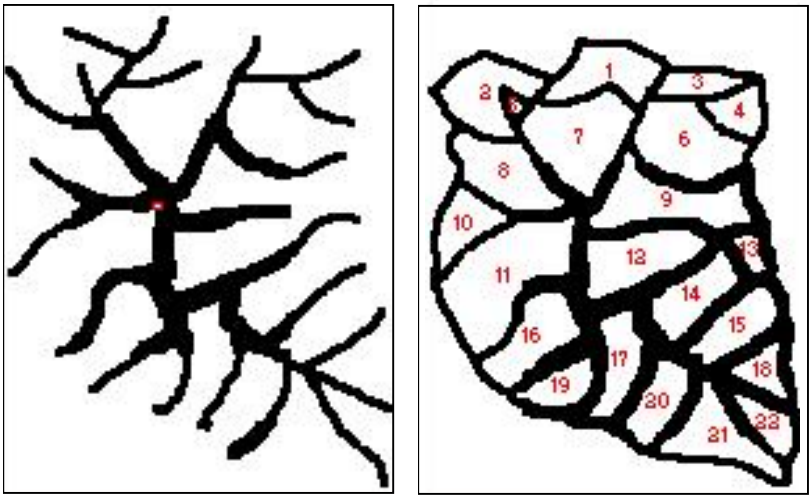

Figure 4-7. *Particle images for two example networks. In Example I (left) only one small particle is found whereas that of Example II shows 22 particles (right).*

The particle area is the main property of interest, but the shape of the particles may also be important for describing the character of the network. Anisotropy in the network, such as a higher frequency in the number of fractures in a given orientation would show up as a preferred elongated shape of the particles. When the shape properties of particles are studied, the very small objects, with areas less than 10 pixels, are disregarded since the shape of them are regarded as being essentially meaningless.

To study the shape of the particles, equivalent simplified geometries like ellipses or rectangles are often used, here exemplified with an ellipse. For each particle, one ellipse is determined which has the same centre of gravity and first and second moments around the axes as the particle. The length of the particle can be measured as the length of the major axis of the equivalent ellipse. The ratio between length and width of the equivalent ellipse may be used as a measure of shape. In our example the average elongation of the ellipse (length of major axis divided by the length of the minor axis), is 2.1. In Table 4-2 some example parameters are determined for the two example images in Figure 4-7.

Table 4-2. Fracture network particle parameters for example networks (see Figure 4-7).

Parameter	Example I	Example II
Number of particles	1	22
Average size [pixels]	2	500
Median size [pixels]	2	463
Maximum size [pixels]	2	1330
Minimum size [pixels]	2	17
Standard deviation of size [pixels]	-	312
Number, N, of particles of size > 10 pixels	0	22
Average ellipse length of N [pixels]	-	37
Average ellipse width of N [pixels]	-	18
Average elongation of ellipse [pixels]	-	2.1

The histogram in Figure 4-8 shows the overall orientation of the particles. The orientation is calculated as the direction of the equivalent ellipse major axis direction. The preferential orientation of the particles in Example II is between -40 to -50 degrees. Notable is that this indicated direction is roughly similar to the preferred direction obtained by studying the branches of the similar network given by Example I, cf. Figure 4-6. Since branches are surrounding the particles this should normally be the case.

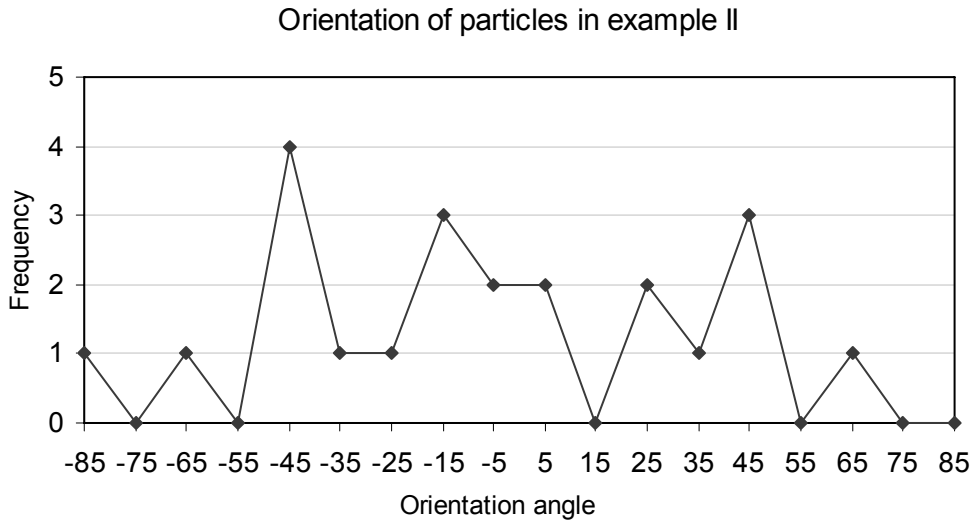

Figure 4-8. *Frequency histogram for the particles orientation in Example II (see Figure 4-7).*

5 Influence of image resolution on determination of porosity

To study the influence of scale (image resolution) on the results, image analysis was conducted on images taken at two different distances from the sample surface. Figure 5-1 shows an image that covers the whole rock surface of the specimen. The red square is the studied part, which is also shown in Figure 5-2. To sample different porosity areas of the image, the study area was divided into eight frames. In frame 4 and 8, the porosity is high, while in frame 2 the porosity is low.

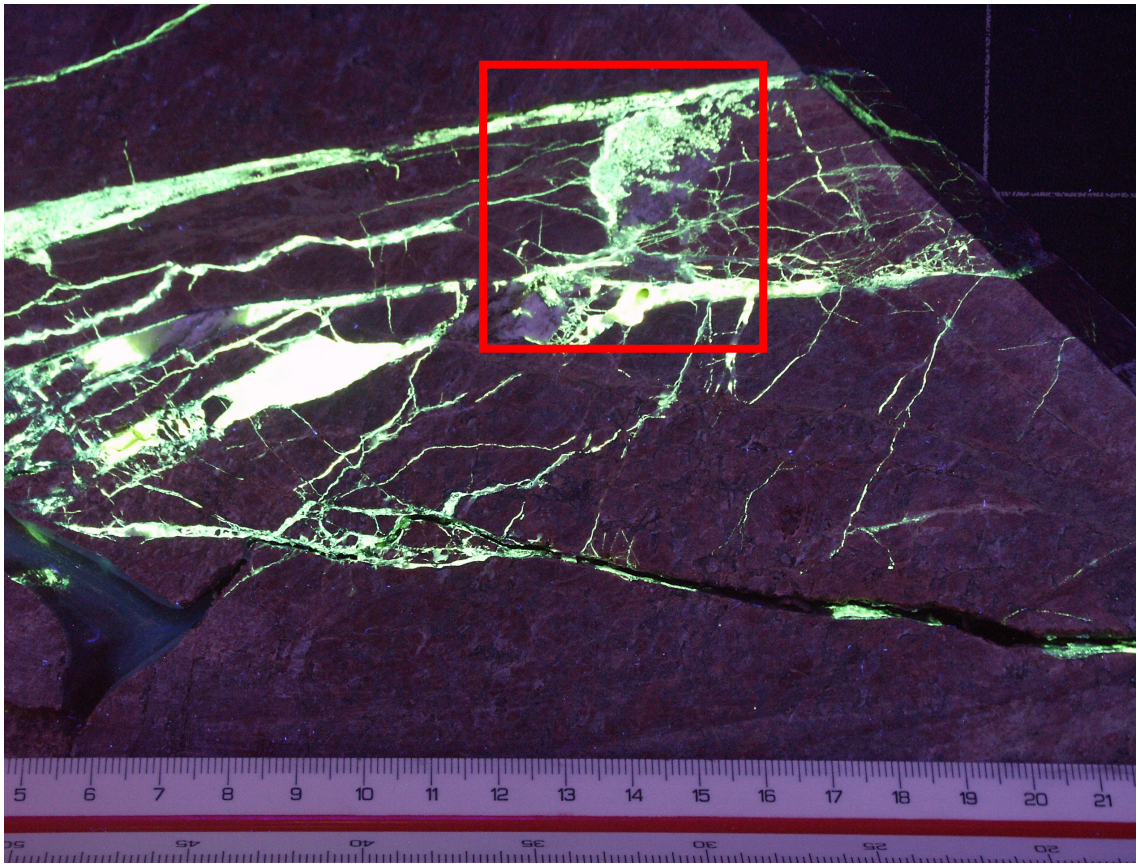

Figure 5-1. *B2 slice a4. Original UV image with the lower resolution used for the study of resolution influence. A part of this image, the marked area, was selected for the study, see Figure 5-2.*

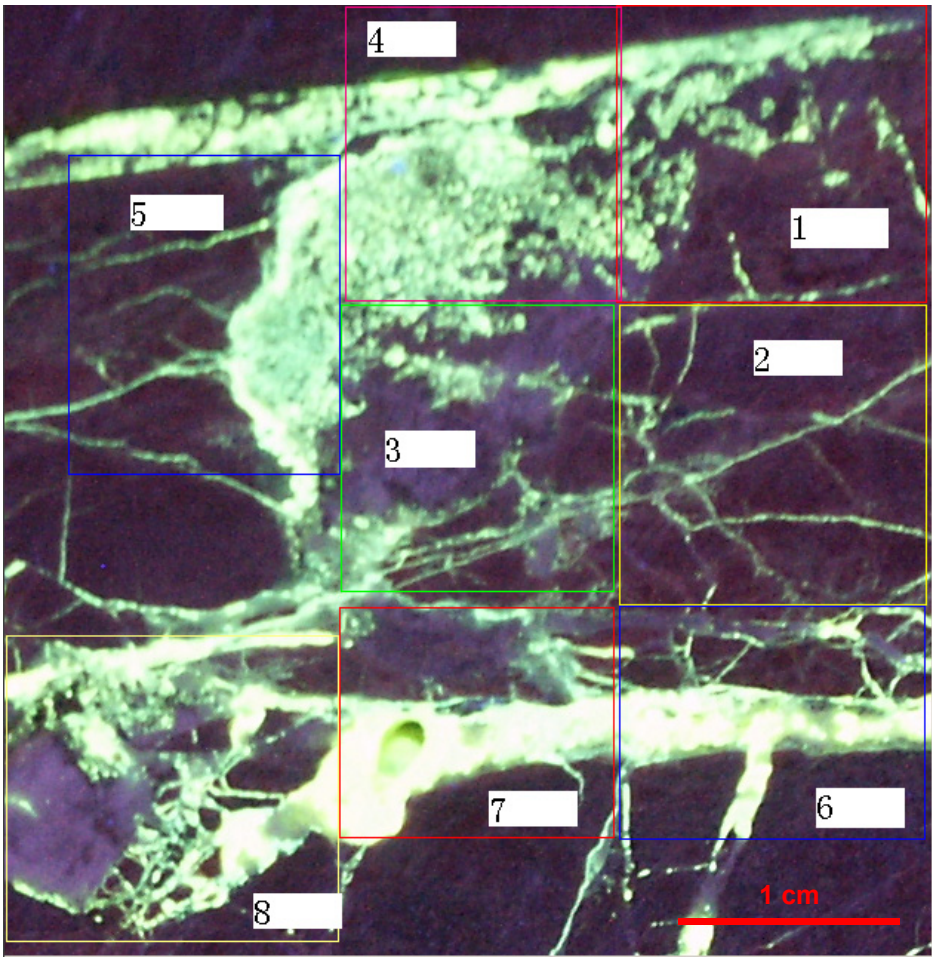

Figure 5-2. *B2 slice a4. Eight sub-frames were selected from the study area and from each frame a new image was taken with a shorter camera focus distance. The image shown here has the relatively lower resolution (0.066 mm/pixel).*

As a global processing procedure, the BCV operation was used, as described in Section 3.3. For the analysis, each frame was cut out as a separate image, and binarisation performed on each image separately.

For each frame a new image was obtained by cutting out parts from an image with a shorter camera focal distance. As an example, the image in Figure 5-3 is frame 2. The resolution of this image is 0.021 mm/pixel (image size 672×652 pixels). The resolution of the image is thus increased by approximately three times compared to the lower resolution. If Figure 5-3 is compared with frame 2 in Figure 5-2 it can be noted that since resin areas are thin, some of them cannot be seen in the lower resolution image. Some conspicuous differences are marked by coloured circles in Figure 5-4, which shows the resulting binary image for both resolutions.

When the frame includes some large epoxy parts, there are some relatively large differences depending on the image resolution. For example, in frame number 8 (see Figure 5-5) the image includes distinct and large epoxy resin areas, but in this case also some of the non-epoxy filled areas might be detected as epoxy filled. This effect appears because, when the camera and lamps are close to the specimen, large and strongly fluorescent epoxy areas reflect the UV light too much, and bright and transparent minerals like calcite may be inadvertently recognized as epoxy.

The porosities, here defined as the percentage of white areas in the image frame, and the number of particles are determined for both resolutions.

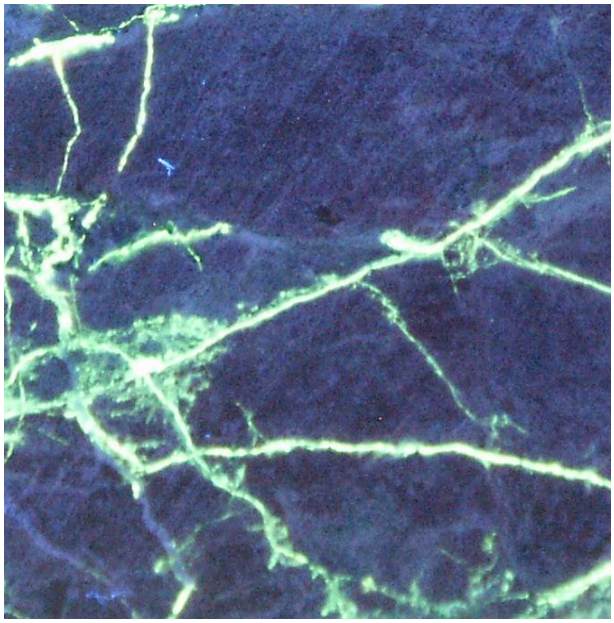

Figure 5-3. *Frame No.2 UV image with the higher resolution, 0.021 mm/pixel.*

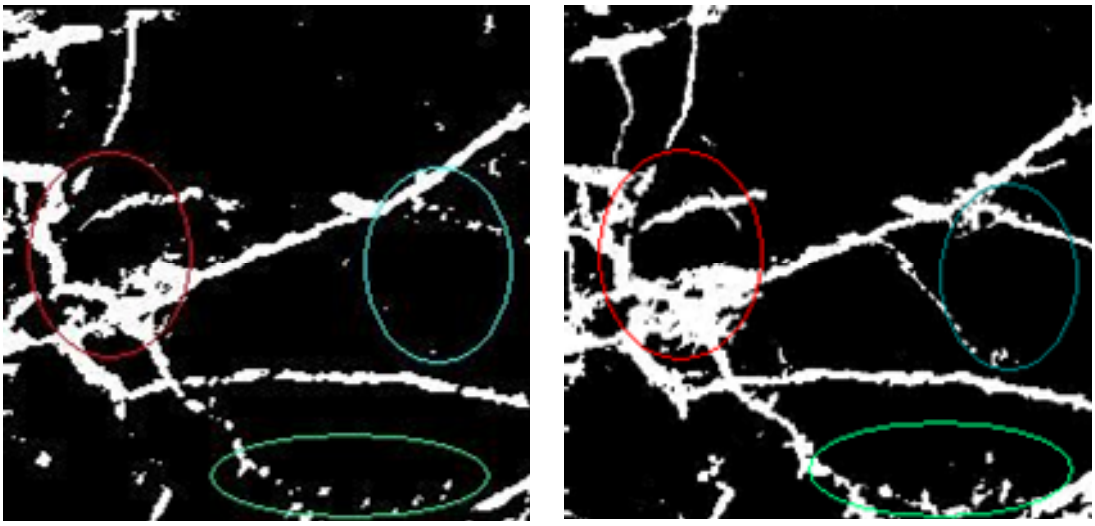

Figure 5-4. *The binary images from frame 2 with different focal distances (resolutions); the one to the left is the low-resolution image, and the one to the right is (a shrinked) image of the high-resolution result. Some locations where differences are noticeable are marked by coloured circles; cf. Figure 5-3 for original image.*

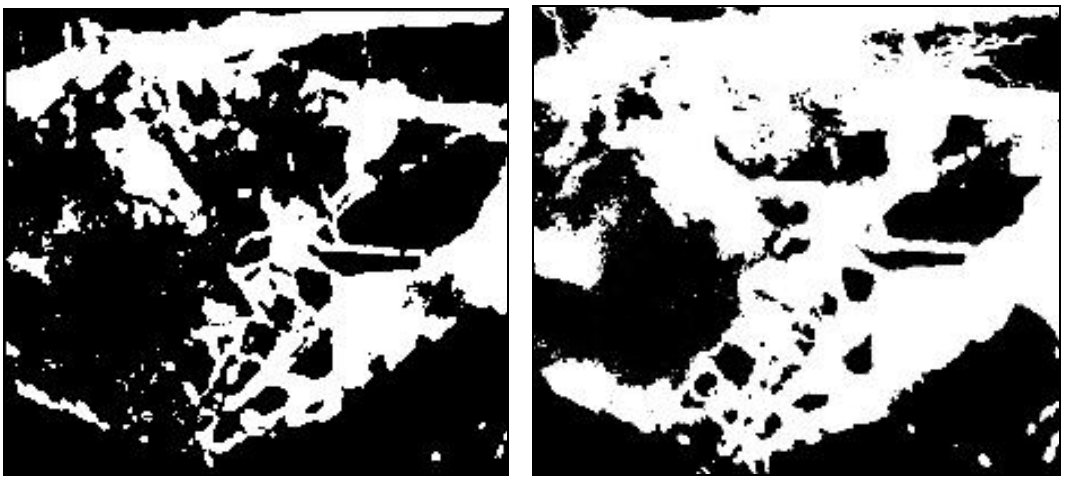

Figure 5-5. *Comparison between two binary images (frame 8), low-resolution image is the one to the left and the high-resolution (here shrinked) image is to the right.*

The parameter values in Table 5–1 show that there is a fairly large difference between the two different resolution images. The interpreted porosity (i.e. the percentage of the frame detected as being filled with epoxy) increases as camera focus distance decreases. When the resolution is increased by three times (0.066/0.021 = 3.14), the porosity increases by 2-23 %-units. On average, the porosity increases 10 %-units.

Since the image detection area is 9 times smaller in the high resolution case, a lot of small resin areas (which cannot be detected in the low-resolution image) show up. Therefore, as expected, the number of particles on the image also increases greatly with increased resolution.

Table 5-1. Results from comparison of porosity (epoxy resin filled areas) in images using different resolution.

Frame	Porosity Low – resolution [%]	Porosity High-resolution [%]	Difference [% -units]	Number of particles, Low-resolution	Number of particles, High-resolution
1	26.0	28.1	2.1	8	166
2	11.4	14.7	3.3	15	120
3	28.5	35.0	6.5	39	189
4	61.3	71.5	10.2	48	761
5	32.1	39.7	7.6	14	104
6	34.5	45.0	10.5	17	56
7	38.6	55.3	16.7	13	47
8	32.5	55.9	23.4	32	290

The above described comparison illustrates well the kind of aspects that must be considered before selecting the procedures for a detailed pore space analysis. The accuracy or resolution of the camera is a factor that is important and it should, at each study occasion, be considered what the best equipment available on the market is. As long as light requirements are not changed, a large number of pixels per frame should be preferred since it makes it possible to acquire desirable overview images of still acceptable quality for analysis.

A particular aspect for the image analysis of fractures and fracture fault zones that should not be overlooked is the very anisotropic nature to be expected. A fault is by definition the result of a deformation and therefore consists of fractures that are not evenly distributed. To determine the porosity of only a small part of the zone, for example exactly at the major opening, would be misleading. To compare porosity values from images where the amount of surrounding rock is very different is also considered not relevant. Great care must therefore be taken when presenting "porosity" parameters stemming from image analysis. Whether analysed from one single image or from a sequence of images across the fault, the characterisation should cover the whole zone, representing the full zone thickness.

6 Two dimensional fracture network analysis based on rock slices

6.1 Fracture zone slices

The sample preparation and image acquisition for the fractured zone encountered in borehole KA2423A03 (Figure 6-1) is described in Section 2.3 and 2.4.

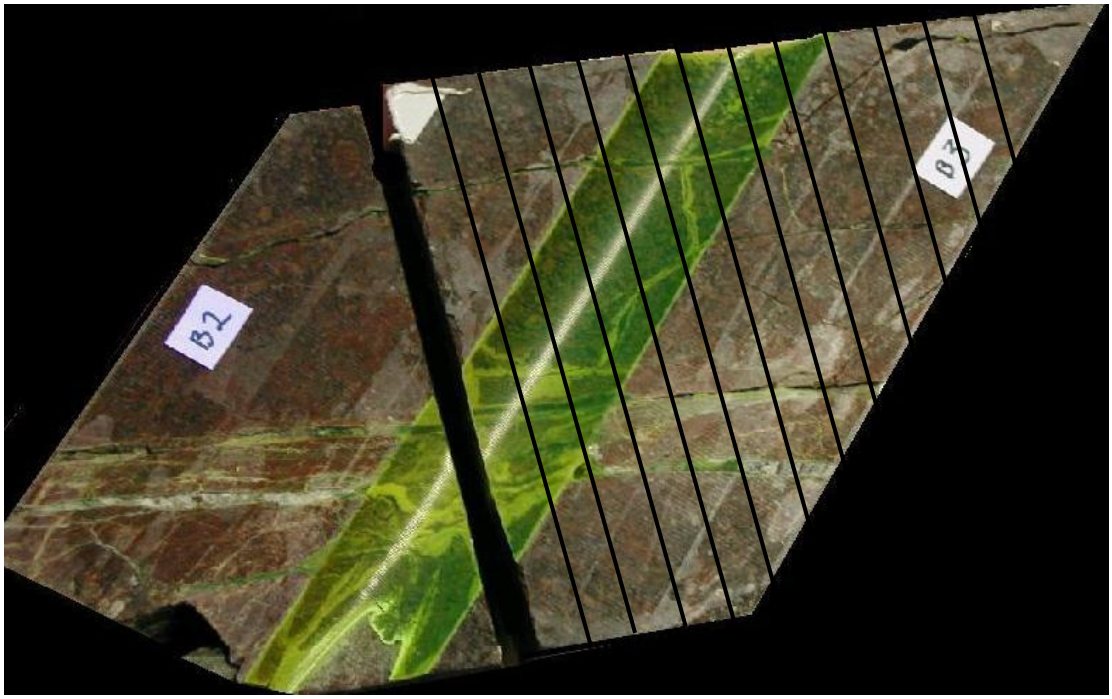

Figure 6-1. *Samples B2 and B3 were cut in two orthogonal directions. The cuts of sample B2 are parallel to the plane of the image. The thickness of a slice is about 18 mm. The B3 cut number one is the leftmost cut and the surface on the left side of this cut to is referred to as B3-a1 and the surface on the right side is B3-b1, etc. Only the a-sides of the cuts have been subjected to study.*

In Figure 6- 2(a and b), the overview images of the 12 B3 slices are shown. It may be noted that the main core of the fractured zone is covered well by the first 4 surfaces and partly by slices 5 to 8 but in the slices 9 to 12 only some of the fractures away and parallel to the fractured zone are covered. This must of course be considered when analysing the results of the image analysis.

In Figure 6-3, the 7 UV overview images of B2 sample slices are presented. The overall colour of the images may have some variation, which was caused by either slight differences in the UV lighting (or disturbances from extra lighting) or differences in the epoxy fluorescence strength on the rock surface. To fully avoid this type of variations one could construct a shielded illumination box for image acquisition such that the illumination could be kept perfectly stable. However, these minor variations are not judged to affect our results significantly and the overall quality of the images used for analysis was judged sufficient for this study, including elements of methodology development.

As described in Section 2.3, images were taken at three different scales, one for overview of the whole sample, which may be used for three-dimensional construction and analysis, and an intermediate scale used for the main fracture network analysis. These images are taken slightly closer to the sample such that only the epoxy filled fractures are covered. Finally, some more close-up images have been taken to enable more detailed studies of some parts of the fracture surfaces.

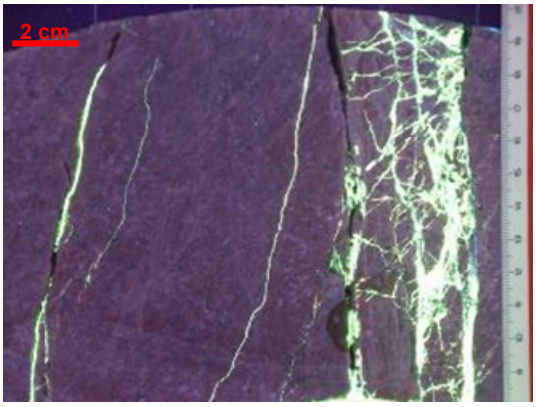

Slice B3-a1

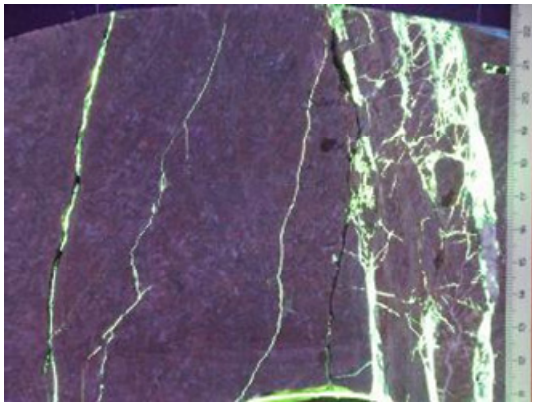

Slice B3-a2

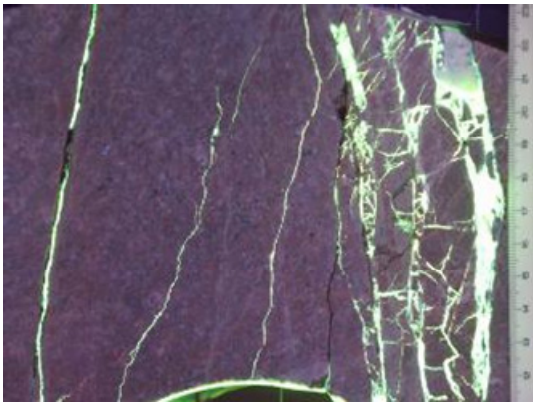

Slice B3-a3

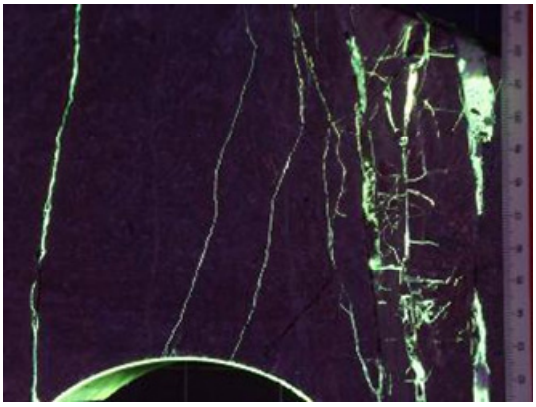

Slice B3-a4

Figure 6-2. *(a) B3-B13 slice images (first 4 on this page and the following 8 on next page) at UV illumination. These images provide the overview and shape of the whole drill core sample slices (The images that were actually used for the image analysis where not these ones but images at the intermediate scale, i.e. taken a little closer to the samples including only the epoxy network part.) In the lower part of the images one can notice the thin epoxy layer that surrounded the dummy in the pilot borehole used for the injection. Note that the intersection of the core of the fractured zone is such that only the first four slices fully cover the fractured zone. Therefore, in the following, this is considered when interpreting and comparing the results. All images could, however, be considered as a possible pattern of a fractured zone image in general, some consisting only of a few fractures and others being more complex.*

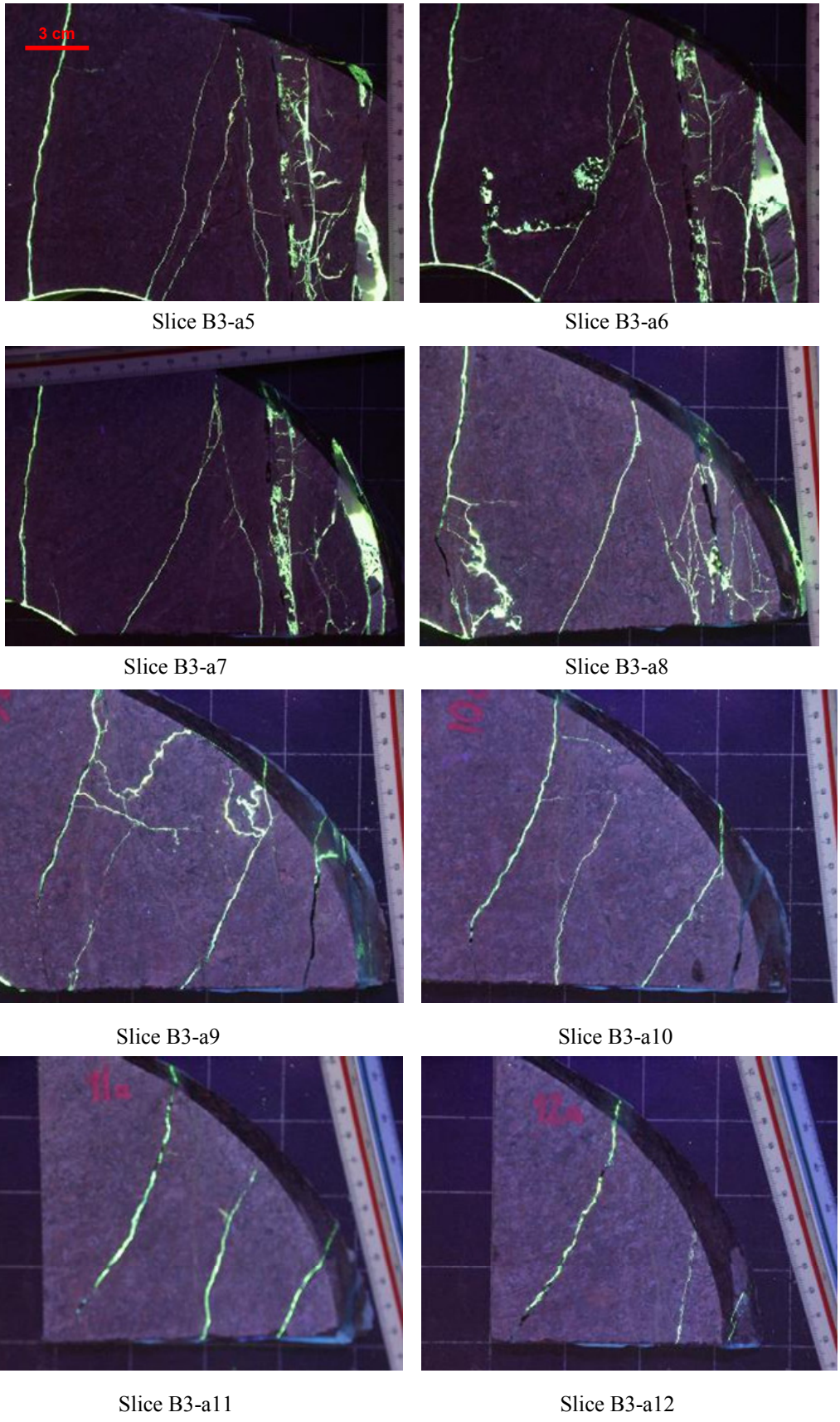

Figure 6-2. *(b) (See figure caption on preceding page).*

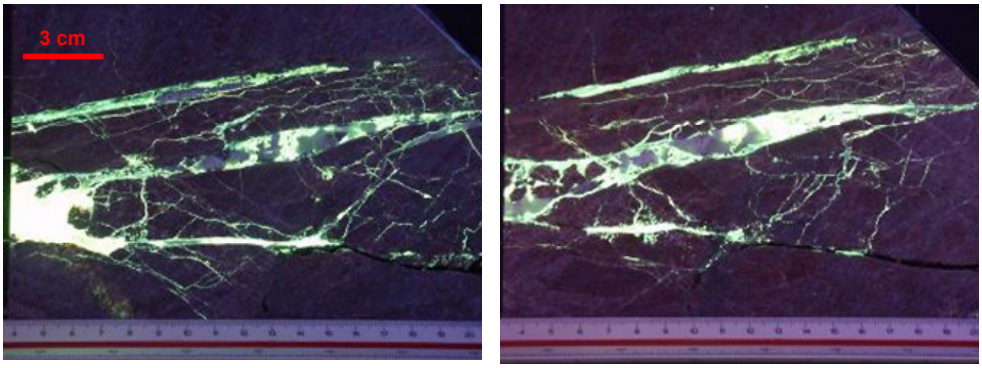

Slice B2-a1 Slice B2-a2

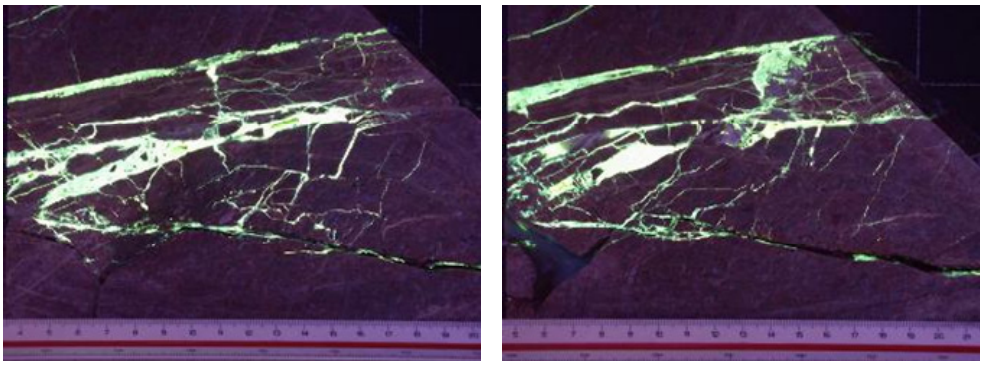

Slice B2-a3 Slice B2-a4

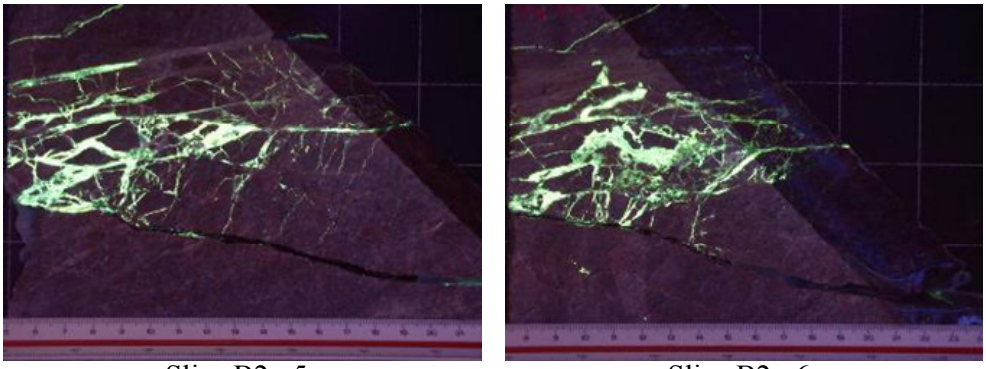

Slice B2-a5 Slice B2-a6

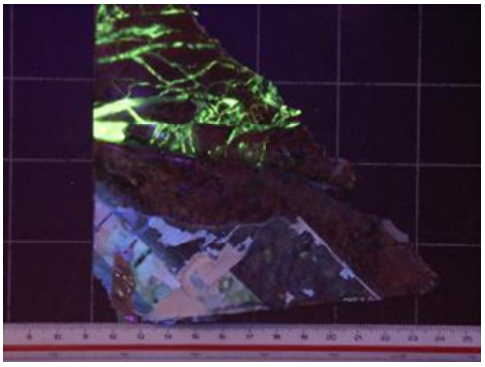

Slice B2-a7

Figure 6-3. *Sample B2, 7 slices, a-sides of cuts at UV illumination; these images provide overview and shape of the whole drill core sample slices. (The images that were actually used for the image analysis where not these ones but images at the intermediate scale, i.e. taken a little closer to the samples including only the epoxy network part.)*

6.2 Image processing of slices

For each slice image, the UV colour image is converted to a grey scale image, using the green part of the colour image. Then some image enhancement was applied followed by binarisation (cf. Chapter 3). The thresholding operation was not performed automatically; instead the threshold was selected manually. After the thresholding the image was further processed by using smoothing, dilation and thinning operations and even some manual changes in the images were introduced at some locations. This was performed with the aim of obtaining a binary image suitable for the net image, i.e. to enhance the connections along fractures and highlight the inherent structural pattern of the network. However, these operations will not produce a suitable image for displaying the structure inside the major fractured zone, since infilling material disappears in the image and the pore volume becomes exaggerated. The original binary image after thresholding should also be the optimal image for providing the most representative measure of the overall porosity. The image taken at ordinary light is sometimes useful for comparison with the UV image in cases when the content of the UV image is difficult to interpret.

As representative examples, images from B2-a1 are displayed. Figure 6-4 shows the image at ordinary lighting, and Figure 6-5 shows the corresponding image of B2-a1 at UV lighting. The fractured zone consists of three larger (or thicker) fractures which are connected by a number of smaller and thinner fractures. Inside the large fractures, some parts contain infilling minerals and some parts are epoxy-filled pores.

To the left in the image in Figure 6-4 there is a large epoxy-filled area. This is not representing the true pore space in the undisturbed fractured zone because this slice is the first slice very close to the pilot drill hole such that what is seen is the epoxy layer filling up the annular space between the dummy and the borehole wall. This fact is compensated for in the analysis of this image by reducing the white area with 400 mm^2 (estimated based on visual inspection directly on the rock samples itself).

The binary image after pure thresholding is shown in Figure 6-6 and the binary image obtained after some further processing to enhance the fracture network structure is shown in Figure 6-7.

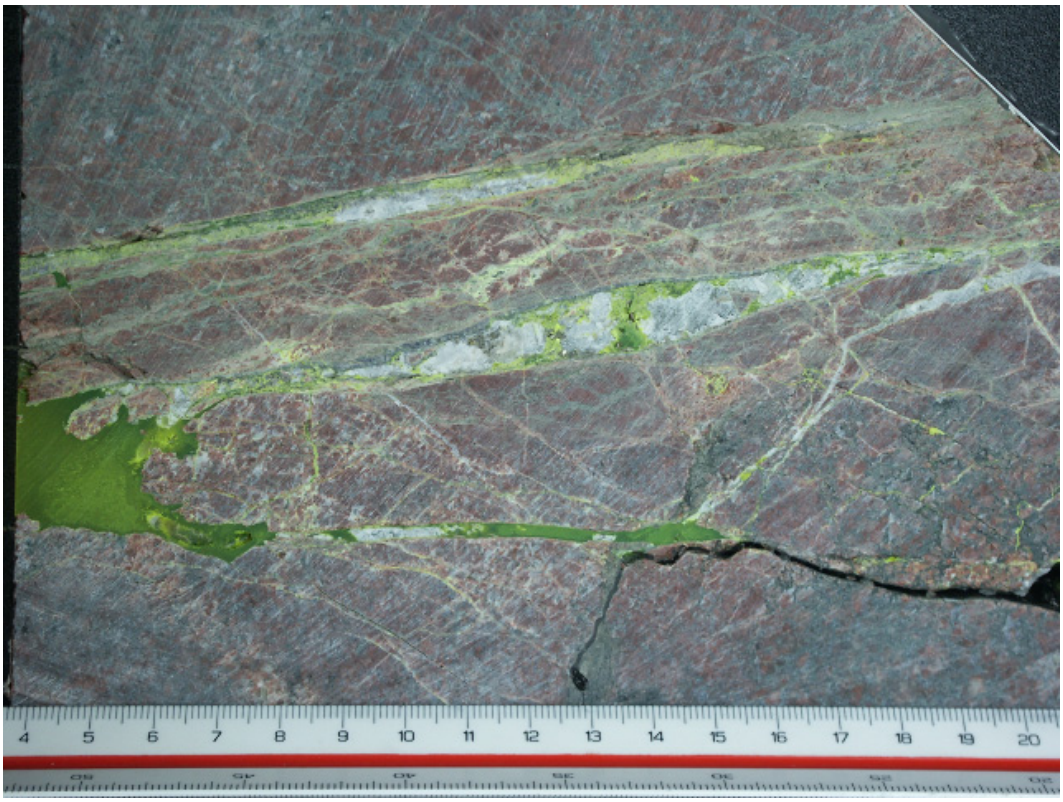

Figure 6-4. *B2-a1 image at ordinary light; the scale factor is 0.062 mm/pixel, image size 2,560×1,920 pixels = frame size 169×127 mm.*

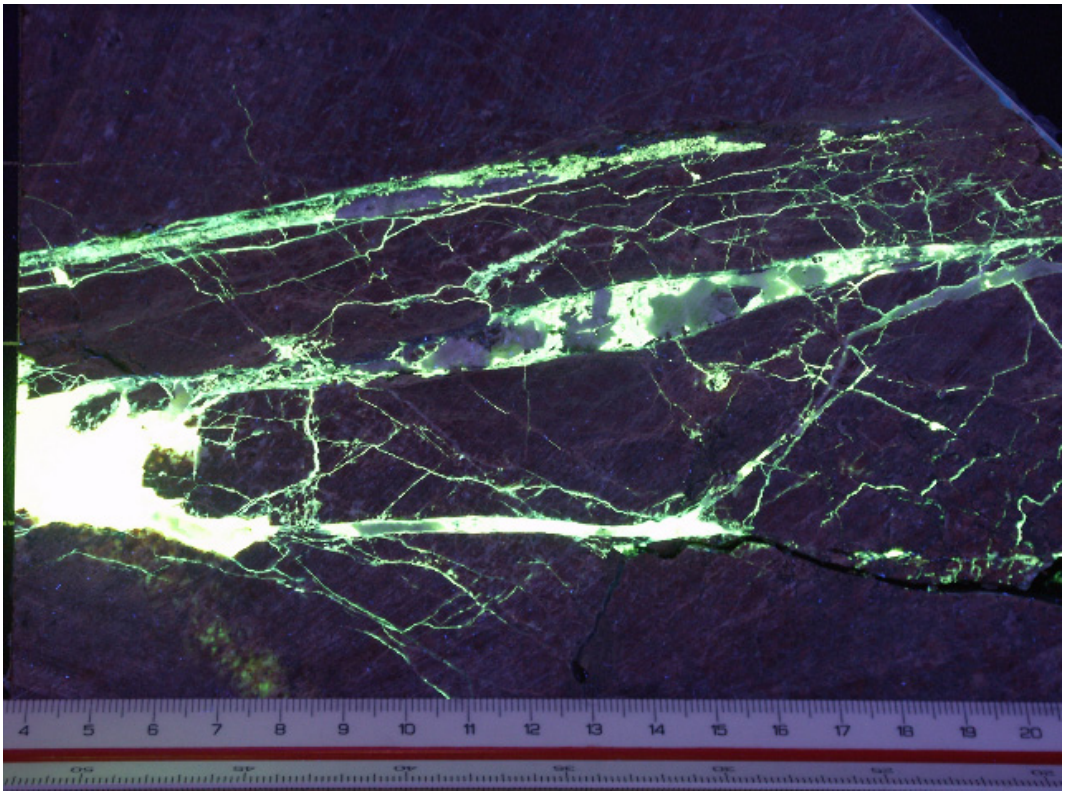

Figure 6-5. *B2-a1: the UV image corresponding to the image in Figure 6-4.*

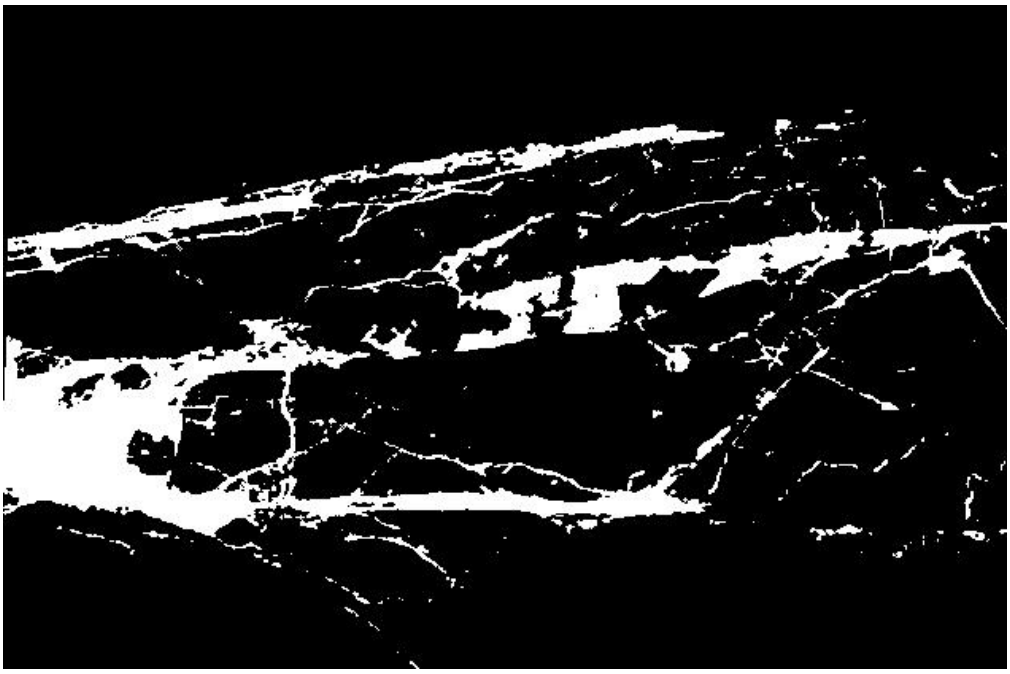

Figure 6-6. *B2-a1; Binary image after the image Figure 6-5 has been converted to grey scale (image based on the green image and a light smoothing and finally an automatic BCV thresholding have been performed). This image is also shrunk compared to the original image and the image size is now 640×480 pixels. The scale factor is 0.264 mm/pixel.*

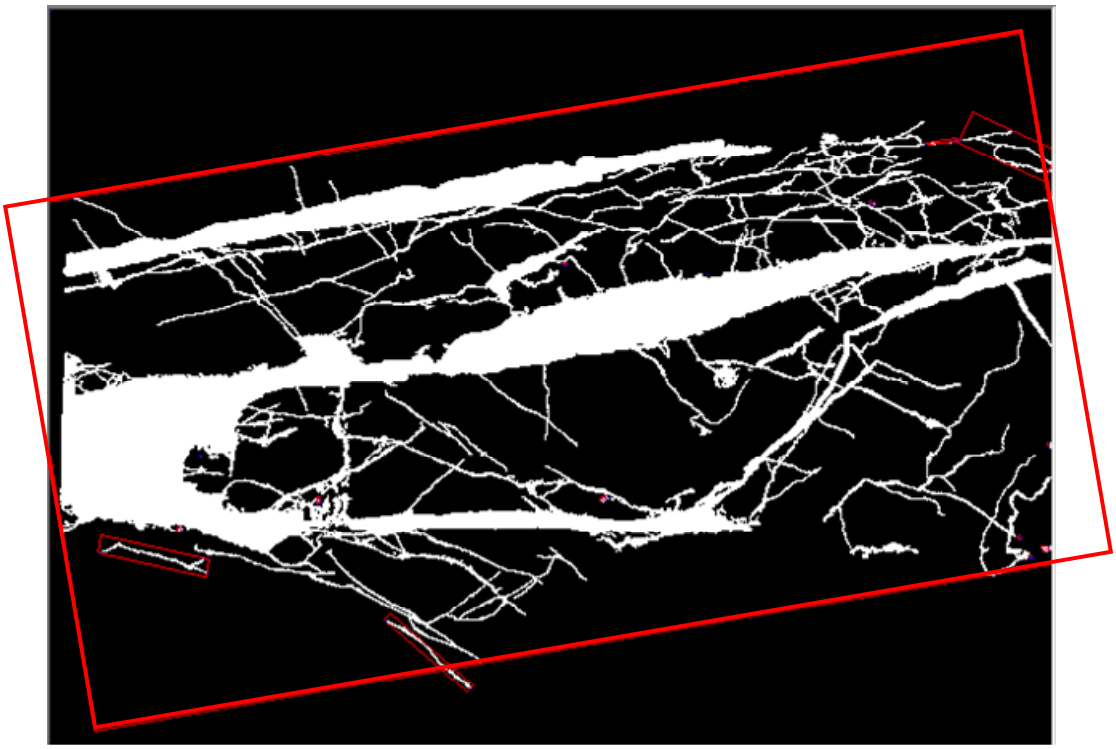

Figure 6-7. *B2-a1; "binary image"; the image is, after auto thresholding, further processed to get the resulting connected fracture network (one large object). This image is used as the starting point for the network analysis. The fractured zone is circumscribed by a minimum size rectangle, a so-called Ferret Box (the largest red box in this case) that is determined from a combination of the network centre and its second moments and boundaries.*

To calculate some kind of porosity for the whole fracture zone it is required to determine the area that could be regarded as being the area of the fractured zone. This task could seem straightforward but is by no means trivial. From the example given in Figure 6-7 it is difficult to say if the outer part of the zone should simply be at the wall of the upper major fracture, or at the termination of the small connecting fractures, as the red square indicate. Maybe the zone does actually extend outside the image where some additional sub-parallel fractures are found. Obviously, if the porosity is calculated as the simple percentage of pores (epoxy-filled in our case) then the porosity will be mainly dependent on how the "area" (Ferret box) of the fractured zone is determined. For this reason the authors are reluctant to use this parameter, but have still tried to use it.

The red square in Figure 6-7 is calculated as the smallest rectangular object that circumscribes the largest object of the binary image. The sides of the objects should be in the same direction as the ellipse that has the same moments around the axes as the object has. The ellipse axes pass through the centre of gravity of the object. As is readily seen, with this definition the Ferret Box will rotate quite parallel with the major fractures and the box width should be a fair measure of the area of the fractured zone.

The binary image can provide information such as porosity, size and shape, and orientation of fractures, but no information on the connectivity, space density, and complexity of a fracture network. As described in Section 4.2, skeletons of the fracture network need to be produced first. There are many skeleton algorithms in the literature; most of them produce detailed information of skeletons of objects. In our case, a network includes a lot of fractures, some of them are thick (but including loose particles, and with rough boundaries) and some of them are thin. To make skeletons for these kinds of networks, it was preferred to mainly consider the principal skeletons, and not the auxiliary skeletons caused by the boundary roughness and particles, because the auxiliary skeletons may cause an overestimation of fracture density. In parallel to testing out different algorithms, a morphological algorithm was employed for skeletonisation that detects the principal skeletons, and is non-sensitive to the boundary roughness and particles (see Figure 6-8). The image can then be used for calculating the fracture space density and average thickness. The problem is that these skeletons are not completely connected to each other (being simply segments), in which case, the particles and junctions cannot be detected. In order to detect junctions and particles, another skeleton algorithm was used (sometimes called thinning algorithm) that makes skeletons continuous (see Figure 6-9 and Figure 6-10). To distinguish it from the first skeleton algorithm (morphological skeleton algorithm), the latter is denoted the Thinning algorithm in what follows. After detection of junction points, these points were subtracted from the network and a fracture "branch image" was obtained. An example is shown in Figure 6-11 (the sample image is taken from a B3 slice).

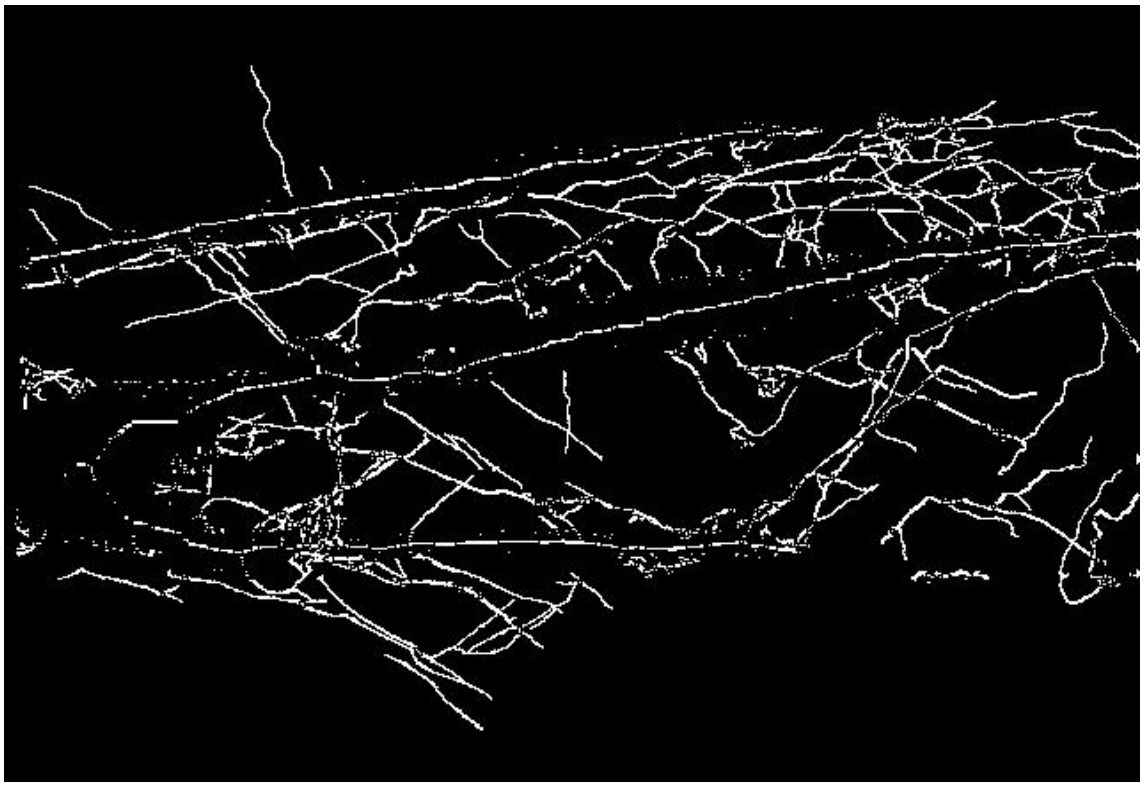

Figure 6-8. *B2-a1, Skeleton image; Morphological operations used on the binary image to abstract the skeletons of fractures.*

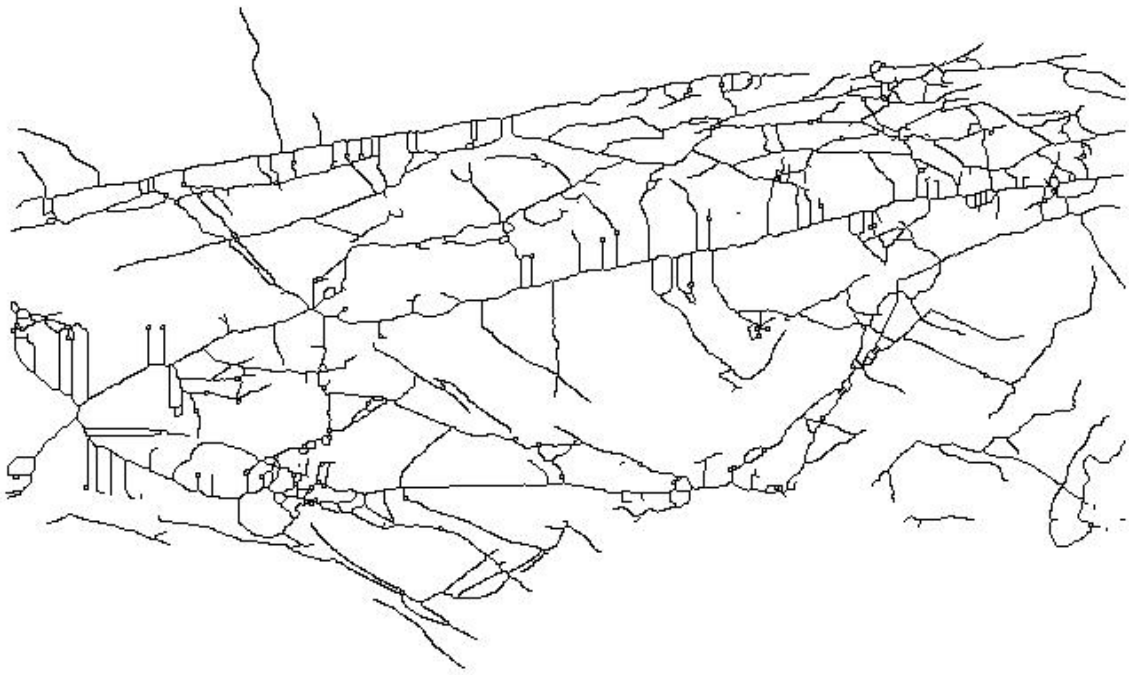

Figure 6-9. *B2-a1, Network image (Thinning image); from this network, one may estimate the connectivity and complexity of the network. It is used for calculating the number of junctions and to study fracture branches.*

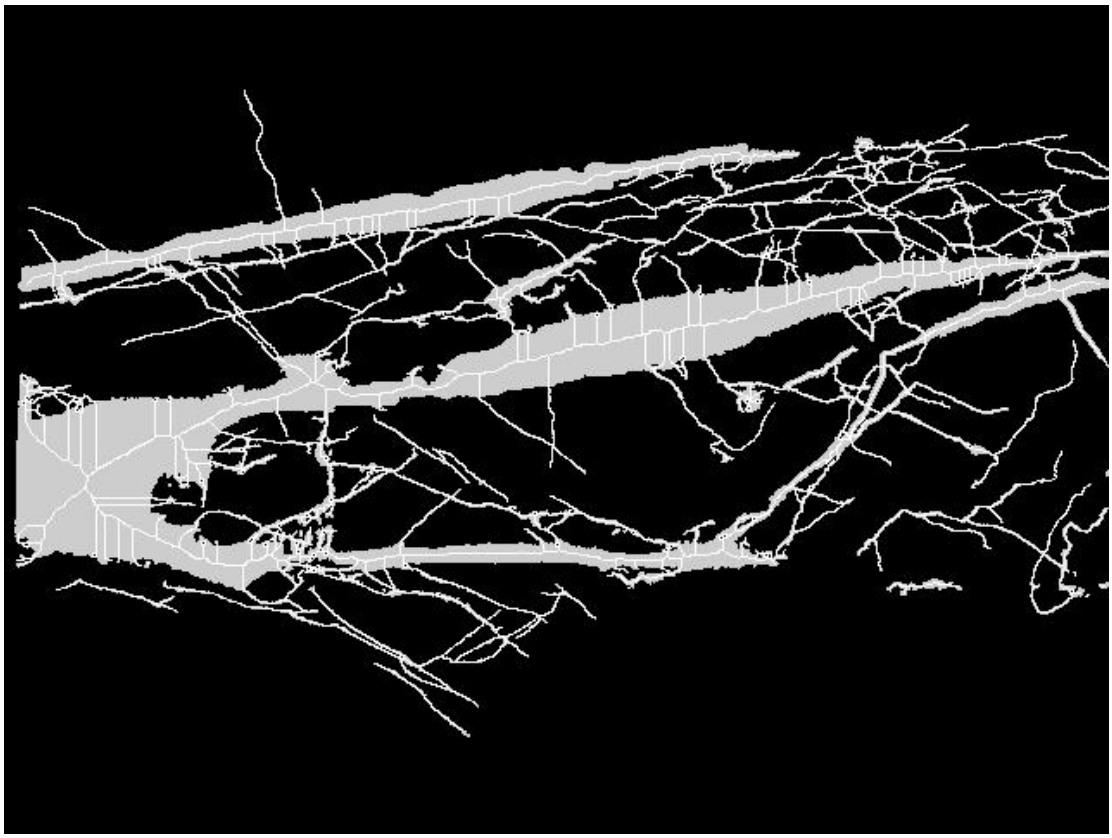

Figure 6-10. *B2-a1, Network image overlay on the binary image; here, the grey colour represents the detected fractures, and the white colour represents the skeletons.*

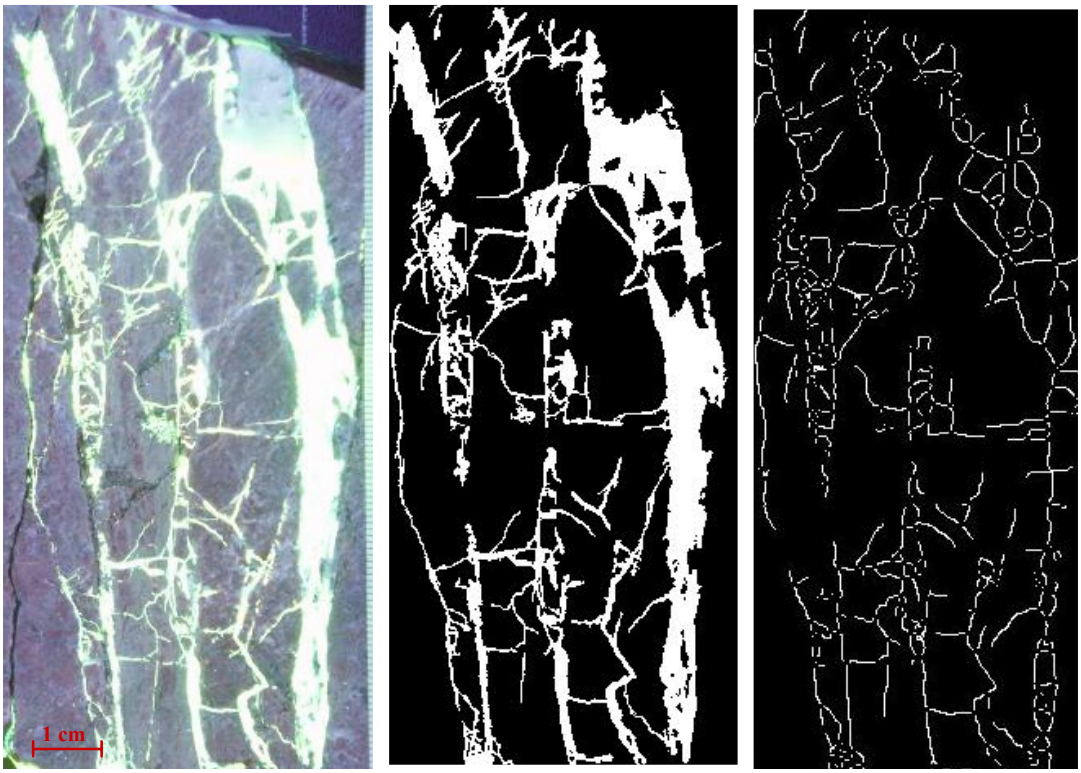

Figure 6-11. *B3-a3 image processing results; (a) original image, (b) binary image, and (c) branch image.*

6.3 Two dimensional fracture network property analysis

For each of the seven UV images from the B2 slices the following base data were measured: Ferret lengths (L) and widths (W, width is the direction across the zone), the epoxy filled area (A_e), the skeleton (net) area (A_n), the number of particles (P) and the number of junctions (J). The results are listed in Table 6-1.

Table 6-1. B2 slices - basic data.

Slice[1]	L [mm]	W [mm]	Epoxy area, A_e [mm^2]	Net area, A_n [mm^2]	Particles, P	Junctions, J
a1	173	87	1,863	1,074	163	138
a2	173	88	2,257	982	95	95
a3	150	86	1,912	824	92	124
a4	150	86	2,148	835	137	98
a5	131	82	1,867	684	96	93
a6	124	76	2,179	660	82	50
a7	84	57	1,267	253	65	128

1 This is actually the a-side of a certain cut of the sample (the b-side of the cut was not analysed). In the following this a-notation is for simplicity omitted in some cases.

To present different characteristics of the fracture network observed in the B2 slices, the basic data in Table 6-1 were used to calculate a number of characteristic parameters described in the following.

Figure 6-12 presents the variation in fractured zone size (L×W) and shows that the area of the zone decreases from slice 1 to 7, caused mainly by a decreasing section of the zone captured in the images (clearly seen from sample photos in Figure 6-3). This parameter, as such, thus does not describe any interesting change in the zone character, but it may still be important in the evaluation of other results. It is relevant as a "check" parameter and the original image should be consulted to find the explanation if any strange variation is noted. In this particular case the decrease in zone coverage may explain some of the trends seen in other parameters.

Figure 6-13 shows that the *porosity* of the fracture network ($A_e/(L \times W)$) is fairly stable and the average value is 18.6%. From slice 1 to 7 the porosity varies between 15-23%. As indicated previously, the parameter porosity is difficult in the sense that the value becomes sensitive to the way the "fracture zone area" is defined, cf. Section 6.2.

The average aperture for all fractures in the network may be calculated as A_n/A_e and gives a similar value between slices, varying from 1.7 to 5.0 mm. However the average aperture calculated in this way is regarded not so relevant in the case of a fault zone, since it is well known that the aperture is certainly not evenly distributed. A fault normally has one or a few fractures with much larger apertures and a network were some of the fractures are very thin. Therefore there is not of much interest to calculate a mean aperture that might be misleading in the sense that no fracture is actually expected to have this aperture.

In Figure 6-14, the average *total* aperture of fractures is shown. This parameter is obtained by dividing the total fracture area (which is approximated by the total area of the epoxy A_e) by the Ferret length, L (length in the direction parallel to the fracture zone plane). The advantage of this parameter (over the average aperture) is further that it is less sensitive to number of thin fractures and thus to image analysis resolution. The advantage of this parameter over the porosity parameter is that the definition is not dependent on a difficult definition of "fracture zone thickness". In B2 slices, the total aperture varies between 10.7 to 17.6 mm, with a 14 mm as a mean value.

Figure 6-15 shows the average space distance (density) both for fractures and skeletons. The average fracture space distance varies between 18 to 25 mm, and the average net (skeletons) space distance varies between 23 to 30 mm. In Figure 6-16, it is assumed that all the fractures are oriented parallel with the longest side of the Ferret Box; the number of main fractures in this length direction can be calculated using the established fracture skeletons. The number of fractures in each slice, in accordance with this procedure, is about 6.

Figure 6-17 and Figure 6-18 present particle density (the number of particles per cm length) and junction density (the number of junctions per cm length) for the seven slices, respectively. The particles could be minerals or some fracture filling materials which may affect transport and retention properties.

Junction density is calculated as the total number of junctions divided by the length. A more complicated network has more fracture junctions. The highest values for junction density are obtained for slices 3 and 5; their fracture patterns are more complicated than the fracture network in the other slices, as may be qualitatively noticed also directly in the images in Figure 6-18.

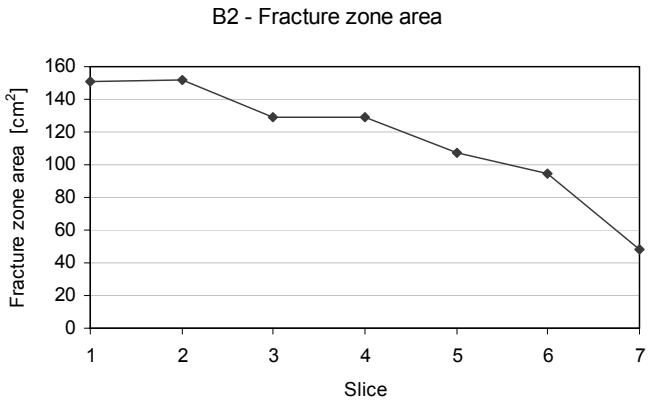

$$Fracture\ \ zone\ \ area = L \times W$$

Figure 6-12. *B2 – Fracture zone (Ferret Box) area variation.*

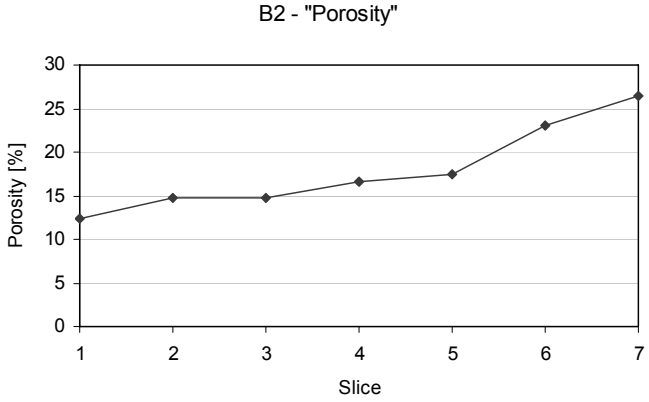

$$"Porosity" = \frac{A_e}{L \times W}$$

Figure 6-13. *B2 – slice porosity variation, for a discussion on porosity, see Section 6.2.*

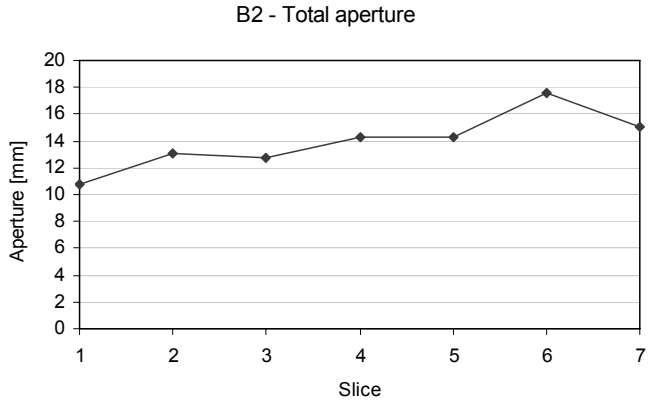

$$Aperture = \frac{A_e}{L}$$

Figure 6-14. *B2 – Total fracture aperture, i.e. the average sum of all apertures in a section across the fracture zone. A_e is the area of all epoxy in the image and L is the length along the zone plane.*

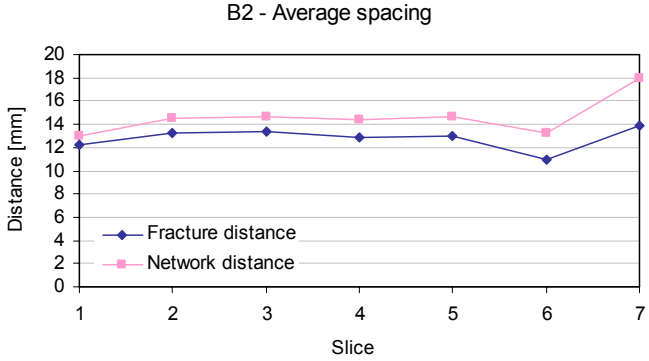

$$Fracture\ \ spacing = \frac{L \times W - A_e}{A_n}$$

$$Network\ \ spacing = \frac{L \times W - A_n}{A_n}$$

Figure 6-15. *B2 – average fracture spacing (distance measured from fracture wall to fracture wall) and average network spacing (centre to centre distance measured between fractures).*

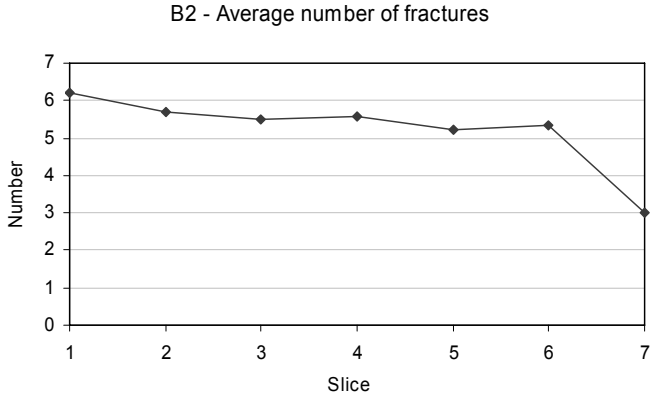

$$Number = \frac{A_n}{L}$$

Figure 6-16. *B2 – the number of main fractures in the individual slices.*

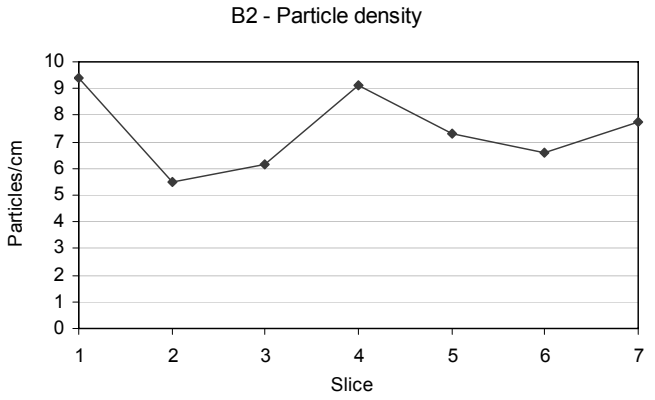

$$Particle\ density = 10 \times \frac{P}{L}$$

Figure 6-17. *B2 – Variation in particle density in the individual slices.*

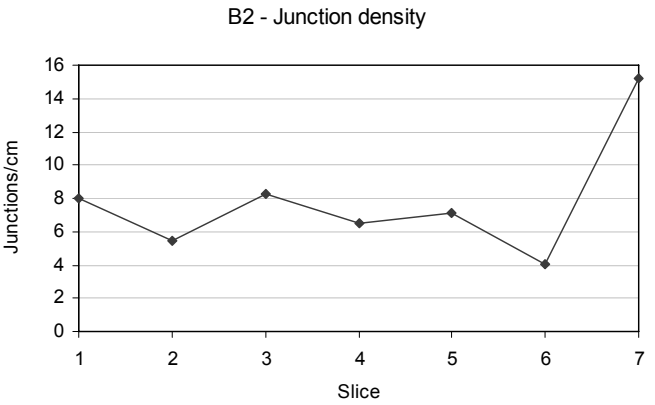

$$Junction\ density = 10 \times \frac{J}{L}$$

Figure 6-18. *B2 – variation of junction density.*

The same analysis has been performed for the sample B3 slices. In B3 the first four slices have similar Ferret Box orientations. Since Ferret Boxes for slices 1-4 involve the same fractured zone, the 5-8 slices only include a part of the fracture network, and the remaining slices are outside the same fractured zone. The detailed measurement results are listed in Table 6-2.

In Figure 6-19, it may be noted that the fracture zone size is stable from slices 1 to 4, and the remaining slices have a larger zone size. The porosity and thickness of the fractures (Figure 6-20 and Figure 6-21) decrease sharply from slice 1 to 12. The number of fractures is about 4 in slice 1 to 7 (Figure 6-23). The space distance increases (Figure 6-22) from slice 1 to 12. The particle density (Figure 6-24) is about 5 for slice 1 and 8, whereas the particle density is close to zero in the remaining slices. In Figure 6-25 it is shown that the junction density is about 25 cm^{-1} from slice 1 to 8, and that the values on the junction density in the remaining slices is very low.

Table 6-2. B3 slices – Basic data.

Slice[1]	L [mm]	W [mm]	Epoxy area, A_e [mm^2]	Net area, A_n [mm^2]	Particles, P	Junctions, J
a1	125	49	1,559	528	140	265
a2	127	57	1,547	490	118	235
a3	128	57	1,613	547	124	244
a4	126	51	1,120	429	116	222
a5	130	123	1,232	541	89	154
a6	136	119	1,082	568	77	166
a7	116	116	705	423	74	131
a8	109	102	471	303	32	104
a9	120	120	527	280	4	33
a10	99	97	230	162	9	17
a11	107	87	143	118	0	5
a12	99	86	121	100	5	13

1 This is actually the a-side of a certain cut of the sample (the b-side of the cut was not analysed). In the following this a-notation is for simplicity in some cases omitted.

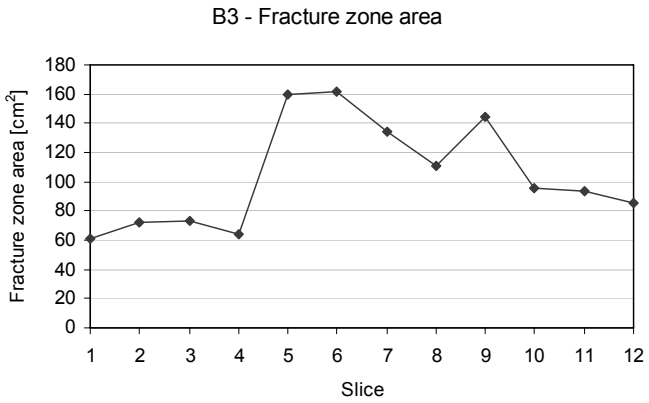

$$Fracture\ \ zone\ \ area = L \times W$$

Figure 6-19. *B3 – fracture zone area (Ferret Box) variation.*

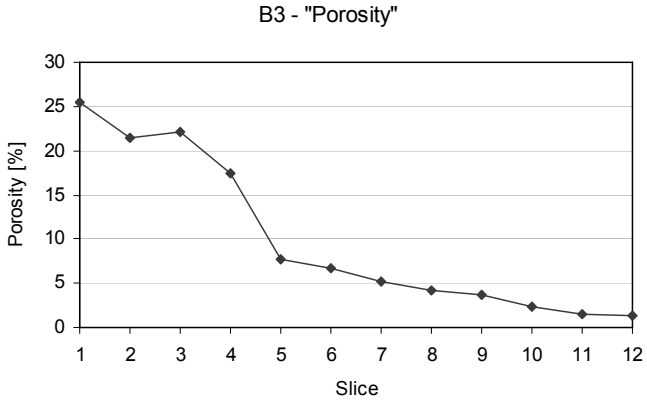

$$"Porosity" = 100 \times \frac{A}{L \times W}$$

Figure 6-20. *B3 – porosity variation related to different slices. For definition of porosity, see Section 6.2.*

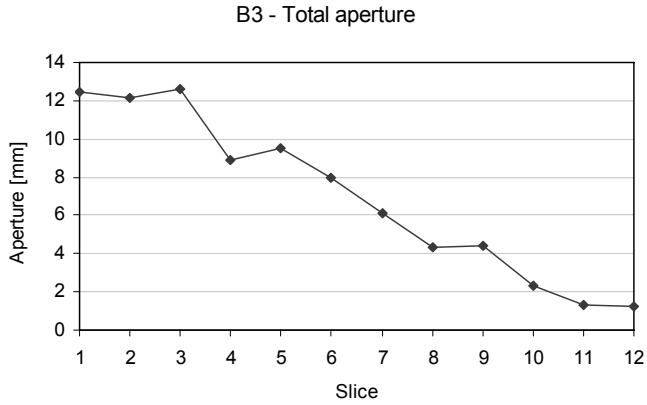

$$Aperture = \frac{A_e}{L}$$

Figure 6-21. *B3 – slice fracture aperture.*

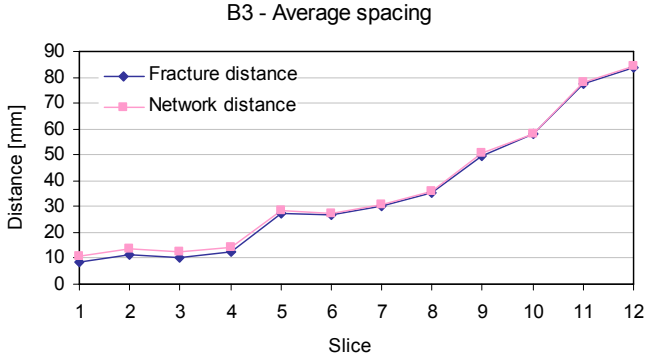

$$Fracture\ dis\tan ce = \frac{L \times W - A_e}{A_n}$$

$$Network\ dis\tan ce = \frac{L \times W - A_n}{A_n}$$

Figure 6-22. *B3 – Fracture spacing is spacing between fractures (fracture wall to fracture wall) and network distances is the distance between fracture centre to fracture centre).*

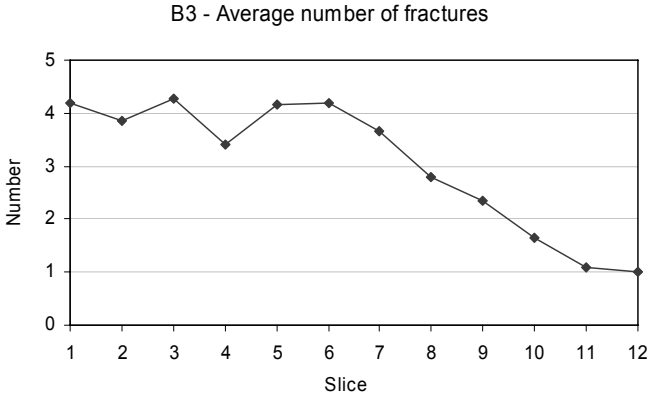

$$Number = \frac{A_n}{L}$$

Figure 6-23. *B3 – average numbers of network branches.*

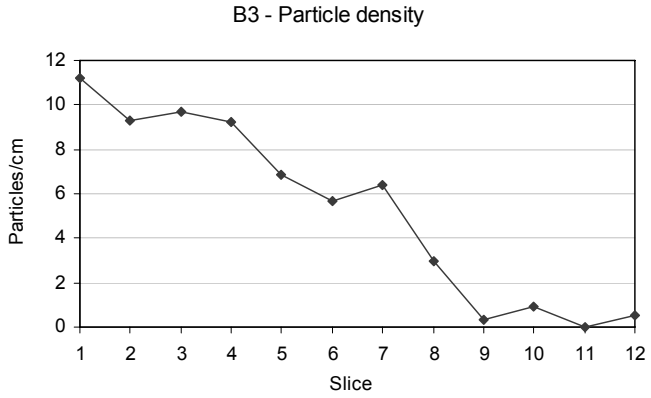

$$Particle\ density = 10 \times \frac{P}{L}$$

Figure 6-24. *B3 – particle density variation.*

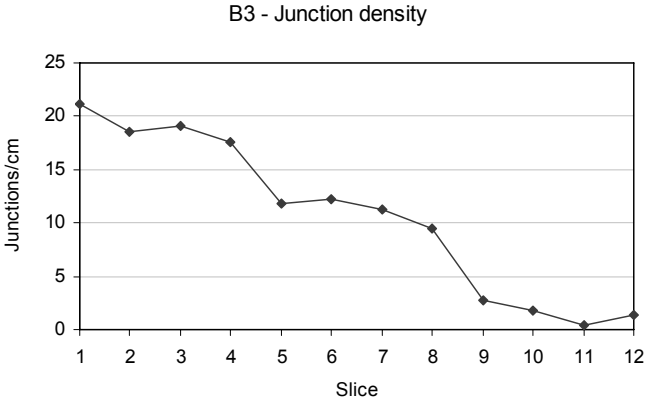

$$Junction\ density = 10 \times \frac{J}{L}$$

Figure 6-25. *B3 – junction density variation.*

When comparing the results from samples B2 and B3 some similarities and differences are notable. The fracture zone area is not relevant for comparison, since this area is a result the slice cutting location only. However, the Ferret width is in the same order for both samples. This is to be expected since the samples are located close to each other and the width should not be dependent on the orientation. The porosity value determined is also similar for the B2 and B3 samples (if we consider B3 slices 1 to 8 only, and more weight is attributed to slices 1 to 4, as discussed previously). The particle density is of the same order for both slice cutting directions, as defined by B2 and B3.

The only clear difference seen is in the junction density which is around 7 in B2, compared to about 19 in B3 slices 1 to 4 and around 11 in slices 5 to 8. This is important given that one of the selected parameters does pick up the difference in shape character that is possible to observe visually from the overview images in Figure 6-2(a) and Figure 6-3. The shapes of the "blocks" of the network are more square-shaped in B3 compared with the more lens-shaped blocks seen in B2. There seems to be more "dead-end" thin fractures in B3. The interpretation is that most of the shear movement has been more (sub-) parallel to the B2 images planes than to the B3 planes. A dominant direction in shear movement will naturally induce anisotropy in the fracture pattern. The orientation of shear is sinistral, when looking at the a-side of the B2 slices and this corresponds to a sinistral shear displacement of the subvertical fault zone studied.

7 Single fracture analysis

The main purpose of the project has been to study the fault rock and the approach taken has been described in the preceding chapters. However, in other cases it may be the objective to study the aperture distribution of a single fracture, i.e. a fracture consisting of only one single fracture plane with associated pore space. In this chapter it is therefore exemplified what kind of approaches that may be applied, and what difficulties that must be resolved when analysing the apertures of single fractures.

For this purpose, using the same rock sample slices from the fault rock, microscopic images were photographed along two identified fractures being part of the zone (marked with red in Figure 7-1). Two slightly different analyses were performed, one which concerns a single fracture with fairly constant aperture. This is the upper of the two fractures (Fracture I). Images were taken with a microscope but with a lower resolution (0.0114 mm/pixel), i.e. each image covered about 8 mm of the fracture trace on the cut rock slice surface.

The lower fracture (Fracture II) has a more complex geometrical structure and the images were in this case acquired with the microscope with higher resolution (0.00426 mm/pixel), i.e. each image covers about 3 mm of the fracture trace.

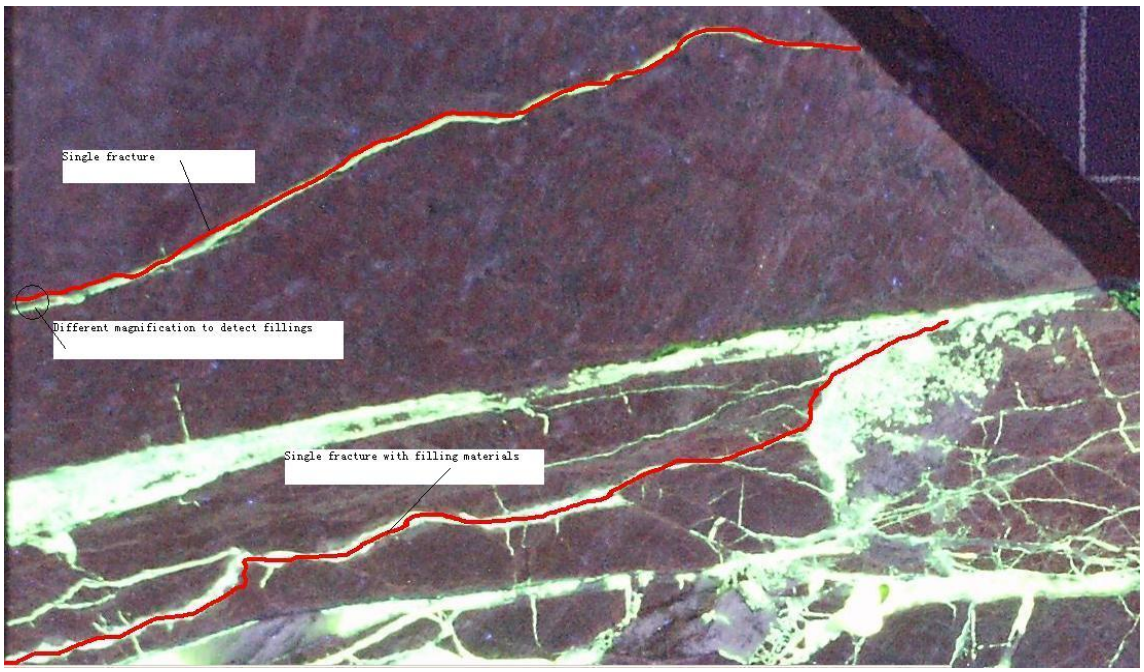

Figure 7-1. *Part of the B2-a4 slice. The red curves marks the two fractures analysed, the upper fracture, Fracture I and the lower, Fracture II.*

7.1 Analysis of single fracture at low resolution – Fracture I

Fracture I (top-red curve in Figure 7-1) with a total length of about 120 mm was photographed with continuous, slightly overlapping, images (720×576 pixels) The original images were merged together, by taking away all overlaps, to ascertain a correct representation of the fracture along its length.

For each of the totally 12 "merged images" (Figure 7-2 and Figure 7-3) first image filtering was made to remove the noise, followed by binarisation to extract the epoxy-filled part of the fracture. After this the total fracture length was divided into 68 segments (average segment length, in the fracture plane direction, is about 1.7 mm). Figure 7-2 presents both the original and the processed version of the first image and Figure 7-3 shows the processed version of the following images. (The images printed in the report are shrinked versions of the images, to enable an overview, and all image details can therefore not be observed in this report). Each fracture segment hence consisted of a white elongated object, and the analysis of the pore space geometry was made on each such object

Here it should be noted that the issue of aperture definition is not so trivial when it comes to actual measurements. The aperture may be defined as a point wise entity. For example /Hakami, 1995/ uses the definition of aperture of the pore as the distance from one side of the fracture (pore) to the other, always measured in the direction perpendicular to a reference plane parallel to the overall fracture plane (i.e. assuming that the fracture plane is roughly planar). Another definition could be the shortest distance between the two fracture surfaces at each point. With this definition the measurement of the aperture will be made in different directions from point to point, which makes the integrated calculation of void space and associated statistics more complicated.

Furthermore, it is not possible to make ideal point-wise aperture measurements because, irrespective of the method used for measurements, there is a minimum of "point size" needed. Using image analysis, the smallest point size would be the pixel width size of the image. This way of measuring aperture was used in e.g. /Hakami and Gale, 1998/. The amount of work and data may then become large if the distance between the measurement points is small. This type of measurement is the best for detailed determination of spatial variability. If the fracture geometry is not very simple there is still a need of a decision as to how to handle the points where the apertures are divided into two or more parts (caused by branching or fragments inside the fracture).

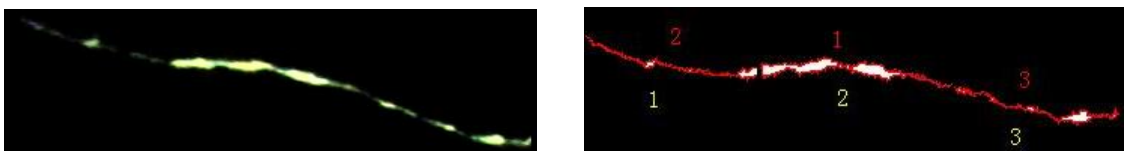

Figure 7-2. *The first image of the single fracture I and the corresponding image after it were segmented into fracture parts. (The outermost pixels of the white objects are coloured red and the white figures are segment number along the fracture (Width of images c. 5 mm).*

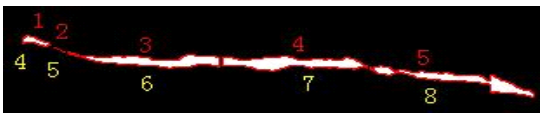

The second image of the fracture

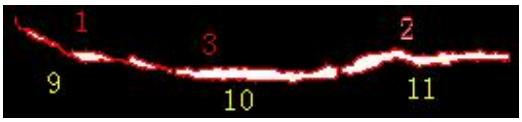

The third image of the fracture

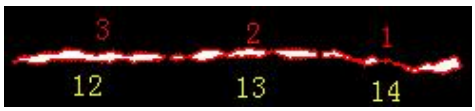

The fourth image of the fracture

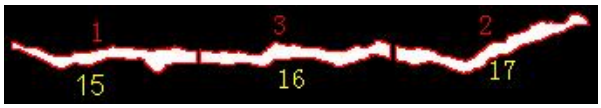

The fifth image of the fracture

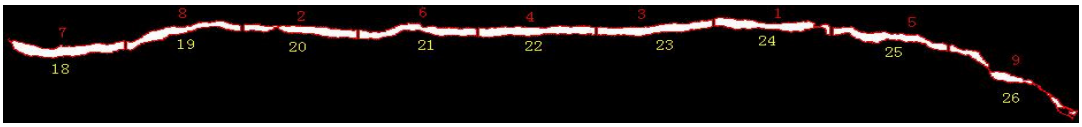

The sixth image of the fracture

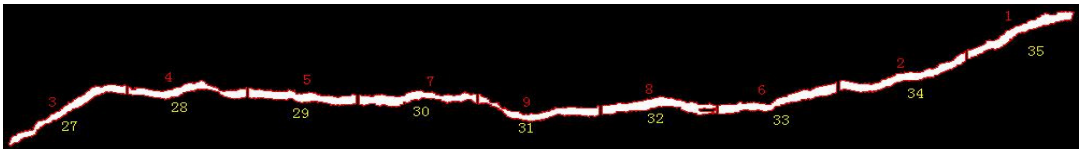

The seventh image of the fracture

The eighth image of the fracture

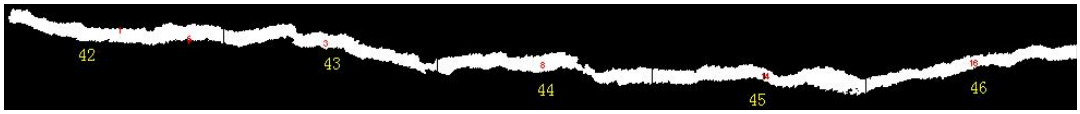

The first part of the ninth image of the fracture

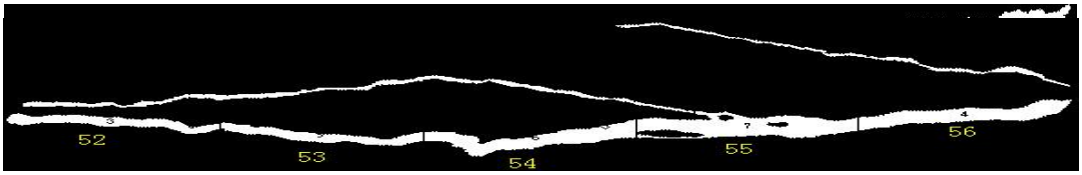

The tenth image of the fracture

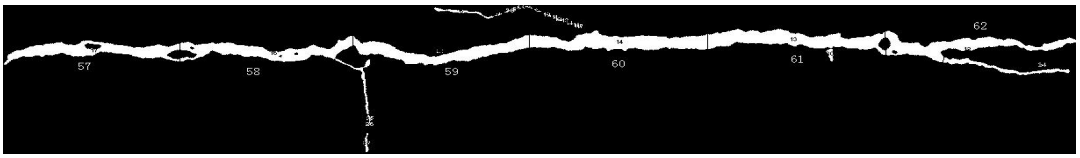

The eleventh image of the fracture

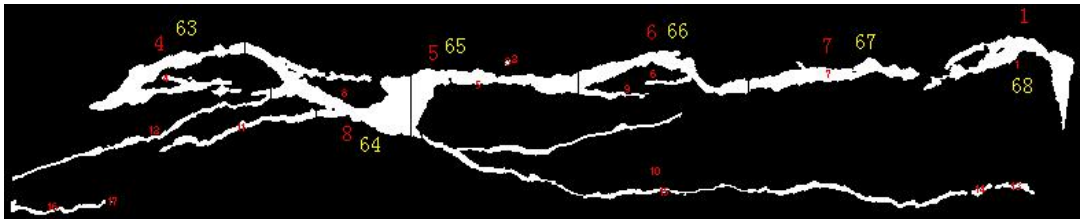

The twelfth image of the fracture

Figure 7-3. *The 2 – 12th image of the single fracture I. (The white numbers show the continuous numbering of the segments along the fracture included in the analysis.) The first image is seen in Figure 7-2.*

However, any other larger “point size” than the single pixel width size could also be chosen and the average value from this “point” be used as the representative average value for this “point”. For the example study presented here the fracture was manually divided into segments (each including a single white object corresponding to the epoxy filled pore) of slightly different sizes, about 1.7 mm long. For each white object a number of geometrical parameters were determined. The most important, and easiest to calculate, is the total area of the object. If this area is divided by the extension of the object in the fracture direction this gives some kind of average value of the aperture. At least when the geometry of the fracture pore space is quite simple (i.e. fairly tabular), as in this case, this type of average value should be close to what is desired and be a sufficiently good characterizing parameter.

If the spatial variation is of importance and the correlation distance is desired the measurement point size (in our case the segment length) must be clearly smaller than the expected correlation length to enable such spatial characterization. This roughly means that the segment should be in the same order as the mean aperture. In this example case (Fracture I) the segments are too long, about 1.7 mm compared to an average aperture of typically 0.2 mm, to be suitable for spatial correlation studies (e.g. for making variograms).

The results from the aperture determination of the segments in Fracture I are given in Figure 7-4. The aperture parameter given is in this case every segment’s object area divided with the object scan length, i.e. the length in the x-direction of the image. This will give an average aperture for each segment.

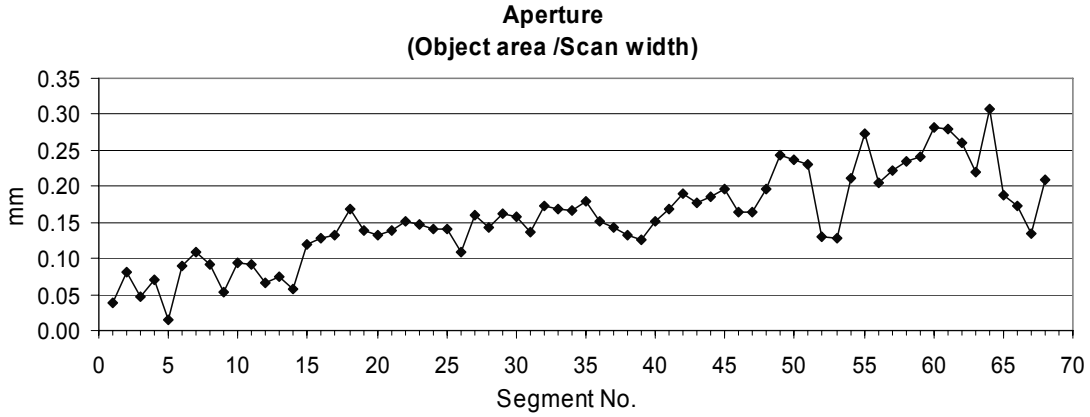

Figure 7-4. *Aperture distribution of a single fracture (see Figure 7-3). Each segment is a part of the fracture pore with a length along the fracture profile of about 1.7 mm. The calculated mean aperture for each segment is the area of the white epoxy filled object of the segment divided by the length of the segment.*

7.2 Analysis of single fracture at high resolution – Fracture II

The second example of analysis concerns a single fracture (the lower red fracture in Figure 7-1) which was photographed with a shorter focal distance and thus giving more close-up images. In Figure 7-5, five continuous example images are presented. The fracture (epoxy-filled) aperture, shape and colour vary from image to image. In Figure 7-5 a) the fracture surfaces are very rough and there are several branches and in Figure 7-5 b) the boundaries of the fracture are fairly blurred due to too intensive light conditions. In Figure 7-5 c) the fracture has rather uniform surface, but has a relative large "hole" in the fracture, and in Figure 7-5 d) there are also some loose small rock fragments inside the fracture opening. In Figure 7-5 e) the fracture has a rough surface, and some edges are not clear. The different images of Figure 7-5 illustrate that when information amount increases with increased resolution, the difficulty of image processing and analysis also increases.

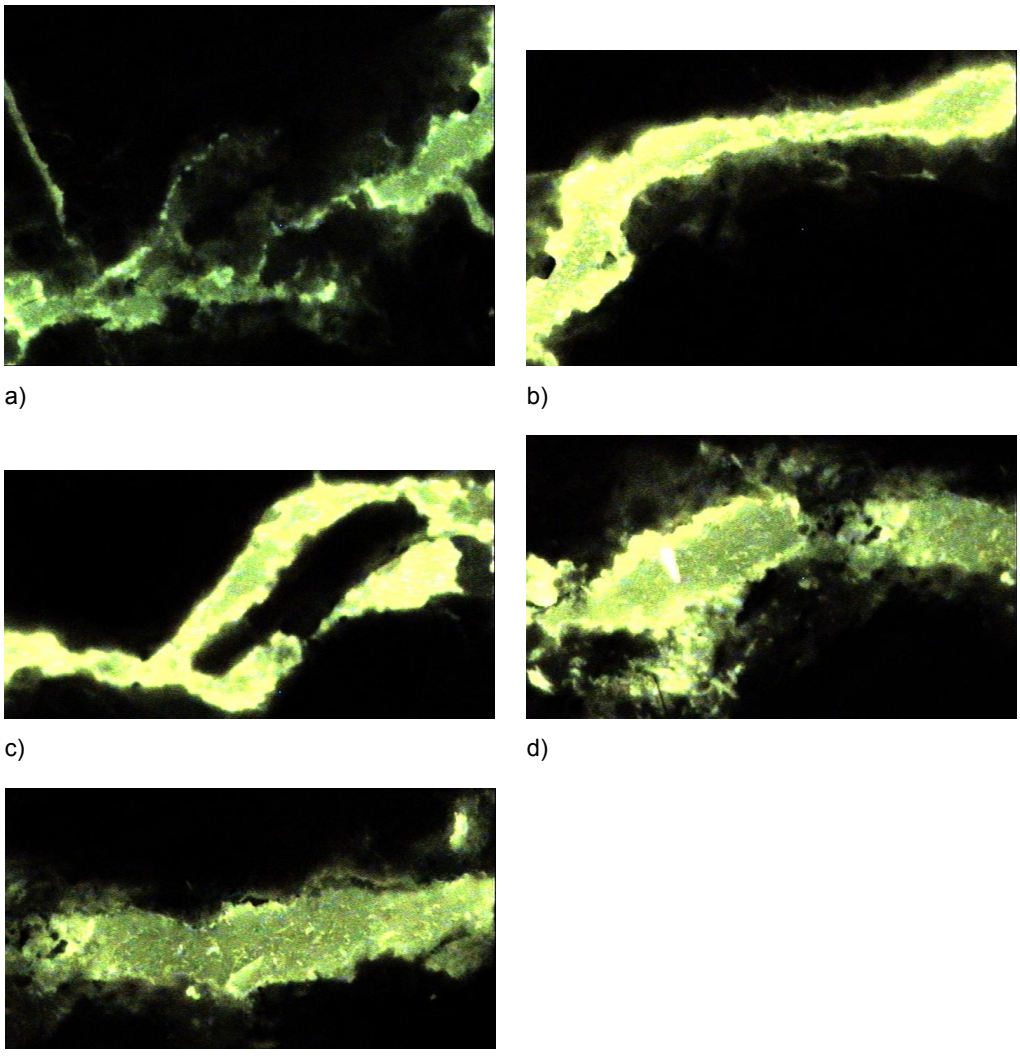

Figure 7-5. *Five neighbouring images for the lower red-marked fracture in Figure 7-1 (Fracture II), the scale factor is 0.00426 mm/pixel. Total width of each image is ca 3 mm.*

In this study the specimens were positioned by hand below the microscope, which has a strong influence on the exact image frame location, the images had to be manually connected together after the acquisition. Figure 7-6 shows an example where eight image are perfectly connected into one continuous fracture image. To avoid this kind of manual manipulation work due to overlap, a mechanical device for taking microscope images may be useful, enabling improved control of the locations of image frames.

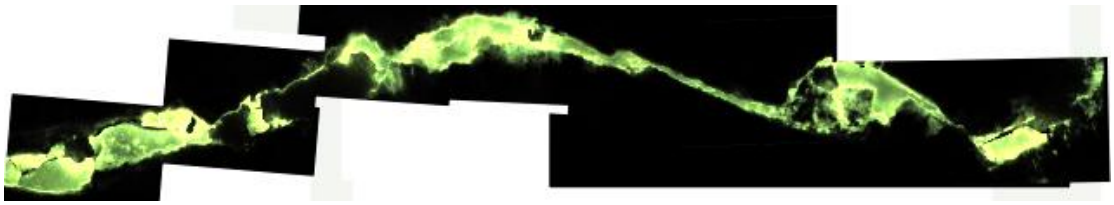

Figure 7-6. *Eight original images are here connected and merged into one continuous fracture. (Parts of this image are shown as more close-up images in Figure 7-7 through Figure 7-9).*

Figure 7-7 through Figure 7-9 present close-up images of the same continuous fracture cut into three parts. The aperture analysis was carried out by first producing a binary version using a threshold on the brightness in the grey-scale picture (as previously described in Section 3.3.1).

Also, as in the previous example case, the point wise aperture parameter, using a single pixel intersection with the fracture, has not been applied but the approach of average segment aperture was used. The fracture was split into a total of 24 segments, each constituting one white object in the image analysis.

In this example analysis, for each object a number of parameters were determined, and the results for these first 24 segments are given in Table 7-1. The “Area” of the segment is simply the number of pixels in the white object multiplied with the area of a single pixel.

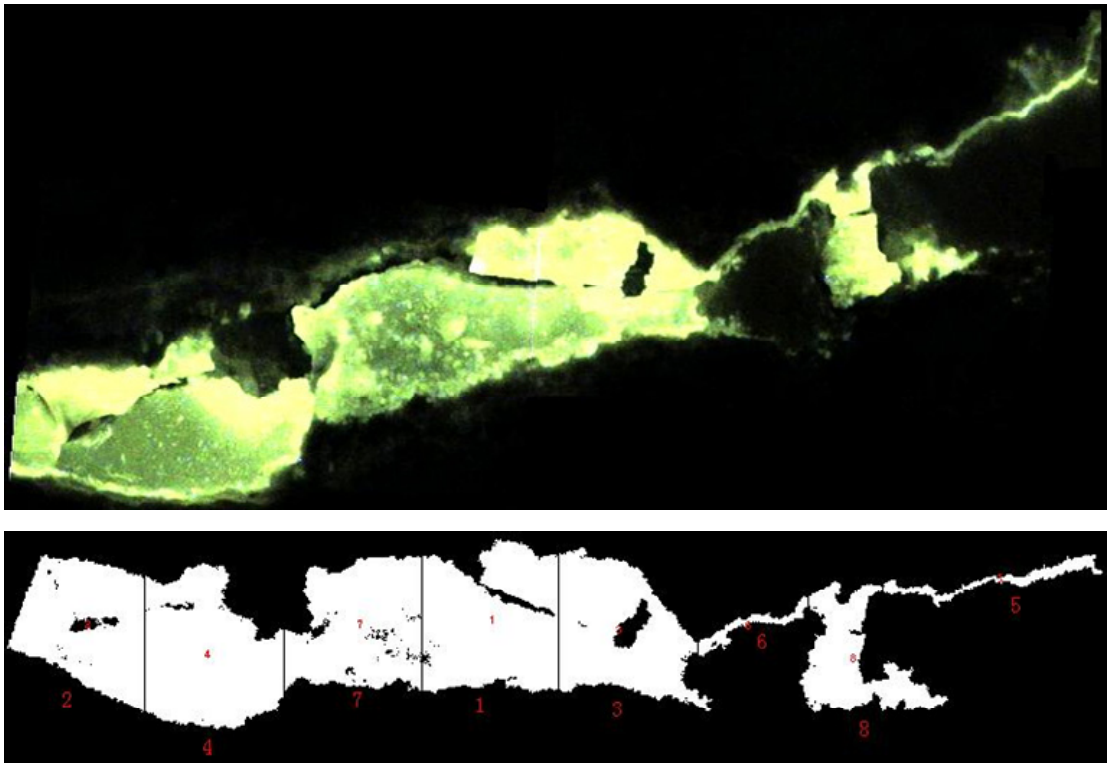

Figure 7-7. *First part of the fracture II as the original colour image in UV-light and its processed result. The binary image is thereafter cut (the black lines intersecting the pore space) into 8 segments .The length in the x-direction of the image (Scan Length) is about 0.4 mm for each segment.*

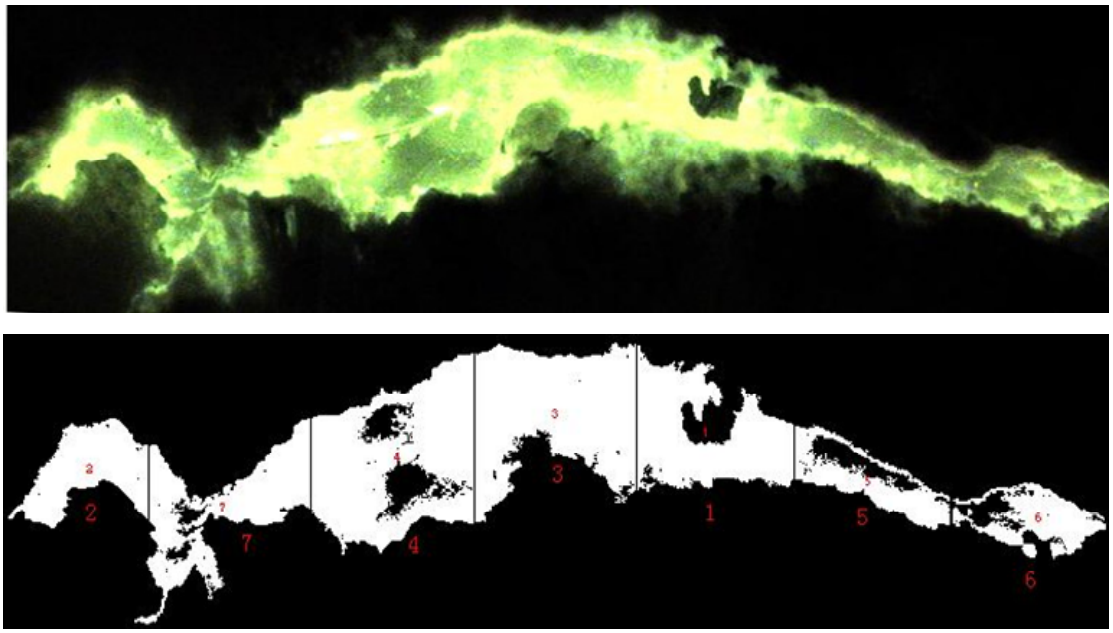

Figure 7-8. *Second part of the fracture II image and its processed result. This image is the continuation of the image in Figure 7-7, (also cf. Figure 7-6).*

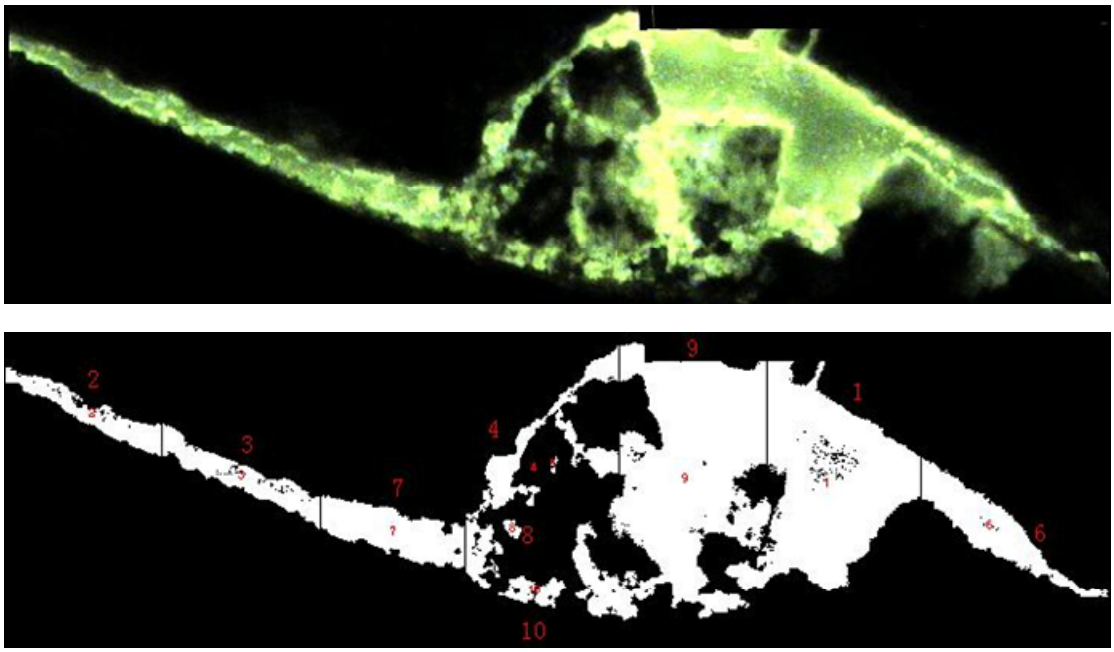

Figure 7-9. *Third part of fracture II image and its processed result. This image is connected to the image in Figure 7-8, (Also cf. Figure 7-6).*

The "Orientation" in Table 7-1 is the orientation of the long axis of the Ferret box of the object (the Ferret box is explained in Section 6.2, and it is a rectangle that encloses the white object and has the same overall direction as the object). This orientation is different from zero when the fracture is not parallel with the image (i.e. not parallel to the coordinate system of the image). This information may be of importance in cases when the planarity of the fracture is low. However, the orientation is only meaningful if the segment length is somewhat longer than the aperture, which is not always the case in our example. The "Scan length" is the maximum distance (in pixels) in the direction of the image x-coordinate of the object, and the "Scan width is the maximum distance in the y-direction. The total sum of the "Scan length" should equal the length of the whole image profile. As discussed previously, it depends on the chosen definition of the aperture if the "Scan length" should be used for the aperture calculation or whether any other length, that takes into account the segment orientation or shape, should be used.

A potential parameter to be used for quantifying the difference between fractures having several fragments and rough boundaries compared with the more simple fracture (without making more tedious detailed point aperture studies) is to calculate for each segment the ratio between the equivalent circle diameter or ellipse width (reflecting the pore volume) and the Ferret box width (reflecting the total size of pore network). This ratio will be lower, and or more variable, in the complex case (as one example, note how the distance between the grey and the black lines varies in Figure 7-10).

Table 7-1. Measurement data for images in Figure 7-7 to Figure 7-9. The units in the table are image pixels (1 pixel = 0.00426 mm).

Segment	Area	Orientation (°)	Scan Length	Scan Width	Ellipse Length	Ellipse Width	Ferret Length	Ferret Width
1	7,283	47.43	114	99	115.51	90.51	132.86	107.55
2	8,941	59.56	120	100	123.98	98.63	132.76	115.74
3	7,583	-41.82	99	97	113.96	94.79	137.38	119.92
4	8,961	-37.68	111	98	116.35	110.55	136.45	135.48
5	7,482	46.75	118	111	130.02	88.29	157.31	101.57
6	579	-20.44	79	44	106.99	15.82	88.41	18.71
7	4,234	53.97	108	95	115.4	79.88	120.99	93.64
8	960	-8.61	159	38	196.52	16.64	159.31	25.03
9	3,370	-24.53	93	72	98.47	58.61	104.62	78.16
10	4,934	-31.98	134	117	158.74	77.97	169.3	107.01
11	8,615	-38.15	131	108	145.03	100.57	149.72	120.74
12	8,283	-8.37	117	107	135.58	102.34	122.61	114.14
13	5,688	21.46	104	95	128.34	79.45	128.32	93.94
14	2,322	24.4	103	69	136.04	34.52	120.33	39.06
15	2,255	7.58	102	50	91.15	43	103.62	48.84
16	1,335	25.41	101	57	127.91	17.01	115.35	21.66
17	1,643	24.34	102	68	133.5	19.01	120.64	22.35
18	2,364	15.68	93	47	109.02	29.69	101.47	32.25
19	2,452	-51.67	156	99	192.24	63.37	177.13	71.36
20	77	48.01	12	12	15.22	8.62	14.53	9.25
21	445	2.38	44	21	42.82	18.54	43.8	20.19
22	12,398	-72.55	179	129	190.14	109.08	190.08	130.25
23	9,364	-86.46	148	127	142.6	105.38	150.87	123.73
24	2,461	36.72	121	90	133.59	27.08	150.4	32.6

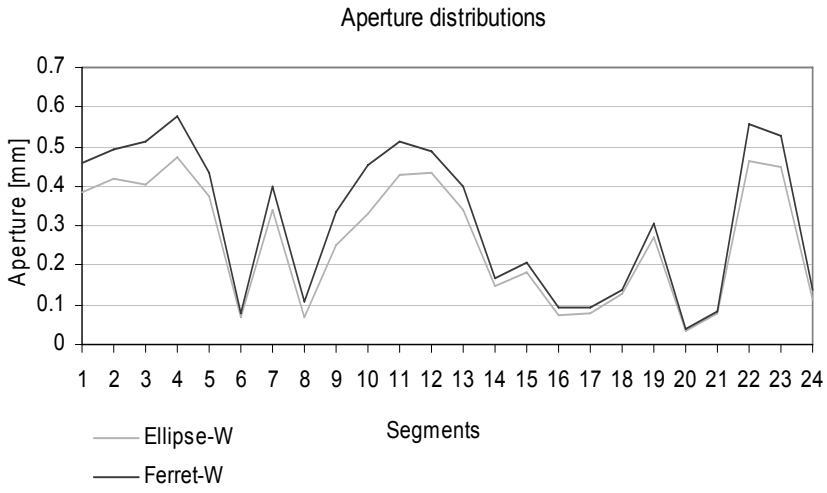

Figure 7-10. *Aperture distribution along a ca. 9 mm long part of Fracture 2 based on the 24 segments seen in Figure 7-7 to Figure 7-9. The data are listed in Table 7-1.*

7.3 Conclusions and recommendation concerning single fracture aperture analyses

In this chapter two examples of aperture measurement and analyses for single fractures has been presented. The following points summarise the conclusions and recommendations related to future aperture measurements on single fractures:

- When image resolution increases, the amount of fracture information increases, but the difficulty in image processing and analysis also increases.
- The definition of the aperture parameters, and the way they are determined (image resolution, segment size etc.), should be chosen depending on the objective of the study and kept constant within the study if detailed comparisons between fractures are to be made.
- For a uniform and simple fracture (without extensive number of fragments/holes and branches, and with a limited fracture orientation variation), the average aperture determined as the segment "Area" divided by "Scan width" is a parameter that is suggested to be satisfactory.
- Due to image quality limitations, on the boundary of a fracture pore, one or two image pixels could be over-counted or under-counted. To alleviate this kind of source of analysis error, one needs to consider the average or minimum fracture aperture (in pixels) to be measured before the choice of image analysis scale is made. For example, if the measured fracture has an average aperture of 10 pixels, the measurement error could be 10-20% on average. If the fracture has an average aperture of 100 pixels, the measurement error would be limited to 1-2% on average.
- If the colour difference in the image is poor, for example because the fluorescence is poor or there is no fluorescent epoxy in the pore, images analysis may still be considered since the ordinary colour image may be used. Alternatively, some combination of the information in ordinary light and UV light imaging may be considered (the latter type of analysis in not exemplified in this report).

8 Conclusions

The study may be divided into three main parts. The first part was the methodology developed for sample collection and elaborated image acquisition of fault rock pore space. The second part includes the methodology development for the image processing and analysis. And the third part is the characterisation and collection of data from the studied fault rock. The conclusions for these parts are summarised below.

8.1 Sample collection and image acquisition

The developed method including impregnation of the fault rock *in-situ*, reinforcing it relative to sampling disturbances and making visible the geometry of the pore space, has worked out satisfactorily.

An important factor is the concentration of fluorescence in the epoxy, which should be high, in combination with good illumination arrangements during the image acquisition. Controlled illumination, using fixed lamp positions, and a stable surrounding (dark room) facilitates the work. Steady image acquisition conditions permit a stable image quality and, as a result, a faster image analysis.

8.2 Image processing and analysis

Image analysis has proven to be a useful tool to identify quantitative parameters that describe the geometrical properties of the pore space of a fault zone fracture network or a single fracture in crystalline bedrock.

Decision on what image processing steps and image analysis to be undertaken in a specific case should be made based on the general character of the pore space, the image quality and, most importantly, the objectives of the specific study.

In order to make the image analysis, as a first step it is necessary to construct a binary (only black or white) image from the original greyscale (or colour) image. Several auto-thresholding algorithms have been studied and compared, and the BCV or OPT algorithms are considered satisfactory for the application on fluorescent epoxy filled rock fracture images.

The amount of epoxy (white in the binary images) is the most important and straightforward characteristic to be determined. This value, in combination with the shapes of the pore volumes, may be used to determine different types of average apertures.

In the study attempts have also been made to determine some fault zone porosity values (porosity here expressed as the ratio between the sums of white areas divided by a “total area”). However, porosity has proven to be a difficult parameter since it is difficult to define unambiguously a “total area/volume”, such that the parameter can be made precise and relevant also for comparison of different zones. The porosity of a fault zone is expected to vary considerably across the zone while being somewhat more constant

along the zone. Furthermore, the lower boundary of a pore size to be included in the determination would also be dependent on the epoxy impregnation and the image scale. Close-up images would consequently tend give a higher value on porosity (as discussed in Chapter 5).

The number of branches in a network is one parameter that may be used as a quantitative characteristic. The approach to measure this entity has been to first make every branch of the network thinner, using image analysis algorithms, and thereafter measuring the area of the network. This gives the average number of fractures in the fault zone samples covered by the image.

The number of junctions is another, similar, parameter that integrates the points where the fractures branches. This parameter is more sensitive to the complexity of the network compared with the average number of fractures. However, sometimes the noise at the boundaries of fracture openings may also create false junctions, which could entail slight overestimation in the number of junctions. Some modification of the junction detection algorithm should therefore be considered if used in future studies.

The number of particles (rock fragments surrounded by the injected epoxy) is also a parameter that may be useful to characterise a fault zone fracture network. This parameter is judged more sensitive to the scale and image quality than the other parameters. The size and shape distribution of the particles are other potentially useful parameters.

8.3 Character of studied fault structure

The minor fault studied was sampled from the wall of the Äspö hard rock laboratory access tunnel with a 300 mm diameter borehole (KA2423A03). Half of the core was used for the study and cut into slices in two perpendicular directions.

Through direct visual studies of ordinary images of the fault cross section, the conceptual understanding of how such structures are geologically built up was improved. Through the image analysis of the UV-light images the pore volume, as in-filled with fluorescent epoxy, could be quantitatively characterized.

The fault zone structure is complex, consisting of on average 5-6 sub-parallel fractures connected to each other. The character of the fractures in the network differs. The major fracture plane is the plane where most of the shear movement has occurred, most probably at several shearing episodes, separated in time. This fracture has a large variation in aperture. At some points the aperture is cm-wide and at other points the fracture is entirely filled with calcite and other fracture filling minerals. Another characteristics of the major fracture is sections with porous infilling, i.e. infilling consisting of packed small crystals of infilling minerals and fragments of the host rock (fault gouge). Mostly this porous material was impregnated with the epoxy, indicating that there is certain porosity/permeability also in these sections.

The general character of the fault zone remained constant at the scale of the studied fault zone sample (about 20 cm long). However, the detailed geometry is not so simple that it enables a direct connection between sections with 2 cm distance, across the thickness of the sample slices, other than for the major fractures of the fault zone.

The width of the studied fault zone is about 6 cm ("width" here being the maximum distance perpendicular to the plane of the interconnected epoxy filled fracture network in the sample). The total aperture (summed aperture from all fractures) is about 14 mm and the average number of fractures (branches) is 5-6 in a section across the zone. An attempt to define a "porosity" parameter was made, but it is shown that this parameter is sensitive to its underlying definition and is therefore not recommended as a characterising parameter.

The anisotropy of the fracture network is observed by the difference in network junctions on planes from sample B2 compared to B3. B2 and B3 are neighbouring parts of the zone which are cut into slices in different directions. The number of junctions per 1 cm section across the fault rock plane is in the order of 7 for B2 and 19 for B3. This is explained by the fact that the fracture network pattern will be determined by the directions of movements on the fault. In planes sub-parallel to the movement (B2) the pattern is less complicated, with fewer junctions and with more smooth lens-shaped particles.

The methodology developed in this study is judged suitable also for application to the conductive structure (Feature A) at the TRUE-1 site, which has been the subject to an extensive series of tracer tests, cf. e.g. /Winberg et al. 2000/.

9 Acknowledgement

The careful and detailed review of this report by Anders Winberg is gratefully acknowledged. Thanks are also due to Malin Johansson who has contributed with editing and proof reading of the manuscript.

10 References

Abanto-Bueno J, Lambros J, 2002. Investigation of crack growth in functionally graded materials using digital image correlation, Engineering Fracture Mechanics Volume 69, Issues 14-16, pp. 1695-1711.

Andersson P, Byegård J, Dershowitz B, Doe T, Hermansson J, Meier P, Tullborg E-L, Winberg A, 2002. TRUE Block Scale project. Final report – 1. Characterization and model development. SKB TR-02-13, Svensk Kärnbränslehantering AB.

Birgersson L, Gale J, Hakami E, 2000. Äspö Hard Rock Laboratory: First True Stage: Pilot Resin Experiment: Summary Report. SKB IPR-00-04, Svensk Kärnbränslehantering AB.

Chae BG, Ichikawa Y, Jeong GC, Seo YS, Kim BC, 2004. Roughness measurement of rock discontinuities using a confocal laser scanning microscope and the Fourier spectral analysis, Engineering Geology 72, Issues 3-4, pp. 181-199.

Chen S, Yue ZQ, Tham LG, 2004. Digital image-based numerical modelling method for prediction of inhomogeneous rock failure Int. J. Rock Mech. & Min. Sci., 41, pp. 939-957.

Cunningham KJ, 2004. Application of ground-penetrating radar, digital optical borehole images, and cores for characterization of porosity hydraulic conductivity and paleokarst in the Biscayne aquifer, southeastern Florida, USA, Journal of Applied Geophysics Volume 55, Issues 1-2, pp. 61-76.

Dingxiang Zou, Wang WX, Bailing Ma, 1986. Computer simulation of spatial distribution of weakness planes and its influence on rock blasting, Proc. of the Int. Sym. on intense dynamic loading and its effects, in Beijing of China, pp. 1056-1062.

Egmont-Petersen M, de Ridder D, 2002. Image processing with networks- a review, Pattern Recognition 35(2002), pp. 2279-2310.

Feng Q, 1996. Application of Image processing to borehole logging, master thesis, at Division of Engineering Geology, Department of Civil and Environmental Engineering, KTH.

Franklin JA, Maerz NH, Bennett CP, 1988. Rock mass characterization using photoanalysis, International Journal of Mining and Geological Engineering, pp. 97-112.

Fu KS, Mu JK, 1981. A survey on image segmentation, Pattern recognition, Vol. 13, pp. 3-16.

Groenewald AM, Barnard E, Botha EC, 1993. Related approaches to gradient-based thresholding, Pattern recognition Letters, Vol. l4, pp. 567-572.

Hakami E, 1995. Aperture Distribution of Rock Fractures, Doctoral thesis, at Division of Engineering Geology, Department of Civil and Environmental Engineering, KTH, TRITA-AMI PHD 1003.

Hakami E, Gale J, 1998. Äspö Hard Rock Laboratory. First TRUE Stage pilot resin experiment. Pore space analysis. SKB IPR-99-14, Svensk Kärnbränslehantering AB.

Harrison JP, 1993. Improved analysis of rock mass geometry using mathematical and photogrammetric methods. Ph.D. thesis, Imperial College, London, UK.

Hu J, Sakoda B, Pavlidis T, 1992. Interactive road finding for aerial images. IEEE Workshop on Applications of Computer Vision.

Huang K, Wu Z, Wang Q, 2005. Image enhancement based on the statistics of visual representation, Image and Vision Computing 23 (2005), pp. 51-57.

Jain AK, Duin RPW, Mao J, 2000. Statistical Pattern Recognition: A Review, IEEE Trans Pattern And Machine Intelligence, Vol. 22, No. 1, pp. 4-37.

Johansson M, 1999. Digital image processing of borehole images for determination of rock fracture orientation and aperture, Licentiate thesis, at Division of Engineering Geology, Department of Civil and Environmental Engineering, KTH, TRITA-AMI LIC 2041.

Jorge A, Lambros J, 2002. Investigation of crack growth in functionally graded materials using digital image correlation, Engineering Fracture Mechanics Volume 69, Issues 14-16, pp. 1695-1711.

Kapur JN, Sahoo PK, Wong AKC, 1985. A new method for grey-level picture thresholding using the entropy of the histogram, Computer Vision, Graphics and Image processing, 29, pp. 273-285.

Kemeny J, Post R, 2003. Estimating three-dimensional rock discontinuity orientation from digital images of fracture traces, Computers & Geosciences Volume 29, Issue 1, pp. 65-77.

Kokare M, Chatterji BN, Biswas PK, 2004. Cosine-modulated wavelet based texture features for content-based image retrieval, Pattern Recognition Letters 25 (2004), pp. 391-398.

Laubach SE, Reed RM, Olson JE, Lander RH, Bonnell LM, 2004. Coevolution of crack-seal texture and fracture porosity in sedimentary rocks: cathodoluminescence observations of regional fractures, Journal of Structural Geology Volume 26, Issue 5, pp. 967-982.

Lee K, Chung SY, 1990. A comparative performance study of several global thresholding techniques for segmentation, Computer Vision, Graphics, And Image Processing, 1990, 2, pp. 171-190.

Lemy F, Hadjigeorgiou J, 2003. Discontinuity trace map construction using photographs of rock exposures, International Journal of Rock Mechanics and Mining Sciences, Volume 40, pp. 903-917.

Lindeberg T, 1993. Detecting Salient Blob-Like Image Structures and Their Scales with a Scale-Space Primal Sketch: A Method for Focus-of-Attention, International Journal of Computer Vision, 11(3), pp. 283-318.

Liu HY, Roquete M, Kou SQ, Lindqvist P-A, 2004. Characterization of rock heterogeneity and numerical verification, Engineering Geology. Volume 72, Issues 1-2, pp. 89-119.

Lyman GJ, 2003. Rock fracture mean trace length estimation and confidence interval calculation using maximum likelihood methods, International Journal of Rock Mechanics and Mining Sciences, Volume 40, Issue 6, pp. 825-832.

Maersk Hansen L, Staub I, 2004. Äspö Hard Rock Laboratory.TRUE-1 Continuation Project. Fault Rock Zones characterisation. Overcoring (300 mm) of impregnated fault rock zones at chainages 2/430, 2/545, 2/163 and 1/600 m. SKB IPR-04-10, Svensk Kärnbränslehantering AB.

Masahiro I, 1995. Hydromechanical Characteristics of a Single Rock Joint, Doctoral thesis, in Massachusetts Institute of Technology.

Muñoz X, Freixenet Y, Cufí X, Martí J, 2003. Strategies for image segmentation combining region and boundary information, Pattern Recognition Letters 24 (2003), pp. 375-392.

Orlando L, 2003. Semiquantitative evaluation of massive rock quality using ground penetrating radar, Journal of Applied Geophysics, Volume 52, Issue 1, pp. 1-9.

Otsu N, 1979. A threshold selection method from grey-level histogram, IEEE Trans. Systems Man Cybernet, SMC-9, pp. 62-66.

Ouchterlony F, 1990. Fracture toughness testing of rock with core based specimens, Engineering Fracture Mechanics, v. 35, no. 1/2/3, pp. 351-366, printed in Great Britain.

Ozkaya SI, Mattner J, 2003. Fracture connectivity from fracture intersections in borehole image logs, Computers & Geosciences Volume 29, Issue 2, pp. 143-153.

Pal NR, Pal SK, 1993. A review of image segmentation techniques, Pattern recognition, Vol. 26, No. 9, pp. 1277-1294.

Power W, Durham W, 1997. Topography of Natural and Artificial Fractures in Granitic Rocks: Implications for Studies of Rock Friction and Fluid Migration, Int. J. Rock Mech. Min. Sci. Vol. 34, No. 6, pp. 979-989.

Reid T, Harrison J, 2000. A semi-automated methodology for discontinuity trace detection in digital images of rock mass exposures, International Journal of Rock Mechanics and Mining Sciences, Volume 37, Issue 7, pp. 1073-1089.

Reid TR, 1998. A methodology for the detection of discontinuity traces in digital images of rock mass exposures. Ph. D. thesis, Imperial College, London, UK.

Sergios P, Stavros J, 2004. On the relation between discriminant analysis and mutual information for supervised linear feature extraction, Pattern Recognition 37 (2004), pp. 857-874.

Sonka, M, Hlavac V, Boyle R, 1995. Image processing, analysis and machine vision, Champion & Hall, London

Soroushian P, Elzafraney M, Nossoni A, 2003. Specimen preparation and image processing and analysis techniques for automated quantification of concrete microcracks and voids Cement and Concrete Research, Volume 33, Issue 12, pp. 1949-1962.

Sun GX, Reddish DJ, Whittaker BN, 1992. Image analysis technique for rock fracture pattern studies around longwall excavations, Trans. Instr Min. Metall, Sect. A: Min. industry, vol. 101, A127-204, London.

Stigsson M, Hermanson J, Forsberg O, 2003. TRUE 1 Continuation. Fault rock zones. Structural models of tentative experiment sites. SKB IPR-03-49. Svensk Kärnbränslehantering AB.

Takahashi M, Takemura T, 2004. Microscopic visualization in rocks under confining pressure by means of micro focus X-ray CT, Proceedings of the ISRM International Symposium 3rd ARMS, Ohnishi & Aoki (eds), Millpress, Rotterdam, ISBN 90 5966 020 X, pp. 139-142.

Tanimoto C, Murai S, Kiyama Joshi AK, 1989. Automatic detection of lineaments from Landsat data. Proceedings of the IGARSS'89, Vancouver, Canada.

Tremblais B, Augereau B, 2004. A fast multi-scale edge detection algorithm, Pattern Regognition Letters 25 (2004), pp. 603-618.

Tsai WH, 1985. Moment-preserving thresholding: A new approach, Computer Vision, graphics, And Image Processing, 29, pp. 377-393.

Wang WX, 2003. Froth delineation based on image classification, International Journal of Mineral Engineering, Volume 16, Issue 11, pp. 1183-1192.

Wang WX, Fernlund J, 1994. Shape Analysis of Aggregates. KTH-BALLAST Report no. 2. KTH, Stockholm, Sweden.

Wang WX, Stephansson O, 1997. Computer vision for size, shape and texture of aggregates. The ninth international conference of computer methods and advances in geomechanics vol. 3, pp. 2307-2312, Wuhan, China, 2-7.

Williams JH, Johnson CD, 2004. Acoustic and optical borehole-wall imaging for fractured-rock aquifer studies, Journal of Applied Geophysics Volume 55, Issues 1-2, pp.151-159.

Winberg A, Andersson P, Byegård J, Poteri A, Cvetkovic V, Dershowitz B, Doe T, Hermanson J, Gómez-Hernández J-J, Hautojärvi A, Billaux D, Tullborg E-L, Meier P, Medina A, 2003. TRUE Block Scale project. Final report - 4. Synthesis of flow, transport and retention in the block scale. SKB TR-02-16, Svensk Kärnbränslehantering AB.

Winberg A, Andersson P, Hermanson J, Byegård J, Cvetkovic V, Birgersson L, 2000. Äspö Hard Rock Laboratory. Final report of the first stage of the tracer retention understanding experiments. SKB TR-00-07, Svensk Kärnbränslehantering AB.

Yue ZQ, Chen S, Tham LG, 2003. Finite element modeling of geomaterials using digital image processing, Computers and Geotechnics, Volume 30, Issue 5, pp. 375-397.

Zhou Y, Starkey J, Mansinha L, 2004. Segmentation of petrographic images by integrating edge detection and region growing, Computer & Geosciences 30 (2004), pp. 817-831.